Eur. J. Mineral., 36, 943–983, 2024
https://doi.org/10.5194/ejm-36-943-2024

European Journal of Mineralogy
Open Access

Pressure–temperature–time and REE mineral evolution in low- to medium-grade polymetamorphic units (Austroalpine Unit, Eastern Alps)

Marianne Sophie Hollinetz[1], Benjamin Huet[2], David A. Schneider[3], Christopher R. M. McFarlane[4], Ralf Schuster[5], Gerd Rantitsch[6], Philip Schantl[7,8], Christoph Iglseder[2], Martin Reiser[2], and Bernhard Grasemann[1]

[1]Department of Geology, University of Vienna, Josef-Holaubek-Platz 2, 1090 Vienna, Austria
[2]Division of Basic Geological Services, GeoSphere Austria, Hohe Warte 38, 1190 Vienna, Austria
[3]Department of Earth and Environmental Sciences, University of Ottawa, 150 Louis-Pasteur Private, Ottawa, K1N 6N5, Canada
[4]Department of Earth Sciences, University of New Brunswick, 3 Bailey Drive, Fredericton, E3B 5A3, Canada
[5]Division of Geophysical and Applied Geological Services, GeoSphere Austria, Hohe Warte 38, 1030 Vienna, Austria
[6]Department Applied Geosciences and Geophysics, University of Leoben, Peter-Tunner-Straße 5, 8700 Leoben, Austria
[7]Institute of Earth Sciences, University of Graz, Universitätsplatz 2, 8010 Graz, Austria
[8]Department of Petrology and Geochemistry, NAWI Graz Geocenter, University of Graz, Universitätsplatz 2, 8010 Graz, Austria

Correspondence: Marianne Sophie Hollinetz (marianne.sophie.hollinetz@univie.ac.at)

Received: 13 March 2024 – Revised: 15 August 2024 – Accepted: 8 September 2024 – Published: 27 November 2024

Abstract. We investigated rare earth element (REE) minerals in low- to medium-grade metapelites sampled in two nappes of the Austroalpine Unit (Eastern Alps, Austria). Combining microstructural and chemical characterization of the main and REE minerals with thermodynamic forward modeling, Raman spectroscopy on carbonaceous material (RSCM) thermometry and in situ U–Th–Pb dating reveal a polymetamorphic evolution of all samples. In the hanging wall nappe, allanite and REE epidote formed during Permian metamorphism (275–261 Ma, 475–520 °C, 0.3–0.4 GPa). In one sample, Cretaceous (ca. 109 Ma) REE epidote formed at ∼ 440 °C and 0.4–0.8 GPa at the expense of Permian monazite clusters. In the footwall nappe, large, chemically zoned monazite porphyroblasts record both Permian (283–256 Ma, 560 °C, 0.4 GPa) and Cretaceous (ca. 87 Ma, 550 °C, 1.0–1.1 GPa) metamorphism. Polymetamorphism produced a wide range of complex REE-mineral-phase relationships and microstructures. Despite the complexity, we found that bulk rock Ca, Al and Na contents are the main factor controlling REE mineral stability; variations thereof explain differences in the REE mineral assemblages of samples with identical pressure and temperature (P–T) paths. Therefore, REE minerals are also excellent geochronometers to resolve the metamorphic evolution of low- to medium-grade rocks in complex tectonic settings. The recognition that the main metamorphic signature in the hanging wall is Permian implies a marked P–T difference of ∼ 250 °C and at least 0.5 GPa, requiring a major normal fault between the two nappes which accommodated the exhumation of the footwall in the Cretaceous. Due to striking similarities in setting and timing, we put this low-angle detachment in context with other Late Cretaceous low-angle detachments from the Austroalpine domain. Together, they form an extensive crustal structure that we tentatively term the "Austroalpine Detachment System".

1 Introduction

The Austroalpine Unit in the European Eastern Alps is a nappe stack that was assembled during a Cretaceous intracontinental collision within the Adriatic microplate (i.e., Eo-Alpine event; Froitzheim et al., 2008, and references therein; Schmid et al., 2004). Resolving Eo-Alpine regional metamorphic patterns and structures is fundamental in identifying contacts between different nappes and illuminating the tectonic evolution of the Alpine orogeny (e.g., Rantitsch et al., 2020). Acquiring Eo-Alpine pressure–temperature–time–deformation (P–T–t–D) data is particularly challenging in the basement nappes due to pre-Alpine metamorphic signatures related to Variscan tectonics (von Raumer and Neubauer, 1993) and Permian lithosphere-scale extension (Permian event; Schuster et al., 2001; Schuster and Stüwe, 2008). In particular, lower and mid-crustal rocks of the Permian crust cooled at depth and were only exhumed later during Eo-Alpine tectonics, resulting in a close spatial correlation between Permian and Eo-Alpine metamorphism, however with markedly different P–T gradients (see Knoll et al., 2023, for a compilation of Permian and Schuster et al., 2004, for Eo-Alpine P–T conditions). Complexities related to polymetamorphism are reasonably well constrained for medium- and high-grade metamorphic units owing to index mineral and diagnostic mineral assemblages (e.g., polyphase garnet, stability of alumosilicates; Bestel et al., 2009; Gaidies et al., 2006; Habler et al., 2006, 2009; Schulz and Krause, 2021; Schuster et al., 2001; Tropper and Recheis, 2003). In low-grade metamorphic units which lack such minerals, the timing of metamorphism and deformation is poorly understood. The current geochronological dataset in these units largely relies on K–Ar, Ar–Ar and Rb–Sr analyses (e.g., Dallmeyer et al., 1998; Gasser et al., 2010, and references therein; Neubauer et al., 2007; Schantl et al., 2015), which can be ambiguous in terms of their geological significance.

To compensate for the lack of data, U–Th–Pb dating of rare earth element (REE)-bearing minerals (e.g., allanite, monazite, xenotime, apatite) provides a promising alternative approach (e.g., Stumpf et al., 2024). Reactions involving REE minerals have been described both in the context of prograde metamorphism (e.g., Boston et al., 2017; Janots et al., 2006, 2008; Wing et al., 2003), during retrograde overprint (e.g., Bollinger and Janots, 2006; Gasser et al., 2012; Skrzypek et al., 2017) and in cases where a secondary REE mineral assemblage developed at the expense of inherited (igneous or metamorphic) REE phases (e.g., Cenki-Tok et al., 2011; Finger et al., 1998; Hentschel et al., 2020; Krenn and Finger, 2007). Additionally, REE minerals may recrystallize through dissolution–precipitation, potentially controlled by deformation and fluid-related alteration (e.g., Budzyn et al., 2011; Catlos et al., 2002; Ricchi et al., 2019; Wawrzenitz et al., 2012; Williams et al., 2011). In situ dating of REE minerals thus offers the potential to date a variety of geological processes and to resolve complex polyphase evolution histories (e.g., Gaidies et al., 2008a; Janots et al., 2009), provided that the petrogenetic significance of the target is well understood. In this contribution, we apply a multimethod approach that combines rigorous petrographical and chemical rock characterization with in situ U–Th–Pb geochronology and thermodynamic forward modeling on metapelites sampled in two Austroalpine polymetamorphic basement nappes across a major tectonic contact.

2 Geological setting

The study area is located at the eastern margin of the upper Austroalpine Unit (UAU; Fig. 1a). The UAU consists of a polymetamorphic basement, Paleozoic metasediments and a Permo-Mesozoic cover that was partly metamorphosed. We focus on two nappe systems that consist dominantly of Paleozoic metasediments and basement rocks. The structurally higher Drauzug–Gurktal Nappe System (DG-NS) contains large portions of Paleozoic metasediments. In the DG-NS, Eo-Alpine metamorphic conditions are generally low and decrease from greenschist facies at the base to diagenetic conditions at the top (Schuster et al., 2004). The structurally lower Koralpe–Wölz Nappe System (KW-NS) represents the Eo-Alpine high-pressure extrusion wedge with eclogite bodies in the center and a metamorphic field gradient that decreases to lower amphibolite facies towards higher and lower structural levels (Schuster et al., 2004). We here use the tectonic and lithostratigraphic nomenclature defined by Matura and Schuster (2014; Fig. 1b).

In the western part of our study area, three low-grade metamorphic nappes of the DG-NS (formerly "Graz Paleozoic") are exposed. The Gasen, Schöckel and Gschnaidt nappes are differentiated based on lithology and metamorphic conditions (Schantl et al., 2015). These nappes consist of metapelites with intercalated metavolcanics and thick packages of marbles with protolith ages ranging from Silurian to upper Carboniferous (Flügel and Hubmann, 2000; Gasser et al., 2010). Close to the contact with the underlying KW-NS, peak metamorphic temperatures of 450–500 °C are constrained by mineral assemblages, mineral thermometers and Raman spectroscopy on carbonaceous material (RSCM) data (Bojar et al., 2001; Rantitsch et al., 2005; Schantl et al., 2015). Somewhat higher temperatures (500–530 °C) were calculated in garnet-bearing metapelites at the base of the Gschnaidt Nappe (Schantl et al., 2015). Only sparse quantitative pressure estimates around 0.4–0.6 GPa exist in the Schöckel Nappe (Bojar et al., 2001). These metamorphic conditions have been linked to Early Cretaceous thrusting inferred by white mica and biotite K–Ar and Rb–Sr geochronological data (Fritz, 1988, 1991; Schantl et al., 2015) or advective heating during the Late Cretaceous to Paleogene exhumation of the KW-NS (Rantitsch et al., 2005). K–Ar and Rb–Sr white mica ages dispersed between 240 and 140 Ma

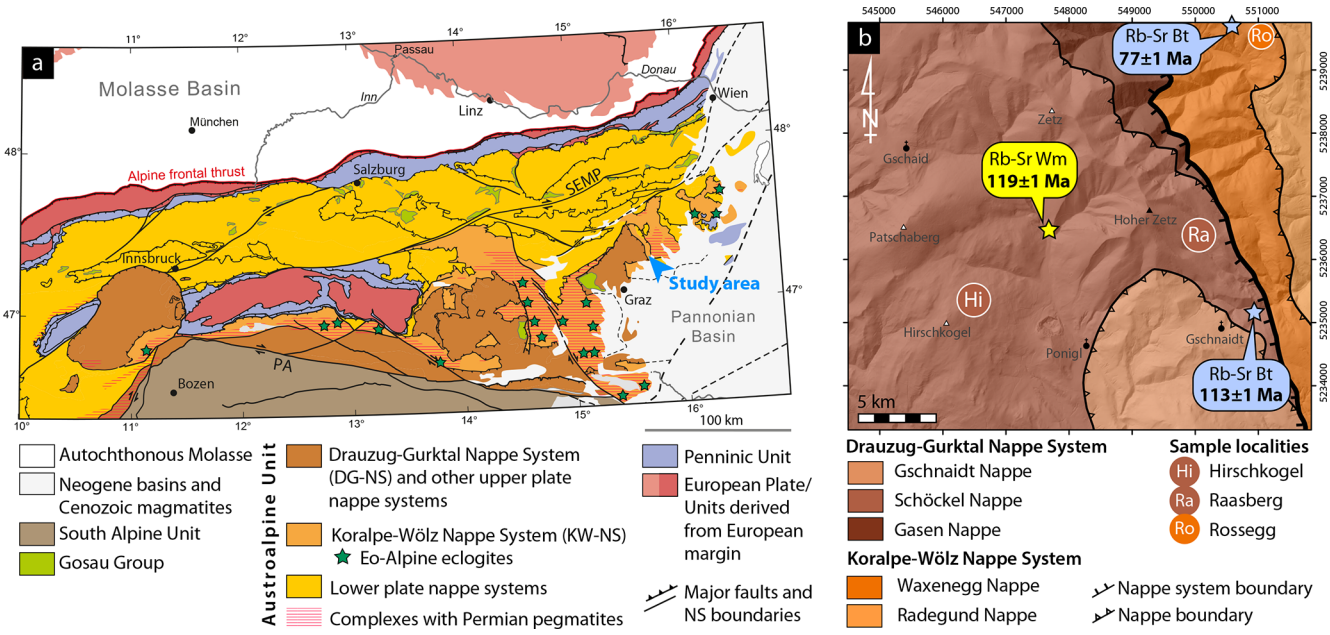

Figure 1. **(a)** Simplified tectonic map of the Eastern Alps and the Austroalpine Unit (modified based on Schuster and Stüwe, 2022). Upper and lower plates are relative to the Cretaceous Eo-Alpine suture zone based on Stüwe and Schuster (2010). The blue arrow shows the position of the detailed map. **(b)** Tectonic map of the study area (UTM 33N coordinate grid) showing sample locations. Rb–Sr geochronological data are from Schantl et al. (2015).

(Gasser et al., 2010, and references therein) and polyphase garnet at the base of the Gschnaidt Nappe (Schantl et al., 2015) indicate a pre-Alpine metamorphic event of unknown age.

The Waxenegg Nappe, a structurally high nappe of the KW-NS, is exposed in the eastern part of the area (formerly "Anger Crystalline Unit"; Krenn et al., 2008). It contains garnet-bearing metapelites with intercalated quartzites, amphibolites and marbles forming the Rossegg Complex. Geothermobarometry of garnet-bearing metapelites in the Waxenegg Nappe suggests 580 °C and 0.8 GPa during Eo-Alpine metamorphism (Krenn et al., 2008). Schantl et al. (2015) also describe relic garnet cores of presumably Permian age; however, no geochronological or P–T data exist for the pre-Alpine metamorphic event. Although the age of Eo-Alpine peak metamorphism in the Waxenegg Nappe is not known, cooling below 300 °C at ca. 80 Ma is resolved by Rb–Sr biotite geochronology (Schantl et al., 2015). According to Krenn et al. (2008), the contact between the DG nappes and the KW-NS is characterized by top-to-northeast thrusting during the Middle to Late Cretaceous (> 95 Ma), which became subsequently overprinted by top-to-southwest brittle and ductile normal faults after being related to an extension in the Later Cretaceous (< 95 Ma).

3 Methods

For this study, we targeted lithologies that contain high-variance mineral assemblages suitable for P–T modeling (e.g., with chloritoid, garnet and/or staurolite) and U–Th–Pb geochronology (with allanite and REE epidote, monazite, xenotime) in the Hirschkogel Lithodeme (top of the Schöckel Nappe), Raasberg Formation (base of the Schöckel Nappe) and the Rossegg Complex (Waxenegg Nappe; Fig. 1b). The lithostratigraphic names are used to refer to the sample localities. The initial objective of this study was to obtain precise P–T and age data for the Eo-Alpine event, which was considered the main metamorphic event based on previous studies (Krenn et al., 2008; Rantitsch et al., 2005; Schantl et al., 2015). However, results of U–Th–Pb geochronology revealed that all sample groups experienced polymetamorphism. Therefore, results for each sample group (Sects. 4 to 6) are arranged as follows: the petrography, mineral chemistry and microstructures of main and REE phases are described, followed by the presentation and first-order interpretation of the geochronological data. Then, equilibrium assemblages for each metamorphic event are identified based on the microstructural relationship between the dated REE phase, main phases and fabric elements. Finally, P–T conditions are derived using thermodynamic forward modeling and, where available, peak temperatures from RSCM. Table 1 contains an overview of interpreted mineral assemblages, P–T and age data.

https://doi.org/10.5194/ejm-36-943-2024

Table 1. Sample overview, interpreted mineral assemblages and results of RSCM thermometry and U–Th–Pb geochronology.

Sample	Alias[a]	UTM 33N easting	UTM 33N northing	Lithostrati-graphic unit	Nappe (nappe system)	Lithology	Permian		Eo-Alpine		Local/ retrograde phases	Tmax RSCM (°C)	Pseudo-section	U–Th–Pb geochro-nology (Ma)
							Main phases (+Ms+Qz)	REE phases (*prograde)	Main phases (+Ms+Qz)	REE phases				
Hi-1	MSH1822B	546332	5235580	Hirschkogel	Schöckel	Cld-bearing phyllite	Cld+Chl+Rt	Aln+Xtm +Ap	Cld+Chl+Rt	Aln	Mnz/Rhb +Thr+Kao		Fig. 3c	Aln: 261.3 ± 8.4
Hi-2	MSH1825A	546420	5235383	Lithodeme	Nappe	Cld-bearing phyllite	Cld+Chl+Rt	Aln+Ap	Cld+Chl+Rt	Mnz/Rhb +Thr			Fig. S13	
Hi-3	MSH1828A	546469	5235752		(DG-NS)	Cld-bearing phyllite	Cld+Chl +Ilm	Aln+Ap	Cld+Chl+Rt	Mnz/Rhb +Thr			Fig. S13	
Hi-4	KP02[b]	546565	5235647			Cld-bearing phyllite	Cld+Chl+Rt	Aln+Ap	Cld+Chl+Rt				Fig. S13	
Hi-5	KP06[b]	546702	5235353			Cld-bearing phyllite	Cld+Chl+Rt	Aln+Ap	Cld+Chl+Rt				Fig. S13	
Hi-6	KP07[b]	546344	5235182			Cld-bearing phyllite	Cld+Chl +Ilm	Aln+Ap	Cld+Chl+Rt				Fig. 3d	
Hi-7	MSH1822D	546332	5235580			Graphitic phyllite						495 ± 29		
Hi-8	MSH1824C	546143	5235540			Graphitic phyllite						483 ± 42		
Ra-1	MSH1830A	550119	5236376	Raasberg	Schöckel	Cld-bearing micaschist, type I	St+ Cld_1+Bt_1+Pl+Ilm	Aln_1+Ep_1	Cld_2+Ilm+Rt		Chl, Kao			
Ra-2	08R09b	550096	5236566	Formation	Nappe	Cld-bearing micaschist, type I	St+Cld_1+Bt_1+Pl+Ilm	Aln_1+Ep_1	Cld_2+Ilm+Rt		Chl, Kao			
Ra-3	MSH1830E	550119	5236376		(DG-NS)	Cld-bearing micaschist, type I	St+Cld_1+Bt_1+Pl+Ilm	Aln_1+Ep_1	Cld_2+Bt_2+Ilm+Rt		Chl, Kao		Fig. 8e, g	Aln_1/Ep_1: 275.2 ± 6.4
Ra-4	MSH1830B	550119	5236376			Cld-bearing micaschist, type II	St+Pl_{ab}+Pl_{ol}+Ilm	Aln_1*+Ep_1*	Cld+Pg +Ilm+Rt +Mnz+Xtm	Ep_2+Ap ± Mnz_2	Thr		Fig. 8f	Ep_2: 108.8 ± 6.6
Ro-1	MSH1832A	551047	5239580	Rossegg	Waxenegg	Grt-micaschist, graphitic	St+Bt +Pl+Ilm	Mnz_1	Grt+Cld+Chl +Pg+Ilm	Mnz_2	Complex	Nappe	Fig. 11e, f	
Ro-2	MSH1833B	551028	5239531		(KW-NS)	Grt-micaschist, graphitic	St+Bt +Pl+Ilm	Mnz_1	Grt+Cld+Chl +Pg+Ilm	Mnz_2	Bt	558 ± 29		Mnz_1: 283–256[c] Mnz_2: 87.3 ± 1.2[d]
Ro-3	MSH1833C	551028	5239531			Grt-micaschist, graphitic						563 ± 29		

[a] Sample name in database of GeoSphere Austria. [b] Sample from Schantl et al. (2015). [c] Crystallization over a prolonged period (see Sect. 7.1.2). [d] Minimum crystallization age (see Sect. 7.4.2).

Table 2. Whole-rock analyses of major and trace elements.

Sample	Hi-1	Hi-2	Hi-3	Hi-4[a]	Hi-5[a]	Hi-6[a]	Ra-1	Ra-2	Ra-3	Ra-4	Ro-1	Ro-2
Whole-rock analysis [w %]												
SiO_2	44.76	47.25	52.19	54.25	49.30	53.36	41.19	41.96	49.52	37.99	56.13	53.07
TiO_2	2.231	1.382	1.464	1.22	1.63	1.30	4.54	4.473	3.57	5.56	1.269	1.243
Al_2O_3	30.52	27.01	25.24	23.90	26.54	24.36	29.66	29.03	22.27	31.56	23.96	24.77
Fe_2O_3	6.62	10.58	9.44	9.87	11.24	10.50	15.95	12.2	12.36	14.41	8.22	7.66
MnO	0.022	0.06	0.039	0.21	0.08	0.06	0.067	0.062	0.073	0.076	0.088	0.08
MgO	1.72	1.84	1.3	2.14	2.33	1.12	0.65	0.64	1.46	0.52	1.13	1.15
CaO	0.29	0.3	0.23	0.12	0.13	0.00	0.29	0.96	1.42	0.62	0.17	0.22
Na_2O	1.06	0.75	0.75	0.67	1.01	0.65	0.58	0.68	0.52	2.23	1.77	1.63
K_2O	6.53	5.6	5.3	4.09	4.47	5.05	4.05	4.83	4.44	2.76	3.72	4.52
P_2O_5	0.18	0.23	0.18	0.17	0.19	0.16	0.16	0.59	1.03	0.23	0.18	0.23
LOI	5.11	4.98	4.47	4.99	4.97	4.86	3.55	3.56	3.19	3.5	3.39	3.85
Total	99.04	99.99	100.60	101.64	101.87	101.41	100.70	98.98	99.86	99.46	100.00	98.42
Al/Al^{b}_{Shaw}	1.836	1.625	1.519	1.438	1.597	1.466	1.785	1.747	1.340	1.899	1.442	1.490
Ca/Ca^{b}_{Shaw}	0.133	0.138	0.106	0.055	0.060	0.000	0.133	0.440	0.651	0.284	0.078	0.101
Na/Na^{b}_{Shaw}	0.613	0.434	0.434	0.387	0.584	0.376	0.335	0.393	0.301	1.289	1.023	0.942
XMg	0.34	0.26	0.21	0.30	0.29	0.17	0.07	0.09	0.19	0.07	0.21	0.23
Trace element analysis [ppm]												
Sc	30	29	28	23	24	23	26	26	20	27	23	24
V	257	217	195	164	195	171	253	275	184	172	178	196
Cr	180	140	130	112	126	116	30	30	40	< 20	130	140
Co	9	15	12	nd	nd	nd	17	16	23	15	15	11
Ni	50	40	50	54	47	54	30	< 20	40	30	40	30
Cu	< 10	20	10	42	41	60	< 10	< 10	< 10	< 10	30	20
Zn	80	180	130	146	152	256	160	140	130	250	110	110
Ga	40	36	32	33	34	32	39	39	31	41	33	34
Rb	302	241	230	191	208	232	43	46	54	28	124	144
Sr	265	191	125	158	188	132	201	212	121	462	315	325
Y	45	39	37	43	51	41	32	69	36	72	39	40
Zr	394	158	222	175	248	193	461	492	267	459	266	218
Nb	39	24	25	25	35	25	86	78	54	86	25	24
Cs	12.7	9.5	8.8	nd	nd	nd	0.7	0.6	1.5	0.5	3.6	3.6
Ba	1165	1086	848	585	541	808	145	203	204	113	1078	1101
La	128	40.8	29.7	nd	nd	nd	47.9	55.2	41.1	56.2	70.8	67.5
Ce	274	92.6	64	106	155	69	88.3	114	80.3	112	140	132
Pr	31.1	10.2	7.04	nd	nd	nd	12	14.2	10.3	14.3	16.1	14.9
Nd	118	38	26.2	51	70	66	48.5	57.9	44.5	60.5	60.6	56.6
Sm	20.5	7.6	5.3	nd	nd	nd	10.4	13.3	9.6	13.6	10.7	10.8
Eu	3.94	2.02	1.35	nd	nd	nd	3.79	4.65	3.72	5.27	2.21	2.35
Gd	13.4	6.7	5	nd	nd	nd	8.8	12.1	9.6	13.3	8.5	9
Tb	2	1.2	0.9	nd	nd	nd	1.3	1.9	1.4	2.1	1.4	1.5
Dy	10.7	7.4	6.1	nd	nd	nd	6.9	12.2	7.6	12.7	7.9	8.5
Ho	1.8	1.5	1.3	nd	nd	nd	1.3	2.5	1.4	2.5	1.6	1.7
Er	4.6	4.4	3.8	nd	nd	nd	3.9	7	3.6	6.6	4.7	4.8
Tm	0.61	0.64	0.58	nd	nd	nd	0.55	0.96	0.48	0.87	0.67	0.69
Yb	3.8	3.9	3.7	nd	nd	nd	3.7	5.3	3	5.1	4.6	4.6
Lu	0.57	0.59	0.57	nd	nd	nd	0.54	0.83	0.46	0.75	0.65	0.68
Hf	10.6	4.3	6.1	nd	nd	nd	10.7	11.4	6.2	10.7	7.6	6.2
Ta	3.1	1.8	1.8	nd	nd	nd	6.3	5.2	4.1	6.1	2	1.9
W	3	1	1	nd	nd	nd	16	1	13	12	20	22
Pb	27	30	27	24	32	26	< 5	< 5	< 5	8	23	20
Th	28.1	19.7	18.6	25	24	21	7.4	7.3	4.3	6.9	23.3	23.1
U	5.2	3	2.9	< 20	< 20	< 20	1	1.3	0.9	1.4	3	2.7

nd: not determined. [a] Schantl et al. (2015). [b] Normed by the average low-grade metamorphic pelite of Shaw (1956).

3.1 Petrography and mineral and whole-rock chemistry

Systematic microstructural and petrographic sample characterization involved optical and scanning electron microscopy (SEM) in backscattered electron mode (BSE) combined with energy-dispersive X-ray spectroscopy (EDS). Planar fabrics are referred to as S and numbered chronologically. Sn is used for the main planar fabric if no sedimentary layering (S0) is preserved. Note that numbering only applies to individual sample groups. Selected samples were processed for further chemical analyses. Whole-rock major and trace elements were analyzed by inductively coupled plasma mass spectrometry (ICP-MS) and are reported in Table 2. The mineral chemistry of the main and REE phases was investigated using an electron probe microanalyzer (EPMA). Details on analytical protocols, the full EPMA dataset, and additional chemical plots and compositional maps are provided in the Supplement (Sect. S1, Tables S1–S11, Figs. S1–S6). Mineral abbreviations are based on Whitney and Evans (2010). Sodium- and potassium-rich white micas are referred to as paragonite and muscovite, respectively, although the latter may compositionally correspond to phengite. When muscovite and paragonite are not distinguishable, white mica (Wm) is used. XMg is defined as $Mg/(Fe^{2+}+Mg)$. We discriminate several types of epidote-group minerals based on microstructural context and composition. For epidote types that entirely fall in the allanite subgroup (REE+Th+U > 0.5 atoms per formula unit, apfu), we use the term allanite. For simplicity, we use REE epidote (abbreviated Ep) for types that show a heterogeneous composition corresponding partly to the allanite and to the clinozoisite groups (Armbruster et al., 2006) within single grains. REEs are grouped as follows: light REEs (LREEs) La–Nd, medium REEs (MREEs) Sm–Gd and heavy REEs (HREEs) Tb–Lu+Y.

3.2 Geochronology

Allanite, REE epidote and monazite of selected samples were analyzed using laser-ablation inductively coupled plasma mass spectrometry (LA-ICP-MS). Crater diameters are 24 µm for allanite and REE epidote and 10 µm for monazite. During analyses of U, Th and Pb isotopes, additional elements (e.g., Ca, Nd, La, Y, Ti, Zr) were monitored to assess the influence of potential inclusions and correlate the U–Th–Pb dates to chemical domains in the analyzed mineral. Tera–Wasserburg concordia diagrams computed with IsoplotR (Vermeesch, 2018) revealed a significant common Pb (Pb_0) contribution in all datasets. Allanite and REE epidote U–Th–Pb data are thus reported as joint isochron regression ages (Vermeesh, 2020). Radiogenic Pb of monazite varies between 91 %–98 % (Pb*; Table S12); thus a correction based on measured net ^{204}Pb was employed, and corrected dates are reported on concordia diagrams and weighted mean $^{206}Pb/^{238}U$ ages computed with IsoplotR. Details on the analytical protocol, data reduction, Tera–Wasserburg diagrams and the full LA-ICP-MS dataset are provided in the Supplement (Sect. S2, Figs. S7–S10, Table S12).

3.3 Thermodynamic modeling, effective bulk rock composition and RSCM analysis

Pseudosections were calculated using the Theriak/Domino software package (De Capitani and Petrakakis, 2010). We used the database file td-tcds62-6axmn-03.txt (http://dtinkham.net/peq.html, last access: 25 November 2024) compiled by Douglas Tinkham (Laurentian University, Canada) which combines the tc-ds62 thermodynamic dataset (Holland and Powell, 2011) and mineral activity–composition relations in the MnNCKFMASHTO system (White et al., 2014). Modifications accounting for pyrophyllite substitution in white mica (Coggon and Holland, 2002) and related to Mn-bearing endmembers of ilmenite, chloritoid and chlorite (see Hollinetz et al., 2022) are also applied. The feldspar model of Fuhrman and Lindsley (1988) was used.

Molar proportions of the effective bulk rock composition (Table S13) are derived from whole-rock analyses (Table 2) or calculated from average mineral compositions measured by EPMA and mineral proportions estimated from petrography, where small-scale compositional layering indicates limited equilibration (sample Hi-1; Table S14). The following choices regarding the compositional space were made for the calculations. Manganese is an important compositional parameter to consider when modeling garnet- and ilmenite-bearing assemblages. Test calculations showed that excluding Mn significantly shifts the position of ilmenite, rutile and garnet reactions towards higher temperatures (Fig. S11). Calculations including Mn predicted realistic compositions for ilmenite, chloritoid and garnet; therefore it is included in the models of all samples. Ferric iron may also influence the stability of Fe–Mg silicates and Fe–Ti oxides, particularly at low-grade metamorphic conditions (e.g., Lo Pò and Braga, 2014). The lack of Fe^{3+}-bearing oxides (e.g., magnetite, hematite) and very minor amounts of Fe^{3+} calculated in the structural formulae of chloritoid, staurolite, garnet and ilmenite generally suggest reducing conditions at the metamorphic peak, consistent with the common occurrence of carbonaceous material. We therefore conclude that the uncertainties related to introducing ferric iron in the model compositional space outweigh potential benefits in terms of model accuracy.

Determining the effective Ca concentration is challenging since identified Ca-bearing phases (allanite, apatite) are not reproduced by the model if REEs and P are not considered. Using the uncorrected Ca content derived from whole-rock analysis therefore predicts phases that are not observed in the natural sample (e.g., margarite or plagioclase in sample Hi-1; Fig. S11). For the Raasberg and Rossegg samples, the measured CaO content was corrected to account for CaO corresponding to apatite following Hollinetz et al. (2022) (Ta-

Table 3. Results of RSCM thermometry and Raman spectra parameters with 1σ standard deviation (SD) following Lünsdorf et al. (2017) of four graphitic samples.

Sample	No. of spectra	D_STA	SD	G_STA	SD	G shape factor	SD	D_{max}	SD	G_{max}	SD	D_{max}/G_{max}	SD	Temp [°C]	±
Hi-7	20	117.6	11.0	41.9	5.9	5.1	0.8	1351.3	2.7	1580.2	2.2	0.4	0.1	495	29
Hi-8	19	119.34	35.65	45.85	10.22	5.19	2.08	1346.28	4.37	1578.23	3.67	0.39	0.14	483	42
Ro-2	20	164.6	70.2	28.9	4.1	7.4	2.6	1353.7	5.0	1579.1	2.9	0.2	0.1	558	29
Ro-3	20	216.4	78.9	28.0	5.1	8.1	2.8	1355.8	4.4	1579.4	1.4	0.1	0.1	563	29

ble S13). This approach yields negative Ca values for some Hirschkogel samples. The presence of resorbed allanite and apatite remnants infers open-system behavior of Ca postdating the metamorphic peak. Given the uncertainties related to the effective bulk Ca concentration at the metamorphic peak, we decided to exclude Ca entirely from the compositional space for the Hirschkogel samples. We noted negligible influence on the stability fields of rutile and ilmenite that are used for the determination of P–T conditions (Fig. S11), thus justifying this approach. In the Raasberg samples, we acknowledge discrepancies between the model stability field of clinozoisite (Cz) and neighboring Ca-bearing phases compared to the real stability field of allanite and REE-bearing epidote. Considering overall uncertainties related to both the thermodynamic database and the effective bulk rock composition, we generally assume a minimum error of ±30 °C and ±0.1 GPa for all thermodynamic calculations (Plunder et al., 2012; Powell and Holland, 2008).

Four graphitic samples (Hi-7, Hi-8, Ro-2, Ro-3) were selected for RSCM analyses which were carried out at the University of Leoben (Austria), following the procedure outlined in Hollinetz et al. (2022). Measured Raman parameters and maximum temperatures calculated based on Lünsdorf et al. (2017) are reported in Table 3.

4 Hirschkogel samples

4.1 Petrography and microstructures

Chloritoid-bearing phyllites of the Hirschkogel Lithodeme (samples Hi-1 to Hi-6) are macroscopically highly heterogeneous, which is reflected by color variations in the fine-grained matrix and size of chloritoid porphyroblasts in different layers. Darker, graphitic variants contain small (< 300 µm) chloritoid porphyroblasts. In mica-rich silvery phyllites, chloritoid is larger (up to 2 mm). This heterogeneity is also reflected at the millimeter-scale by compositional variations in the matrix (phyllosilicate-rich vs. quartz-rich) and the occurrence of accessory minerals (Fig. 2a–b). All samples show an Al-rich bulk rock composition and are strongly depleted in Ca relative to Shaw's (1956) average pelite ($Ca/Ca_{Shaw} < 0.14$; Table 2). Bulk rock XMg values range from 0.17 to 0.34.

Several generations of planar fabrics are distinguishable. In some samples, primary sedimentary layering (S0) can be recognized based on changes in matrix composition as well as accessory mineral grain size and morphology (Fig. 2a). We therefore assume the heterogeneity is partly inherited from the protolith. A relic schistosity (S1) is preserved as internal foliation of porphyroblasts or in domains of very fine-grained interlayering of white mica and chlorite (Fig. 2a). The main schistosity (S2) is defined by the orientation of white mica; chlorite; and, if present, ilmenite. Relic S1 fold hinges suggest it formed as an axial surface cleavage during folding of S1 (Fig. 2c). The folding of S2 locally leads to the formation of a crenulation cleavage (S3; Fig. 2b, e). The phyllosilicate-rich matrix is dominated by muscovite and chlorite, which are either fine-grained and oriented parallel to S2 or coarse-grained oblique to S2 and adjacent to large porphyroblasts (Fig. 2c–e). The XMg of white mica correlates with the sample bulk rock chemistry (Fig. 3b, Table 2). Variability in Si (3.04–3.12 apfu) is noted but is not systematically linked to microstructural domains. Along the S3 crenulation cleavage, chlorite is typically absent; muscovite is reoriented but no newly grown muscovite is present (Fig. 2e). Euhedral chloritoid porphyroblasts (up to 2 mm) are oriented parallel or oblique to the S2 schistosity (Fig. 2c). As for muscovite, their chemical composition is related to the bulk rock chemistry of the sample. In some samples, a slight increase in XMg from core to rim is noted (Fig. 3a).

The sample set exhibits contrasting Fe–Ti oxide assemblages and morphologies. Sample Hi-1 contains rutile that forms euhedral, elongate (up to 20 µm) or very fine-grained (< 1 µm) crystals that are ubiquitous in the matrix and as inclusions in porphyroblasts (Fig. 2c). In samples Hi-2, Hi-4 and Hi-5, rutile forms fine-grained intergrowths with muscovite, chlorite and quartz. Remnants of Mn-rich ilmenite (XMn = 0.04; Fig. 3a) are found partially replaced by rutile intergrowths included in chloritoid, suggesting these intergrowths are pseudomorphs of ilmenite (Fig. 2d). In samples Hi-3 and Hi-6, Mn-poor ilmenite is the dominant Ti-oxide mineral (XMn = 0.02; Fig. 3a). It forms euhedral, lath-shaped crystals oriented parallel to the main schistosity S2 (Fig. 2e, h). Occasionally, tiny quartz or muscovite inclusions are present. Ilmenite exhibits variable degrees of replacement by rutile, particularly in the S3 crenulation cleavage domains (Fig. 2e).

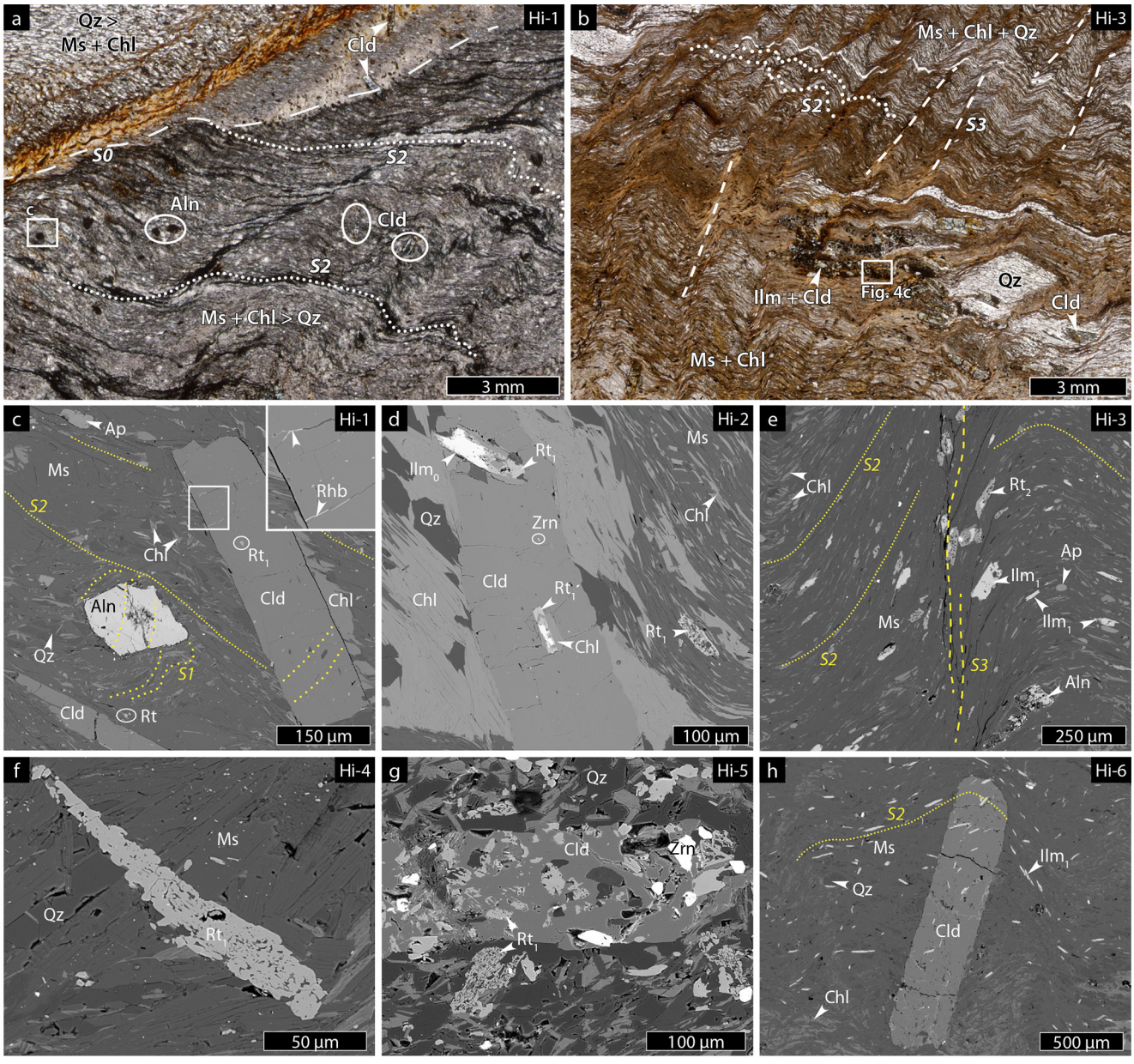

Figure 2. Transmitted light photomicrographs and representative BSE–SEM images illustrating microstructural features and phase assemblages of Hirschkogel samples (sample name given in the upper right corner). **(a)** Sedimentary layering (S0) preserved in sample Hi-1, overprinted by S2 (relic S1 not visible at this scale). **(b)** Crenulation cleavage (S3) forms as a result of folding of S2. S0 is largely overprinted by later planar fabrics. **(c)** Chloritoid and allanite porphyroblasts showing an internal foliation (S1) in a matrix of muscovite, chlorite, rutile and quartz. The inset shows a bright LREE-rich phase tentatively labeled rhabdophane (Rhb) that precipitated in cracks of chloritoid. **(d)** Ilmenite partially replaced by a rutile aggregate is overgrown by chloritoid. Note that ilmenite is fully replaced in the matrix. **(e)** Matrix ilmenite pseudomorphed by rutile and resorbed allanite along the S3 crenulation cleavage of sample Hi-3. **(f)** Sample Hi-4 contains rutile pseudomorphs after ilmenite in the matrix. **(g)** Layer containing abundant rutile pseudomorphs and zircon overgrown by chloritoid. **(h)** Sample Hi-6 contains euhedral ilmenite both in the matrix and included in chloritoid.

4.2 REE bulk rock pattern and REE mineralogy

Whole-rock REE patterns normalized to the average upper-crust composition (Rudnick and Gao, 2003) exhibit similar HREE patterns for all samples but appear heterogeneous in terms of L+MREE contents (Fig. S12). Sample Hi-1 shows the highest REE concentration and is enriched in L+MREE. In samples Hi-2 and Hi-3, L+MREEs are depleted with respect to HREEs and possess a positive Eu anomaly. The REE minerals are, in order of relative abundance, allanite, apatite,

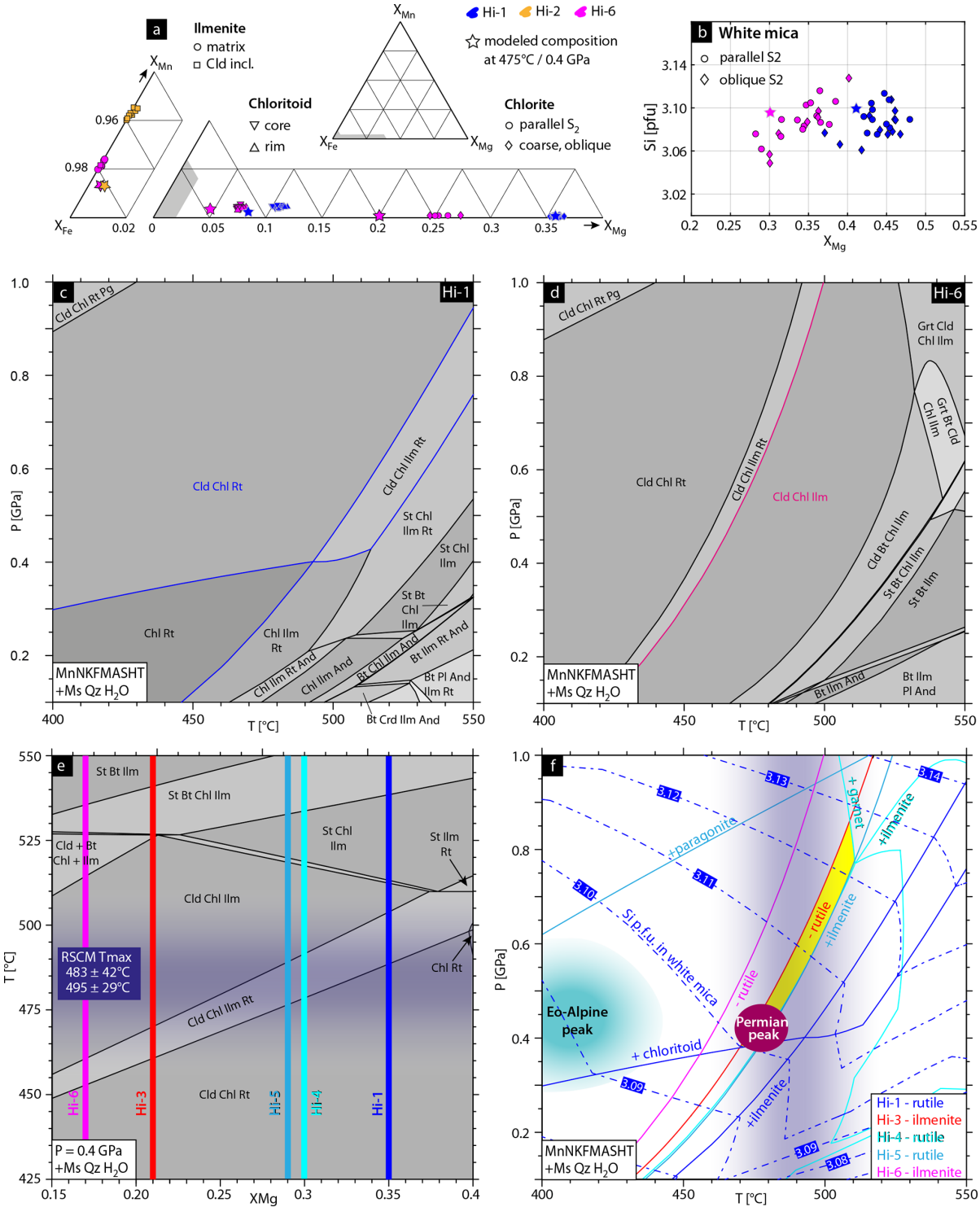

Figure 3. Mineral chemistry of **(a)** chloritoid, chlorite and ilmenite and **(b)** white mica measured with EPMA for selected Hirschkogel samples with the lowest (Hi-6) and highest (Hi-1) bulk rock XMg. The ilmenite composition of sample Hi-2 is also shown. See Fig. S1 for other samples. Large stars represent modeled mineral compositions at given P–T conditions. **(c–d)** Representative P–T pseudosections for selected Hirschkogel samples with the peak assemblage highlighted. **(e)** XMg–T pseudosection calculated at 0.4 GPa. Average values of SiO_2, TiO_2, Al_2O_3, MnO, K_2O, Na_2O and (FeO+MgO) from all Hirschkogel samples were used (Table S13). Colored bars indicate the bulk XMg of different samples. **(f)** Composite P–T pseudosection of five Hirschkogel samples with contrasting peak metamorphic assemblages (only important reactions are shown; see Fig. S13 for full pseudosections) and isolines for Si (pfu) in muscovite for sample Hi-1 (dash-dotted blue lines). The yellow area indicates overlapping peak assemblage fields for all samples. RSCM temperatures at 483 and 495 °C of two samples are shown as the dark blue shaded area (Table 3).

zircon, xenotime, thorite, monazite and rhabdophane group minerals.

Allanite is most abundant in phyllosilicate-rich layers where it forms large (100–500 µm) isolated porphyroblasts or polycrystalline aggregates (Figs. 2c, 4a–b). Generally, elongate allanite crystals are oriented parallel to S2 and may be fractured (Fig. 3b). Inclusions are mostly matrix minerals and, less abundantly, apatite; xenotime; and rare, tiny monazite crystals along cracks (Fig. 4a, b). An internal foliation (S1) is delineated by inclusions of fine-grained (< 5 µm) muscovite, chlorite, quartz and rutile (Fig. 4a). Most allanite blasts possess a distinct porosity in the core, causing a fibrous appearance of the allanite (Fig. 3a, d). Mineral chemistry is available for allanite in sample Hi-1 (Table S9) but is expected to be similar in other Hirschkogel samples because of the similar BSE Z contrast (Fig. 4a, b). Allanite is relatively homogeneous and characterized by a high REE+U+Th content (0.64–0.75 apfu; Fig. 4g) with L+MREEs enriched relative to HREEs (< 0.05 apfu; Fig. 4h). From core to rim, a slight, gradual decrease in La and increase in Nd are noted (Fig. 4e). The Th content is highest in the interior (0.5 wt % ThO_2) and also decreases towards the rim (Fig. 4f). Some zones that are devoid of small inclusions deviate from this general pattern. These zones, denoted as "alteration", show patchy zoning with minor REE enrichment in bright zones and depletion in darker zones in high-contrast BSE images (Fig. 4d, g). Allanite in sample Hi-1 is relatively pristine, although the limited resorption and formation of kaolinite with small thorite crystals are noted (Fig. 4a), potentially associated with metamitization and alteration of the Th-rich, porous core. Allanite resorption is more advanced in other samples, particularly in microstructural positions close to the S3 crenulation (Fig. 3c, e). Resorbed allanite blasts are characterized by a pronounced porosity and irregular cracks filled with quartz and fine-grained phyllosilicates. Around such remnants, a corona of tiny (< 3 µm), irregular thorite crystals and fine-grained phyllosilicates often develop (Fig. 4b). These grains correspond to the thorite–xenotime solid solution with M+HREE enrichment relative to LREE, a weak negative Eu anomaly and Y_2O_3 concentrations between 3.9 wt % and 6.8 wt % (Fig. 4i).

Apatite is ubiquitous in all samples and ranges from 10 to 50 µm in diameter. Based on morphology, we distinguish (1) anhedral, porous apatite grains; (2) euhedral, unzoned apatite without pores; and (3) composite apatite grains that consist of a porous core that may be enriched in REEs, Th and U and a darker rim similar to euhedral apatite. Anhedral apatite is typically found in layers enriched in zircon (Fig. 4c), whereas euhedral and composite apatite is dispersed in the matrix and often oriented parallel to S2 (Fig. 4b). Zircon is present as round or subhedral grains of variable size (5–30 µm), typically showing cracks and porous zones. These features and its enrichment in layers with other heavy minerals strongly suggest a detrital origin (Fig. 4c). Xenotime is rare and forms outgrowths on detrital zircon grains (inset Fig. 4c) or small (< 10 µm), anhedral grains that are dispersed in the matrix (Fig. 4a). EPMA measurements of a few xenotime grains reveal a heterogeneous chemical composition characterized by variations in M+HREEs (Fig. 4i). Monazite is uncommon and forms small (< 7 µm) euhedral or subhedral grains. In rare cases it forms isolated grains in the matrix, but more commonly it occurs spatially associated with allanite, either adjacent to or enclosed along cracks in allanite (Fig. 4a, b). EPMA analysis of a few monazites in sample Hi-1 show a homogeneous composition in terms of LREEs and a weak negative Eu anomaly (Fig. 4i). The monazite thermometer of Gratz and Heinrich (1997) yields temperatures between 343 and 482 °C (Table S10, inclusions not considered). The ThO_2 concentration is low (< 0.4 wt %) and slightly elevated in matrix-hosted monazite (0.8 wt %–1.8 wt %). A bright, LREE-rich phase that precipitated in thin (< 1 µm) cracks of chloritoid porphyroblasts or along grain boundaries in the phyllosilicate-rich matrix was observed systematically in all Hirschkogel samples (Fig. 2a). EDS analysis yields spectra that are similar to monazite but with a pronounced Ca peak. The bright phase thus likely corresponds to a rhabdophane group mineral, which commonly forms during low-grade metamorphism (e.g., Krenn and Finger, 2007; Nagy et al., 2002).

4.3 Geochronology

U–Th–Pb dating of well-preserved allanite in sample Hi-1 yields a Pb/U–Th isochron date of 261.3 ± 8.4 Ma (*n*: 41; MSWD: 1.4; Fig. 5a). This date is within error of the Tera–Wasserburg lower intercept date of 250.7 ± 9.9 Ma (Fig. S7). Upon comparing LA-ICP-MS and EPMA chemical data, we found that most analyses correspond to the compositional domain of the dark allanite mantle (Fig. 5d). The dark mantle of allanite contains the highest U concentration, whereas the interior exhibits larger Th / U ratios and higher Pb_0 concentrations. Minor amounts of Zr (up to 152 ppm) and elevated Ti (up to 18 350 ppm) suggest the contribution of tiny zircon and rutile inclusions in some of the analyses (Table S12). Excluding these analyses, however, has no effect on the U–Th–Pb date (Fig. S7).

Allanite contains fine-grained inclusions of the same phases present in the matrix and possess an internal foliation, clearly indicating its metamorphic origin. The absence of fine-grained inclusions and minor compositional modifications in a few "alteration zones" in allanite (Fig. 4d) indicate limited recrystallization postdating allanite growth. No related effect is seen in the allanite U–Th–Pb data, suggesting the minor importance of this process. The 261.3 ± 8.4 Ma Pb/U–Th isochron date is thus interpreted as the crystallization age of the dark allanite mantle.

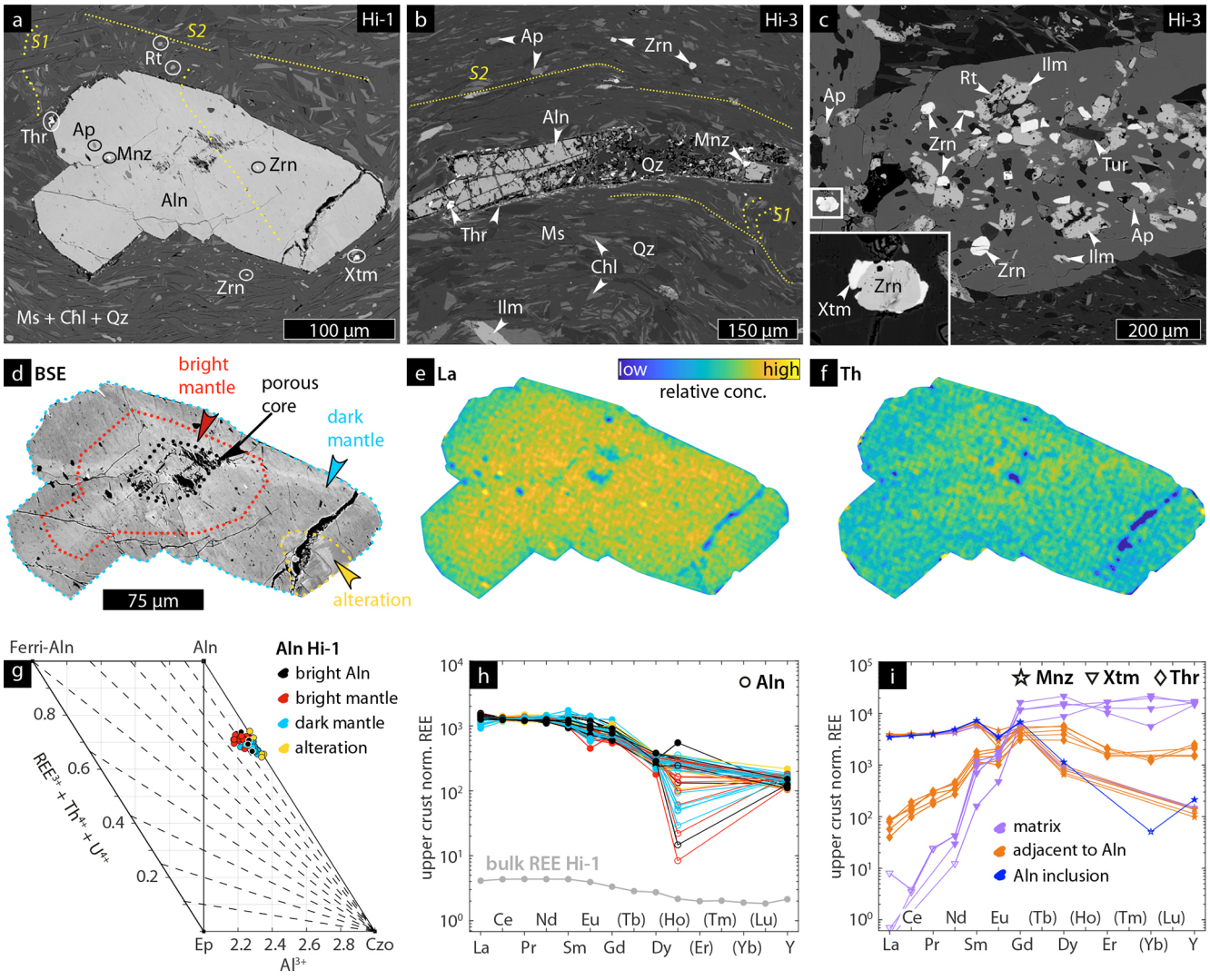

Figure 4. REE phase relationships and chemistry in Hirschkogel samples. **(a)** BSE–SEM image of euhedral allanite in sample Hi-1 with tiny inclusions delineating an internal foliation (S1). Note tiny thorite crystals along the rim. **(b)** BSE–SEM image of strongly resorbed allanite in sample Hi-3 surrounded by tiny thorite crystals and a few anhedral monazite crystals. **(c)** BSE–SEM image of detrital minerals (zircon, apatite, ilmenite and tourmaline) enriched in a layer enclosed in chloritoid. Inset shows xenotime forming around porous, fractured zircon. **(d)** High-contrast BSE–SEM of allanite shown in **(a)** with different zones highlighted and element maps showing the **(e)** La and **(f)** Th distribution. **(g)** Al (pfu) vs. REE+U+Th (pfu) plots illustrating compositional variation in allanite in the clinozoisite (Cz)–epidote (Ep)–ferriallanite (Ferri-Aln)–allanite (Aln) system. Dashed lines represent lines of constant Fe oxidation state. **(h–i)** REE distribution normalized by the average upper crust of Rudnick and Gao (2003) of **(h)** allanite and **(i)** monazite, xenotime and thorite. Low totals of thorite (82 wt %–96 wt %; Table S10) indicate a contribution of matrix minerals. Elements in brackets were not analyzed in all datasets.

4.4 Interpretation of Permian and Eo-Alpine parageneses and fabrics

Based on petrographic observations only, all observed parageneses could theoretically be explained by a monometamorphic history. In fact, prior to U–Pb dating of allanite, we assumed that the Hirschkogel samples experienced a single metamorphic cycle during the Eo-Alpine event based on a muscovite Rb–Sr date of 119.2 ± 1.2 Ma in the same nappe (Schantl et al., 2015) and attributed signs of resorption to minor retrogression during exhumation. Our finding that allanite crystallized in the Permian suggests an alternative, more complex evolution: the main metamorphic imprint occurred in the Permian, followed by a lower-grade Eo-Alpine overprint.

Allanite and chloritoid occur both as euhedral porphyroblasts and share similar inclusion patterns (Fig. 3a). Straight phase boundaries between the chloritoid; allanite; and the matrix-hosted chlorite, muscovite and quartz indicate that these minerals were in equilibrium during Permian meta-

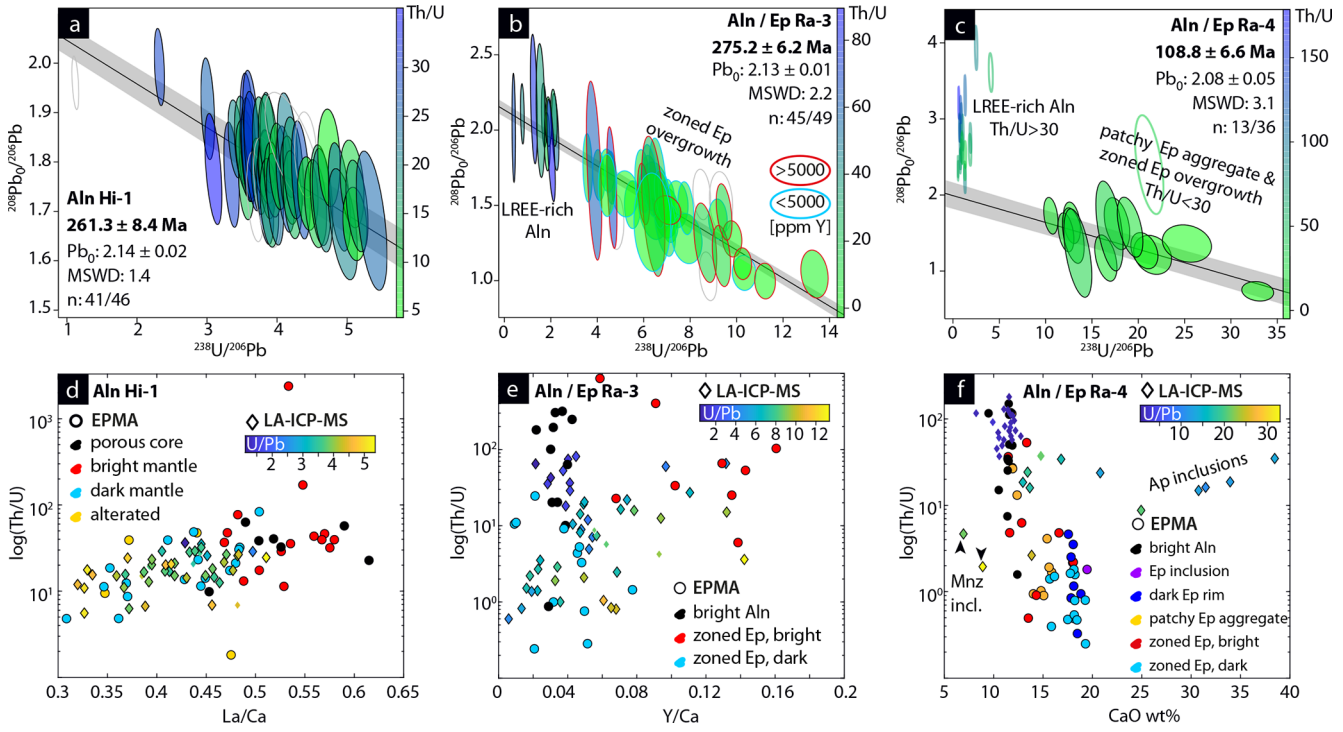

Figure 5. Geochronological data of allanite and REE epidote in samples Hi-1, Ra-3 and Ra-4. **(a, b, c)** Total Pb/U–Th isochrons shown in $^{208}Pb_0/^{206}Pb - {}^{238}U/^{206}Pb$ space (Vermeesch, 2020) of allanite and REE epidote in samples Hi-1, Ra-3 and Ra-4. **(d)** La/Ca vs. log(Th / U) plot, **(e)** Y/Ca vs. log(Th / U) and **(f)** CaO (wt %) vs. log(Th / U) comparing LA-ICP-MS data (diamond symbols) color-coded by $^{238}U/^{206}Pb$ and EPMA data (circles). Analyses that are excluded from the age calculation are shown as open ellipses in the isochron plots and as small diamonds in the compositional plots.

morphism. The interpretation of ilmenite–rutile phase relations and contrasting morphologies is more complex and requires consideration of (1) the variation in the temperature-dependent transition of rutile to ilmenite with changing bulk rock XMg, (2) the polymetamorphic evolution and (3) the detrital source of Ti. RSCM thermometry of two graphite-bearing samples yields peak temperatures at 483 and 495 °C (Table 3) that fall in the range of the temperature-dependent transition of rutile to ilmenite in metapelites (White et al., 2014). A XMg–T pseudosection calculated at intermediate pressure (0.4 GPa) predicts the observed assemblage of chloritoid + chlorite + muscovite + quartz at $T < 520$ °C across the whole range of XMg ratios reflected by our sample set (Fig. 3e). Depending on the XMg ratio, either ilmenite (XMg < 0.25) or rutile (XMg > 0.3) is predicted as the stable Ti-bearing phase for the peak temperature suggested by RSCM. Accordingly, we interpret the dispersed, fine-grained rutile of high-XMg sample Hi-1 as a Permian peak metamorphic phase.

Samples Hi-2, H-4 and Hi-5 show intermediate XMg values and contain rutile as the dominant Ti-bearing phase. It is present as aggregates, which are interpreted as pseudomorphs after ilmenite. These pseudomorphs are enriched in layers with other heavy minerals (e.g., zircon; Fig. 2g) which are interpreted as a sedimentary microscale paleoplacer, thus suggesting a detrital origin of ilmenite. This is also supported by the Mn-rich composition of incompletely replaced ilmenite remnants preserved as a chloritoid inclusion in sample Hi-2, which suggests an igneous rather than a metamorphic origin (Fig. 4a). We therefore interpret rutile in these samples as the peak Permian phase (Rt_1) which formed at the expense of detrital ilmenite.

In the low-XMg samples Hi-3 and Hi-6, we noted the same replacement structure of ilmenite by fine-grained rutile. However, its extent is minor and mostly limited to microstructural domains along the S3 cleavage (Fig. 2e). Elsewhere, ilmenite is the dominant Ti-bearing phase and occurs both enriched in paleoplacer layers (Fig. 3c) but also dispersed in the matrix (Fig. 2h). It contains muscovite inclusions and chemically matches the composition predicted by thermodynamic modeling (Fig. 4a). For these samples, multiple replacement reactions of ilmenite and rutile and vice versa are possible: during prograde Permian metamorphism, detrital ilmenite is (partially) replaced by fine-grained rutile aggregates (Rt_1). This stage is captured where paleoplacer layers are overgrown by chloritoid (Fig. 2g). At Permian peak conditions, Rt_1 was replaced by metamorphic ilmenite (Ilm_1), supported by the presence of muscovite inclusions and its composition, which closely matches the predicted composition by the model (Fig. 3a). Minor replacement by

rutile (Rt_2) observed in these samples is attributed to the Eo-Alpine metamorphic overprint.

To summarize, the Permian peak assemblage (not considering REE-bearing minerals) consists of chloritoid, chlorite, muscovite, quartz and rutile in samples Hi-1, Hi-2, Hi-4 and Hi-5 and ilmenite in samples Hi-3 and Hi-6. The pervasive foliation defined by the matrix minerals (S2) is also interpreted as Permian fabric. The S3 crenulation cleavage observed in all Hirschkogel samples is interpreted as Eo-Alpine. In low-XMg samples (Hi-3, Hi-6), retrogressed Permian ilmenite occurs particularly along the S3 crenulation cleavage. Since only minor replacement of chloritoid by coarse-grained chlorite is noted, we assume that their mode changed during the Eo-Alpine overprint, but both minerals remained stable. The Eo-Alpine assemblage therefore consists of chloritoid, chlorite, quartz, muscovite and rutile in all samples.

4.5 Permian and Eo-Alpine *P–T* conditions

Pseudosection calculations for individual samples reproduced the Permian peak assemblage in a large stability field bordered by the chloritoid-out, paragonite-in and ilmenite-in reaction for the high-XMg, rutile-bearing samples (Fig. 3d). For the low-XMg, ilmenite-bearing samples, the field is delimited by the rutile-out, staurolite-in and garnet-in reactions (Fig. 3e). However, combining several samples with contrasting peak assemblages allows constraining *P–T* conditions much more precisely. Figure 3f illustrates important reactions of three rutile-bearing and two ilmenite-bearing samples (not including the incompletely equilibrated sample Hi-2 with detrital ilmenite remnants; see Fig. S13 for pseudosections of samples Hi-3 to Hi-5). The yellow area at 470–500 °C and 0.4–0.8 GPa marks the overlap of peak assemblages of all samples. The chloritoid-forming reaction of sample Hi-1 and the garnet-in reaction of sample Hi-4 mark the lower and upper pressure limits, respectively. *P–T* conditions are in agreement with RSCM maximum temperatures and the average Si contents in white mica (3.07–3.10 apfu), which imply relatively low-pressure conditions. Permian peak conditions therefore reached 475 °C and 0.4 GPa.

Minimum *P–T* conditions of the Eo-Alpine overprint are given by the chloritoid stability field ($T > 350$ °C, $P >$ 0.3 GPa; Fig. 4f). The upper temperature limit is defined by the rutile stability field (Fig. 4f). The absence of paragonite indicates that Eo-Alpine metamorphism occurred below 0.5–0.6 GPa (Fig. 4f). Muscovite was reoriented during S3 deformation, but no neoblastic muscovite developed and its composition measured in S3 domains does not significantly deviate from matrix muscovite. Considering all the characteristics together, we conclude that the Eo-Alpine overprint occurred at similar pressure compared to the Permian peak conditions (0.3–0.6 GPa) but at temperatures ∼ 50–100 °C less than the Permian maximum temperature (475 °C).

5 Raasberg samples

5.1 Petrography and microstructures

Four mica schist samples (Ra-1 to Ra-4) are characterized by an unusual large amount and size of chloritoid porphyroblasts (30 vol %–40 vol % of the rock). All samples are enriched in Al and depleted in Ca relative to Shaw's (1956) average pelite. Na contents are low, except for sample Ra-4 ($Na/Na_{Shaw} = 1.29$; Table 2). The bulk rock XMg is generally low (0.07–0.09) and slightly higher in sample Ra-3 (0.19). The main foliation (Sn) is heterogeneously developed in the sample set, indicating variable degrees of finite strain. In the least-deformed sample Ra-4, the weakly developed Sn is defined by the preferred orientation of fine-grained ilmenite and is overgrown by coarser-grained, mostly randomly oriented minerals (Fig. 7a). Samples Ra-1 and Ra-2 show a distinct Sn characterized by ilmenite-rich layers that bend around large, oblique-growing chloritoid porphyroblasts (Fig. 6a). Sample Ra-3 is strongly foliated with Sn defined by the preferred orientation of fine-grained white mica and biotite in the matrix. Around porphyroblasts, the development of strain shadows is noted (Fig. 6b, g, h). Muscovite is the dominant matrix mineral in all samples. It is typically coarse-grained and grows oblique to Sn, except in sample Ra-3, which also contains fine-grained muscovite oriented parallel to Sn. Silicon in muscovite varies between 3.04 and 3.11 apfu regardless of its orientation with respect to the foliation (Fig. 8d). In sample Ra-4, fine-grained white mica aggregates of predominantly paragonitic composition are commonly associated with resorbed staurolite blasts (Fig. 7b).

All samples contain both staurolite and chloritoid porphyroblasts that exhibit variable phase relationships. In samples Ra-1 to Ra-3, staurolite is rare and two types of chloritoid are distinguished based on microstructural characteristics and its relationship to staurolite. In the less-deformed samples Ra-1 and Ra-2, staurolite is subhedral, small (< 1 mm) and typically engulfed by larger (∼ 5 mm) chloritoid porphyroblasts (Cld_1). XMg of staurolite ranges from 0.08 to 0.16 and is controlled by the sample bulk composition. Different chemical populations within the same sample indicate limited equilibration of staurolite inclusions at the thin-section scale (Fig. 8a). Moreover, significant contents of TiO_2 and ZnO (up to 0.58 wt % and 1.91 wt %, respectively; Table S7) were measured in staurolite. In a few cases, we observed euhedral staurolite that lacks signs of resorption and shares straight phase boundaries with Cld_1. Both phases share a similar inclusion spectrum defined by round quartz, apatite and ilmenite, which is aligned parallel to Sn. Ilmenite layers that are bent around obliquely oriented Cld_1 porphyroblasts suggest syn- or intertectonic Cld_1 growth with respect to Sn (Fig. 6a). In samples Ra-1 and Ra-2, the XMg of Cld_1 increases from core to rim (0.06–0.12; Fig. 8a). Sample Ra-3 contains elongated aggregates of fine-grained chloritoid and quartz that reach up to 2 cm in length and are aligned par-

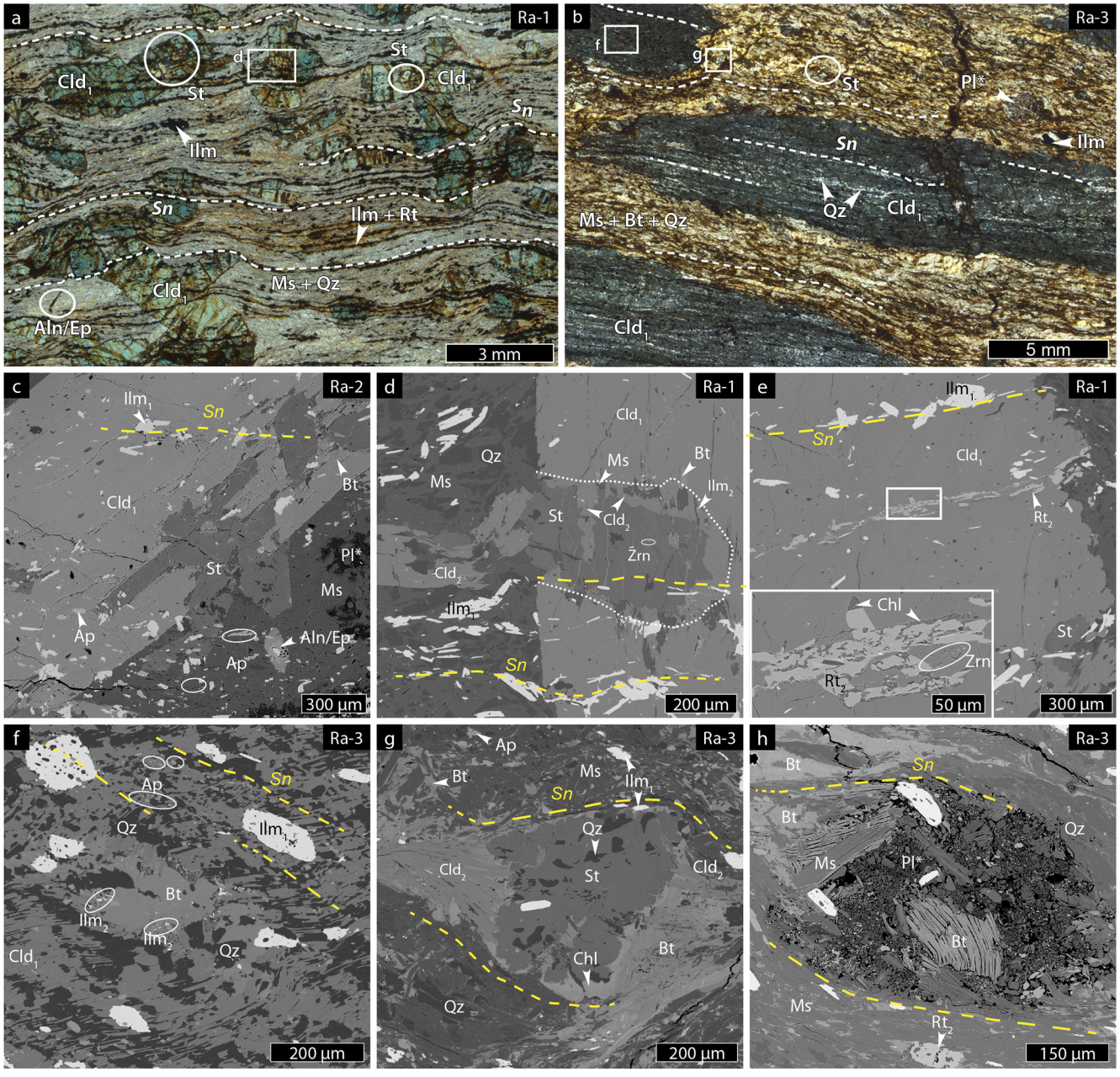

Figure 6. Transmitted light photomicrographs **(a–b)** and BSE–SEM images **(c–h)** illustrating microstructural features and phase assemblages of samples Ra-1, Ra-2 and Ra-3 (sample name given in the upper right corner). **(a)** Chloritoid porphyroblasts overgrowing a fabric (Sn) defined by ilmenite layers in sample Ra-1. **(b)** Very large chloritoid porphyroblasts in sample Ra-3 with numerous quartz inclusions. **(c)** Large chloritoid porphyroblast (Cld_1) intergrown with staurolite. Straight phase boundaries indicate intergrowth in equilibrium. **(d)** Large Cld_1 with small staurolite inclusions that are partially replaced by Cld_2 and muscovite. **(e)** Ilmenite inclusions in Cld_1 pseudomorphed by an aggregate of rutile and chlorite. **(f)** Coarse-grained biotite included in exceptionally large Cld_1. Note the tiny ilmenite needles (Ilm_2) adjacent to the biotite inclusion and the internal foliation (Sn) delineated by quartz inclusions. **(g)** Small, needle-shaped chloritoid (Cld_2) and biotite in strain shadows of preserved matrix staurolite in sample Ra-3. **(h)** Pseudomorphs of fine-grained clay minerals which are interpreted as pseudomorphs of plagioclase (Pl*) associated with coarse-grained biotite. Note that the foliation (Sn) wraps around the pseudomorph.

allel to Sn (Fig. 6b). These aggregates are interpreted as exceptionally large, deformed Cld_1 blasts that contain numerous rounded quartz inclusions delineating an internal foliation and representing a significant modal proportion in the blasts (Fig. 6f). Chemically, these large blasts are homogeneous with XMg at 0.12–0.14 (Fig. 8a). The second type of

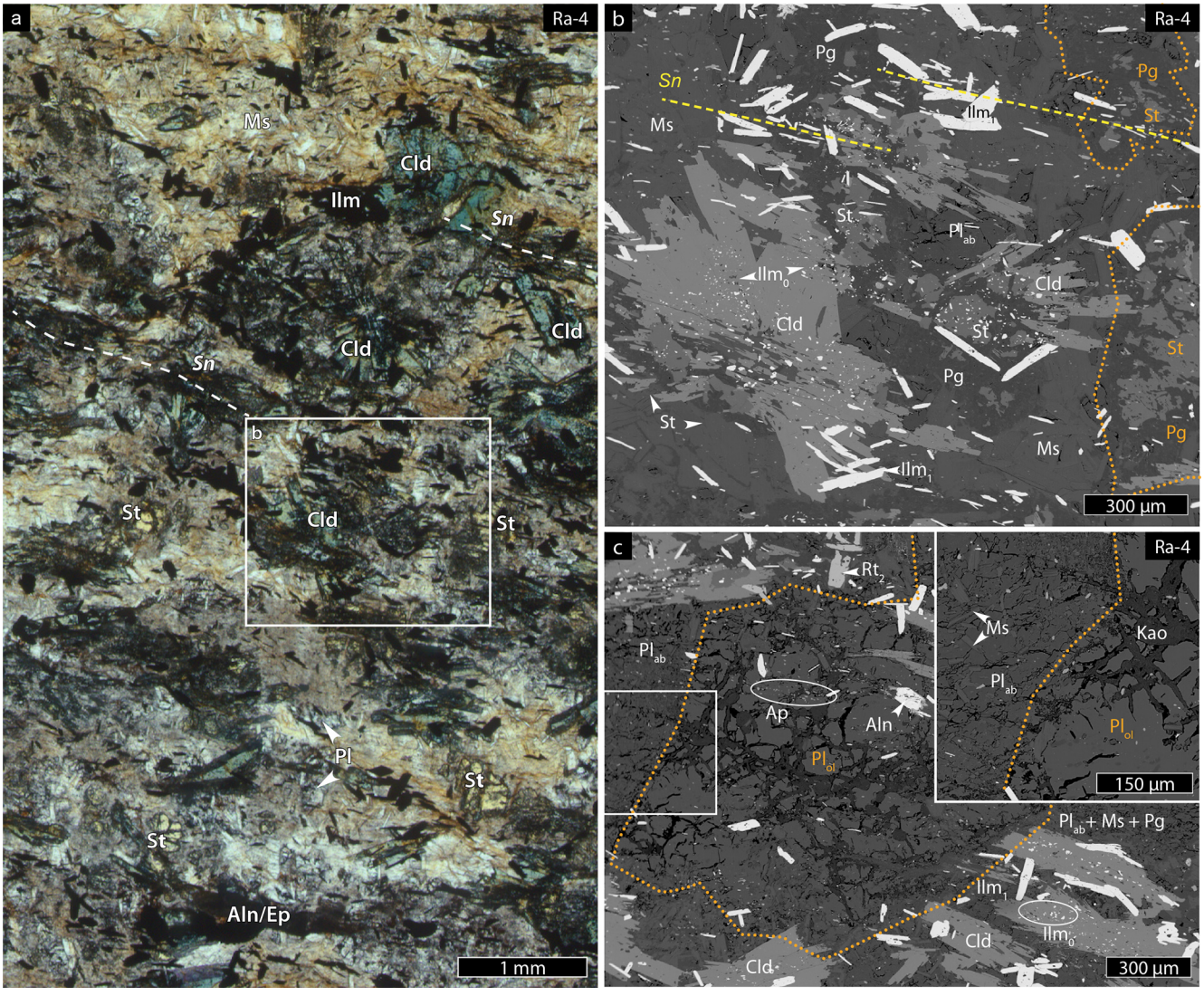

Figure 7. Transmitted light photomicrograph **(a)** and BSE–SEM images **(b–c)** illustrating microstructural features and phase assemblages of Raasberg sample Ra-4. **(a)** Poorly foliated sample Ra-4 with staurolite remnants replaced by fine-grained white mica and chloritoid aggregates. Note the small grain size of chloritoid in comparison to type I samples. **(b)** Staurolite remnants replaced by chloritoid and paragonite. Dashed orange lines delineate the original shape of staurolite. **(c)** Domain of sample Ra-4 dominated by coarse-grained albitic plagioclase (Pl_{ab}) and oligoclase (Pl_{ol}). Although both types of plagioclase are partially resorbed by muscovite and kaolinite, note that the inferred phase boundaries are relatively straight (highlighted by dashed orange lines). Inset shows resorption of Pl_{ab} by muscovite and kaolinite randomly growing in cracks of Pl_{ol}.

chloritoid (Cld_2) is significantly smaller and forms at the expense of staurolite. In sample Ra-3, Cld_2 displays a needle-shaped habitus, forms in strain shadows around resorbed matrix staurolite (Fig. 6g) and exhibits slightly lower XMg contents compared to Cld_1 (Fig. 8a). In samples Ra-1 and Ra-2, the distinction between Cld_1 and Cld_2 is not straightforward where staurolite is engulfed in large Cld_1 blasts. Note, however, the presence of muscovite, which roughly delineates the shape of the original staurolite blasts (Fig. 6d). Chemically, Cld_2 is comparable to the rim of Cld_1 (Fig. 8a).

In sample Ra-4, staurolite is most abundant, and only one type of chloritoid is observed. Staurolite forms up to 2 mm long, is typically strongly resorbed porphyroblasts and is overgrown by rosette-shaped aggregates of small (< 1 mm) chloritoid crystals and fine-grained, randomly oriented, predominantly paragonitic white mica (Fig. 7a, b). The replacement of staurolite by white mica is pseudomorphic and the inclusion pattern of staurolite blasts characterized by numerous minute (< 20 µm), round, ilmenite crystals (Ilm_0; Fig. 8b–c) is preserved. Chemically, both chloritoid and stau-

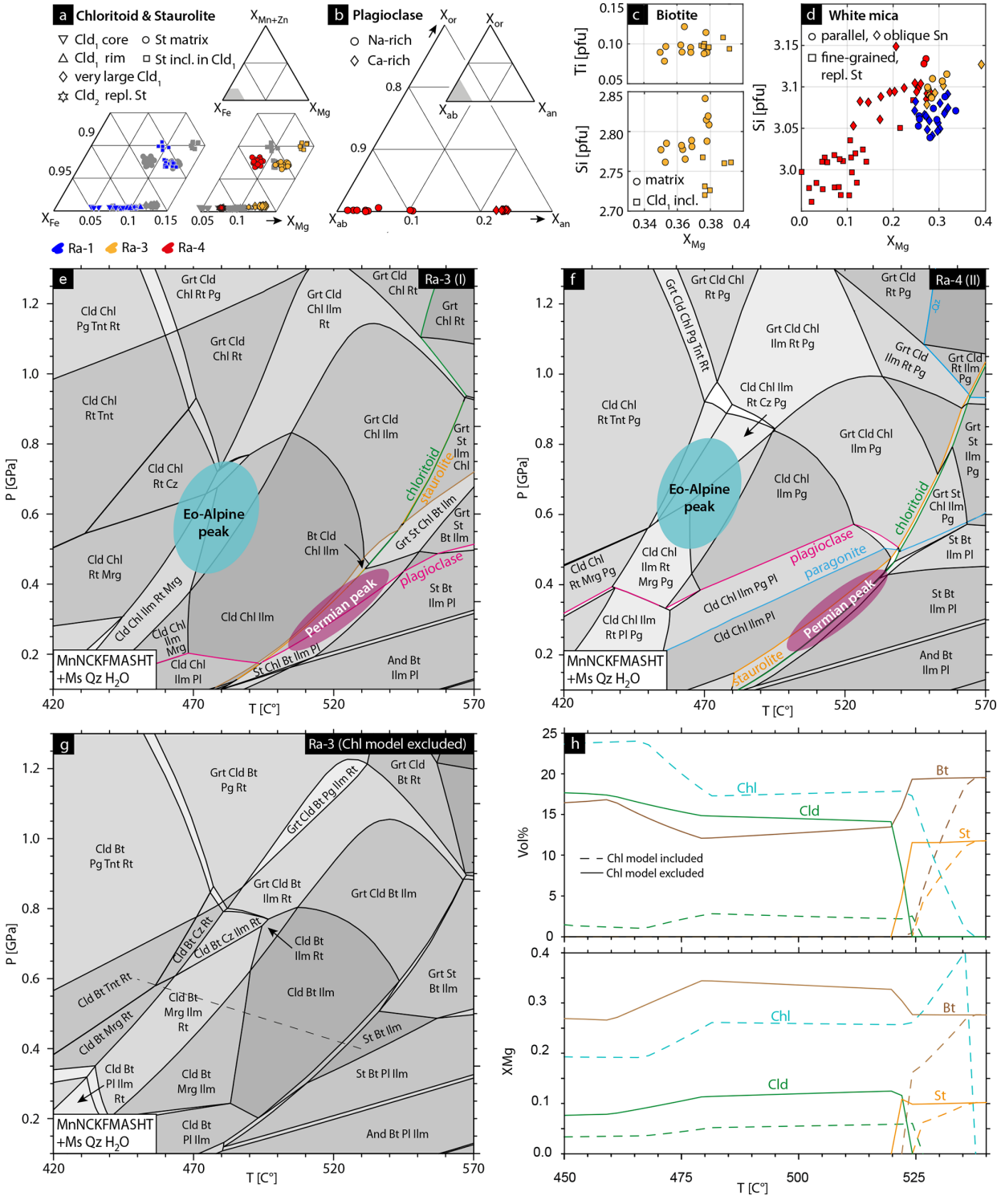

Figure 8. Mineral chemistry measured with EPMA for selected Raasberg samples. Additional data for sample Ra-2 are in Fig. S5. The same color code applies for plots **(a)**–**(d)**. **(a)** XFe – XMg – XMn ternary plot showing chloritoid and staurolite chemistry. Data for sample Ra-1 are shown separately from samples Ra-3 and Ra-4 for better legibility. **(b)** Plagioclase chemistry of sample Ra-4. **(c)** XMg – Si (pfu) and XMg – Ti (pfu) of biotite in sample Ra-3. **(d)** XMg – Si (pfu) plot of white mica. **(e)** Pseudosection of sample Ra-3 (representative of Raasberg type I samples) and **(f)** sample Ra-4 (Raasberg type II) with important mineral reactions highlighted by color. **(g)** Pseudosection of sample Ra-3 calculated without the chlorite model. **(h)** Volumes and XMg of chlorite, chloritoid, biotite and staurolite along a P–T path from 450 °C and 0.6 GPa to 540 °C and 0.4 GPa, indicated by the dashed line in **(g)**.

rolite are relatively homogeneous and lower in XMg compared to the other samples (Fig. 8a).

Biotite is not observed in sample Ra-4, a minor constituent of samples Ra-1 and Ra-2 and a matrix-forming mineral of sample Ra-3. In the latter, two habits of biotite are distinguished. Bt_1 forms large aggregates of coarse-grained, obliquely oriented biotite that are intergrown with muscovite and oriented oblique to Sn (Fig. 6g, h). This coarse-grained population is also included in Cld_1 (Fig. 6f) and possesses the same round quartz and apatite inclusions as Cld_1 and staurolite. Bt_2 is fine-grained and oriented parallel to Sn in the matrix or intergrown with Cld_2 in strain shadows of resorbed staurolite (Fig. 6g). Biotite is homogeneous in terms of Ti content (0.07–0.12 apfu). Matrix biotite (both Bt_1 and B_2) exhibits slightly lower XMg and higher Si contents compared to Bt_1 included in Cld_1 (Fig. 8c).

In sample Ra-4, two types of plagioclase are observed: (1) albitic plagioclase, partially replaced by coarse, randomly oriented muscovite (Pl_{ab}, $X_{an} = 0.02$–0.1), and (2) oligoclase (Pl_{ol}, Xan = 0.22–0.24; Fig. 8b), partially resorbed by kaolinite along cracks (Fig. 7c). Remnants of albitic plagioclase are commonly observed in the matrix (Fig. 7b). In some layers, the rock matrix is dominated by coarse-grained plagioclase of both types, with relatively straight albeit overprinted boundaries between the different types (inset Fig. 7c). In other samples, plagioclase is not observed, aside from strongly resorbed relics included in Cld_1. These samples, however, contain peculiar aggregates of quartz; very fine-grained, unidentified clay minerals; and Fe hydroxides that are overgrown by coarse-grained muscovite and biotite, spanning several millimeters in size. These aggregates are interpreted as sericitized pseudomorphs of plagioclase (labeled Pl* in Fig. 6b, c, h).

All samples contain both ilmenite and rutile. We distinguish several types based on morphology and microstructural position. Ilm_0 is most prominent in sample Ra-4, where it exists as numerous small (< 50 µm), typically subhedral round crystals that form a distinct inclusion pattern of staurolite and chloritoid aggregates (Fig. 7b–c). In other samples, this type only occurs as an inclusion of bright allanite porphyroblasts (Fig. 9b). Ilm_1 is the dominant ilmenite type in all Raasberg samples. It forms euhedral, lath-shaped blasts ranging between 50 and 200 µm in length. Numerous inclusion of small, round quartz and apatite grains are typical, especially in sample Ra-3. Smaller Ilm_1 grains are typically parallel to Sn, whereas larger grains tend to grow oblique to Sn. Ilm_2 forms tiny ilmenite needles (< 10 µm length) that typically precipitate along cleavage planes of Cld_2 and muscovite around inclusions of staurolite and, in sample Ra-3, biotite (Fig. 6d, f). Ilm_2 is also observed in the matrix of sample Ra-3 associated with Bt_1 aggregates. Rt_0 is rarely observed as small inclusions of Ilm_1 and staurolite. Rt_2 forms as a pseudomorphic replacement of Ilm_1 together with anhedral, fine-grained chlorite. This replacement is systematically observed in all samples regardless of the microstructural position of Ilm_1 (matrix and inclusion; Fig. 6e, h). Note also that Ilm_1 unaffected by the replacement coexists next to layers where it is fully replaced by Rt_2 pseudomorphs (Fig. 6e).

5.2 REE bulk rock pattern and REE mineralogy

Whole-rock REE patterns of the Raasberg samples exhibit a pronounced positive Eu anomaly relative to the average upper-crust composition (Fig. S12). Samples Ra-2 and Ra-4 are characterized by a high REE content relatively enriched in M+HREEs. In contrast, the whole-rock REE content of samples Ra-1 and Ra-3 is lower, and the enrichment of M+HREEs relative to LREEs is subtle. The Raasberg samples exhibit variable and complex REE mineral assemblages. Based on the REE mineralogy, samples Ra-1, Ra-2 and Ra-3 are grouped as "type I" samples that contain allanite porphyroblasts with a zoned REE epidote overgrowth. Sample Ra-4 represents a "type II" sample that exhibits highly complex allanite and REE epidote microstructures and additionally contains monazite and xenotime. Small (< 20 µm) fluorapatite and tiny zircon (< 2 µm) is ubiquitous in all samples, often appearing in foliation-parallel layers (Fig. 7c). Details of individual samples are given in Table 4 and summarized below.

Based on petrographic and chemical characteristics, we differentiate several types of allanite or REE epidote. All samples contain bright, euhedral or subhedral allanite porphyroblasts that are characterized by high total REE+Th+U contents (> 0.5 apfu), high Th / U ratios and enrichment in L+MREEs (Fig. 9c, d, i, j). The allanite contains numerous fine-grained (< 10 µm) inclusions of quartz, ilmenite and apatite that delineate an internal foliation (Fig. 9a, b). In sample Ra-4, subordinate small monazite and xenotime inclusions also occur (Fig. 9e). Additionally, small REE-rich epidote inclusions are common in the bright porphyroblasts (Fig. 9b, e); however, only one epidote inclusion was large enough for EPMA analysis. Like its host, L+MREEs dominate the REE pattern, but the total REE+Th+U content is lower (0.24 apfu; Fig. 9i, j). Note that these inclusions occasionally form along the phase boundary between quartz inclusions and the LREE-rich allanite host (Fig. 9e).

In type I samples, the allanite porphyroblasts are rimmed by a zoned REE epidote overgrowth (Fig. 9a-b). This overgrowth lacks fine-grained inclusions and is characterized by lower REE+Th+U contents (< 0.5 apfu) than the bright porphyroblast (Fig. 9c). REE patterns vary depending on the sample; bright zones (dotted red lines in Fig. 9a–b) are generally enriched in M+HREEs, whereas in darker zones (dotted light blue lines in Fig. 9a–b) the allanite endmember is defined by the HREE content that decreases towards the margin (Fig. 9c–d). Internally, the overgrowth zones may show irregular or oscillatory chemical zoning rather than a simple core-to-rim trend (Fig. 9a–b).

In type II sample Ra-4, allanite and REE epidote phase relationships are more complex. In the rare occasion where

https://doi.org/10.5194/ejm-36-943-2024

Table 4. Allanite and REE epidote types in Raasberg samples.

Sample	Lith. type	Description	Color code	Morphology	Abundance	BSE Z contrast	Total REE+Th+U	REE zoning pattern	Th / U
Ra-1	type I	bright Aln porphyroblast	black	euhedral porphyroblasts, < 100 µm	few (5–10 grains per thin section)	bright, homogeneous (patchy in high-contrast images)	0.73–0.7 apfu	enriched in L+MREE low HREE < 0.02 pfu	high Th / U
Ra-1	type I	zoned Ep overgrowth, bright	red	10–30 µm wide rim overgrowing porphyroblasts	common around porphyroblasts	bright, may show oscillatory zoning	0.02–0.19 apfu	enriched in HREE, decreased towards rim	low Th / U
Ra-1	type I	zoned Ep overgrowth, dark	light blue		common around porphyroblasts	dark, may show oscillatory zoning	low REE (< 0.04 apfu)		low ThO_2 (< 0.08 wt %), UO_2 bdl[a]
Ra-3	type I	bright Aln porphyroblast	black	subhedral porphyroblasts, numerous, fine-grained inclusions	common (15–20 grains per thin section)	bright, homogeneous (patchy in high-contrast images)	0.50–0.72 apfu	enriched in L+MREE low HREE	high Th / U, ThO_2 < 0.38 wt %, UO_2 bdl[a]
Ra-3	type I	Ep inclusion	purple	along phase boundary of quartz inclusion and Aln	common in bright porphyroblast	dark, internally variable	not analyzed	not analyzed	not analyzed
Ra-3	type I	zoned Ep overgrowth, bright	red	discontinuous overgrowth on Aln or euhedral porphyroblasts	common	bright, internal heterogeneity due to oscillatory zoning	0.14–0.48 apfu	enriched in M+HREE L+MREE decrease towards rim	variable Th / U, highest ThO_2 (up to 0.62 wt %)
Ra-3	type I	zoned Ep overgrowth, dark	light blue		common	dark, internal heterogeneity due to oscillatory zoning	0.01–0.24 apfu	enriched in HREE, decrease towards rim	low Th / U, highest UO_2 (up to 0.08 wt %)
Ra-4	type II	bright Aln porphyroblast	black	euhedral Aln porphyroblasts, up to 800 µm long	uncommon (< 5 grains per thin section)	bright, homogeneous (patchy in high-contrast images)	0.69–0.78 apfu	enriched in L+MREE low HREE (< 0.02 apfu) La/Nd decrease towards rim	ThO_2 < 0.53 wt %, high Th / U (> 10)
Ra-4	type II	porphyroblast rim	dark blue	10–30 µm wide rim around Aln porphyroblasts	rare relics around one Aln porphyroblast	dark, homogeneous	0.23–0.33 apfu	enriched in HREE	low Th / U (< 5)
Ra-4	type II	Ep inclusion	purple	along phase boundary of quartz inclusion and Aln	common in bright porphyroblast	intermediate, internally variable	0.24 apfu	enriched in L+MREE	
Ra-4	type II	patchy Ep aggregate	yellow	elongated aggregates, up to 1 mm long	common (~ 15 grains per thin section)	patchy, highly variable, micron-scale heterogeneity	0.44–0.77 apfu	enriched in L+MREE HREE enriched towards rim of aggregate	variable to low Th / U
Ra-4	type II	zoned Ep overgrowth, bright	red	in cracks of Aln porphyroblasts, overgrowth on patchy aggregate, neoblasts in matrix adjacent to Aln blasts and patchy aggregates	commonly associated with Aln porphyroblasts and REE Ep aggregates	bright, internal heterogeneity due to patchy zoning	0.78–0.29 apfu	L+MREE > HREE	low Th / U (mostly < 10)
Ra-4	type II	zoned Ep overgrowth, dark	light blue			dark, internal heterogeneity due to patchy zoning	0.48–0.20 apfu	HREE > L+MREE	UO_2 < 0.10 wt %, low Th / U (mostly < 5)

[a] bdl: below detection limit of EPMA (~ 0.02 wt % UO_2).

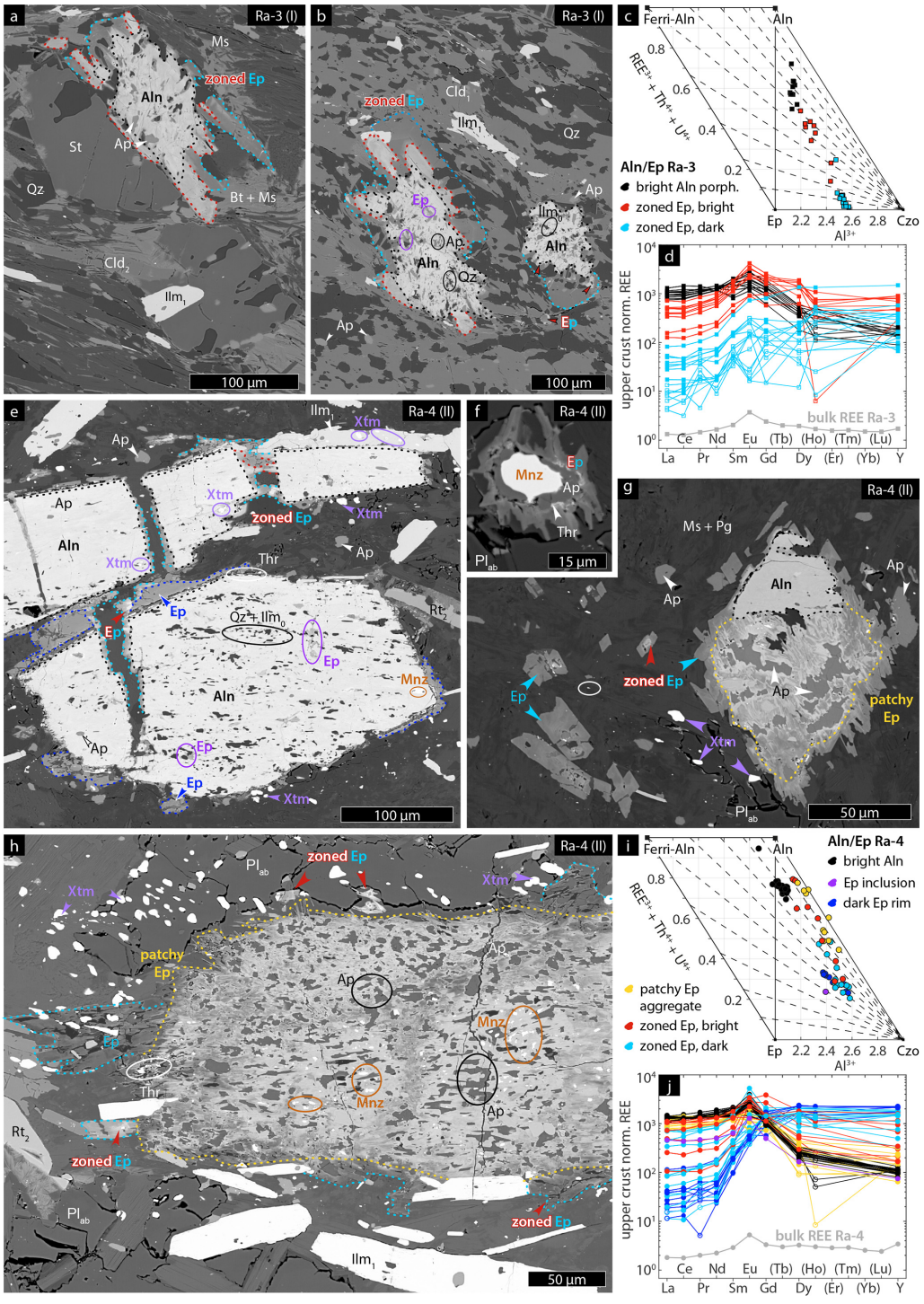

Figure 9. BSE–SEM images illustrating phase relationships of REE minerals and EPMA data of allanite and REE epidote in samples Ra-3 **(a–d)** and Ra-4 **(e–i)**. Sample name and lithological type given in the upper right corner. Colored labels and dotted lines indicate different types of allanite and REE epidote. Monazite (orange) and xenotime (purple) are also highlighted. **(a–b)** Zoned allanite and REE overgrowth in sample Ra-3 (type I) adjacent to staurolite and included in Cld_1. **(e–h)** Phase relations of allanite, REE epidote, monazite and xenotime in type II sample Ra-4. **(e)** Bright allanite porphyroblasts with relics of a dark epidote rim and zoned REE epidote forming in cracks. **(f)** Monazite in the matrix rimmed by a corona of apatite and zoned REE epidote. **(g)** Bright allanite porphyroblast partially replaced by patchy REE epidote aggregate with apatite inclusions. **(h)** Large patchy REE epidote aggregate with numerous apatite and small monazite inclusions surrounded by xenotime crystals. **(c, i)** Al (pfu) vs. REE+U+Th (pfu) plots illustrating compositional variation in allanite and REE epidote of sample **(c)** Ra-3 and **(i)** Ra-4 in the clinozoisite (Cz) – epidote (Ep) – ferriallanite (Ferri-Aln) – allanite (Aln) system. Dashed lines represent lines of constant Fe oxidation state. **(d, j)** REE distribution normalized by the average upper crust of Rudnick and Gao (2003) of allanite and REE epidote in **(d)** Ra-3 and **(j)** Ra-4.

two allanite porphyroblasts are adjacent to each other, relics of a 10–30 µm wide, dark REE epidote rim (dotted dark blue lines in Fig. 9e) are present. This REE epidote is characterized by low total REE+Th+U contents (0.23–0.35 apfu) and is enriched in HREEs (Fig. 9i, j). Only a few bright allanite porphyroblasts are present in this sample (Fig. 9e). Instead, REE epidote aggregates that consist of numerous small, chemically highly heterogeneous REE epidote crystals are more common. These elongated aggregates are often oriented parallel to Sn (Fig. 9h) and in some cases directly replace the allanite porphyroblast (Fig. 9g). Distinct features include numerous apatite inclusions and a highly variable *Z* contrast, which reflects micron-scale variations in REEs (± Th, U), resulting in a patchy appearance (Fig. 9g, h). The interface between apatite and REE epidote is highly serrated, particularly in darker, REE-poor areas of the aggregates (Fig. 9h). The patchy REE epidote exhibits higher Al contents and greater variability in total REE contents than the bright allanite (Fig. 9i). REE patterns are similar but with lower L+MREE concentrations and slightly increased HREEs, particularly towards the margins (Fig. 9j). A zoned REE epidote generation similar to the overgrowth in type I samples also exists in sample Ra-4. It occurs in cracks of bright allanite and the dark REE epidote rim and as overgrowth on the patchy aggregates, thus clearly postdating the growth of these allanite and REE epidote types. Additionally, small (< 50 µm) euhedral neoblasts occur in the vicinity of bright allanite and patchy REE epidote aggregates (Fig. 9e, g). Bright zones are characterized by larger REE contents relatively enriched in L+MREEs, whereas dark zones are REE-poor and enriched in HREEs (Fig. 9i). Individual crystals typically show decreasing L+MREE and increasing HREE contents from core to rim (Fig. 9i, j) and can exhibit internal oscillatory or patchy zoning (Fig. 9g).

Clusters of small (< 10 µm) monazite are rarely found in the matrix but are commonly included in patchy REE epidote (Fig. 9h). In rare cases where isolated monazite grains occur in the matrix adjacent to REE epidote, it typically possesses a rim of apatite, which is overgrown by zoned REE epidote (Fig. 9f). The LREE content in monazite is homogeneous, and M+HREE shows some variation irrespective of the microstructural position (0.08–0.10 apfu; Fig. S3). Xenotime exists as small (∼ 15 µm) satellite grains surrounding both allanite porphyroblast and the patchy REE epidote aggregates (Fig. 9e, g, h). Chemically, it is homogeneous with 0.19 apfu M+HREE substituting for yttrium (Fig. S3).

5.3 Geochronology

U–Th–Pb dating of allanite and REE epidote in sample Ra-3, which was chosen as being representative of type I samples, yields a Pb/U–Th isochron date of 275.2 ± 6.2 Ma (*n*: 45; MSWD: 2.2; Fig. 5b), which is consistent with the Tera–Wasserburg lower intercept date of 275 ± 10 Ma (Fig. S8). Using the Th / U ratio and the Y content, individual analyses are correlated with chemically distinct zones in the REE epidote (Fig. 5e). The bright allanite porphyroblast is characterized by a high Th / U ratio, a low Y concentration and a high Pb_0 content. The $^{238}U / ^{206}Pb$ ratio is generally higher in the zoned overgrowth, particularly in the bright Y-rich domain. Comparing the Pb_0-corrected dates of individual spots, no age difference between the various REE epidote domains is apparent.

In sample Ra-4, we attempted U–Th–Pb dating of all allanite and REE epidote types. However, no age data could be obtained for the dark porphyroblasts rim (Fig. 9e), since only small relics of this zone are present. Analyses can be grouped according to their Th / U ratio, with high Th / U ratios (50–170) corresponding to bright porphyroblasts and low Th / U ratios (< 30) and higher $^{238}U / ^{206}Pb$ ratios corresponding to the patchy porphyroblasts and the zoned overgrowth. On a Tera–Wasserburg diagram, bright porphyroblast analyses plot close to the *y* axis, indicating a dominant Pb_0 contribution. A regression calculated through both Th / U populations (one outlier excluded) yields a lower intercept date of 87.1 ± 3.5 Ma (*n*: 35; MSWD: 1.3; Fig. S9), which is roughly consistent with Eo-Alpine metamorphism. However, on the isochron plot (Fig. 5c) it is apparent that these groups comprise in fact different age populations, rendering the Tera–Wasserburg lower intercept date as geologically meaningless. Due to its high Pb_0 content, no meaningful date could be calculated for the bright porphyroblast. The low Th / U population yields a Pb/U–Th isochron date of 108.8 ± 6.6 Ma (*n*: 13, MSWD: 3.1). An elevated Ca content suggests the presence of apatite in most analyses (Fig. 5f).

The U–Th–Pb data of sample Ra-3 indicate that both the bright allanite and the zoned REE epidote overgrowth formed during Permian metamorphism. The age data of sample Ra-4 provide evidence that the patchy porphyroblasts and the zoned overgrowth formed during Eo-Alpine metamorphism. The significance of the various allanite and REE epidote types in this sample requires consideration of both the Permian and the Eo-Alpine evolution. Their significance, the role of monazite and apatite inclusions, and reasons explaining the contrasting evolution of REE phases in type I and type II samples are discussed in detail in Sect. 7.1.

5.4 Interpretation of Permian and Eo-Alpine parageneses and fabrics

All Raasberg samples preserve reaction microstructures. Together with geochronological evidence of both Permian and Eo-Alpine metamorphism, this indicates that a Permian assemblage was partially overprinted during the Eo-Alpine event. It is, however, challenging to interpret whether phase relationships represent replacement microstructures or intergrowth in equilibrium. We here assume that all samples have experienced the same *P*–*T* evolution as they were collected close together. This implies that the contrasting phase assemblages can be explained by differences in the bulk rock

chemistry, deformation and fluid influence. We here use our petrographic observations combined with the results of thermodynamic forward modeling to determine the Permian and Eo-Alpine equilibrium assemblages and assess the influence of contrasting bulk rock compositions on the respective peak assemblage. Finally, we discuss the effect of deformation on resulting microstructures.

We first consider phase relationships between Fe–Mg alumosilicates (chloritoid, staurolite, biotite, chlorite). Since staurolite shows uniform resorption by chloritoid, the replacement of Permian staurolite with Eo-Alpine chloritoid would be an obvious interpretation. This explanation is consistent with reaction microstructures observed in sample Ra-4, where large, partially resorbed staurolite is replaced by rosette-shaped chloritoid aggregates intergrown with muscovite and paragonite according to the following unbalanced reaction (e.g., Nosenzo et al., 2022; Yardley and Baltatzis, 1985):

$$\mathrm{St} + \mathrm{K^+} + \mathrm{Na^+} \rightarrow \mathrm{Cld} + \mathrm{Ms} + \mathrm{Pg}. \quad \text{(R1)}$$

This interpretation, however, fails to explain the two types of chloritoid ($\mathrm{Cld_1}$ and $\mathrm{Cld_2}$) observed in the other samples. Straight phase boundaries between staurolite and large $\mathrm{Cld_1}$ blasts (Fig. 6c) infer equilibration across the phase boundary. Therefore, we propose that $\mathrm{Cld_1}$ coexisted with staurolite during Permian peak metamorphism. The similar inclusion spectrum and both phases overgrowing Sn support this interpretation. $\mathrm{Cld_2}$, on the other hand, is interpreted as an Eo-Alpine chloritoid generation which formed together with muscovite at the expense of staurolite. Remnants of biotite, which are associated with staurolite in samples Ra-1 and Ra-2, likely represent relics of the Permian assemblage. In sample Ra-3, where biotite is a matrix-forming mineral, the two different habits (coarse-grained $\mathrm{Bt_1}$ and fine-grained $\mathrm{Bt_2}$) may be interpreted as Permian and Eo-Alpine generations, respectively. This is supported by the presence of $\mathrm{Bt_1}$ inclusions in large $\mathrm{Cld_1}$ blasts and intergrowth of $\mathrm{Bt_2}$ and $\mathrm{Cld_2}$ around resorbed staurolite (Fig. 6g–f). Tiny $\mathrm{Ilm_2}$ needles formed at the expense of Ti in biotite and staurolite. Thus, staurolite and biotite breakdown in samples Ra-1, Ra-2 and Ra-3 is summarized according to the following unbalanced reaction:

$$\mathrm{St} + \mathrm{Bt_1} \rightarrow \mathrm{Cld_2} + \mathrm{Ms} \pm \mathrm{Ilm_2} \pm \mathrm{Bt_2}. \quad \text{(R2)}$$

Chlorite, finally, is restricted to late-stage shear bands in sample Ra-3 or observed as the local alteration of staurolite remnants. It is therefore attributed to late-stage retrogression and not considered as part of the Eo-Alpine peak assemblage.

P–T pseudosections calculated for all Raasberg samples show a similar topology for the reactions between Fe–Mg aluminosilicates. The positively sloping chloritoid-out and chlorite-out reactions coincide with the staurolite-in and biotite-in reactions with a narrow *P–T* interval between ∼ 480 °C and 0.1 GPa and the intersection with the garnet stability field at ∼ 535 °C and 0.45 GPa (Fig. 8e–f). Although modeling results are consistent with staurolite and biotite forming during higher-grade Permian metamorphism and chloritoid forming during the lower-grade Eo-Alpine overprint, the model fails to explain the two generations of chloritoid. Model results generally show a very restricted *P–T* range where staurolite and chloritoid coexist in equilibrium. However, staurolite incorporates significant amounts of Ti and Zn, both of which are not considered in the model. Therefore, its stability field may be extended towards lower temperatures compared to model results. Another inconsistency between model and observation concerns biotite and chlorite. We found that in all samples, significant amounts of chlorite are calculated below staurolite stability, whereas the amount of chloritoid is generally underestimated by the model. The misfit is particularly striking in the sample Ra-3, which has the highest XMg bulk rock content. Below 520 °C, only minor amounts of chloritoid (∼ 2 vol %) but ∼ 18 vol % chlorite are calculated, which is inconsistent with the exceptionally large $\mathrm{Cld_1}$ blasts of this sample. Test calculations performed excluding the chlorite model not only yield more realistic chloritoid and biotite proportions but also produce chloritoid compositions that match observations more closely (Fig. 8g–h). These findings suggest that the chlorite model applied here (Holland and Powell, 2011) overestimates chlorite stability at low-*P–T* conditions for the considered Al-rich chemistry, which affects the predicted composition and number of other Fe–Mg phases (chloritoid, staurolite, biotite).

Sample Ra-4 exhibits a different mineralogy of the Na- and Ca-bearing phases compared to other samples. Comparing pseudosections of samples Ra-3 and Ra-4, we can infer that this is due to the higher bulk rock $\mathrm{Na_2O}$ content in sample Ra-4 (Table 2), which influences the stability fields of plagioclase and paragonite (Fig. 8e–f). In sample Ra-3, the onset of the plagioclase stability field in the low-pressure, high-temperature (LP-HT) area of the pseudosection approximately coincides with the chloritoid–staurolite transition, whereas paragonite is restricted to high-pressure conditions ($P > 1.0$ GPa). The presence of plagioclase pseudomorphs and resorbed relics included in $\mathrm{Cld_1}$ is consistent with the notion that plagioclase is part of the Permian peak assemblage. Sample Ra-4 contains two compositionally distinct types of plagioclase ($\mathrm{Pl_{ab}}$ and $\mathrm{Pl_{ol}}$) and paragonite. The stability fields of plagioclase and paragonite overlap at 0.2–0.4 GPa, bounded by positively sloping reaction curves. Plagioclase, regardless of which type, is always partially resorbed. Where both plagioclase types are present, they show similar microstructural features (i.e., large grain size) and relatively straight phase boundaries. Thus, we propose that $\mathrm{Pl_{ab}}$ and $\mathrm{Pl_{ol}}$ correspond to peristerite pairs and formed in thermodynamic equilibrium at Permian peak metamorphic conditions. Although thermodynamic modeling fails to reproduce the peristerite solvus, it is expected at similar *P–T* conditions as corroborated by staurolite–chloritoid phase relations at the transition between the greenschist and amphibolite fa-

cies (Habler et al., 2009; Holland et al., 2022; Maruyama et al., 1982).

The growth of paragonite occurred together with chloritoid during the Eo-Alpine overprint.

Finally, ilmenite and rutile phase relations are considered. Ilm_1 is interpreted, too, as part of the Permian peak assemblage, which is consistent with the chloritoid–staurolite transition within the ilmenite stability field. The partial replacement of Ilm_1 by rutile (Rt_2) postdating the growth of large Cld_1 and formation of Ilm_2 related to staurolite and biotite breakdown strongly suggests that ilmenite and rutile coexisted in equilibrium during Eo-Alpine metamorphism.

To summarize, the Permian peak assemblage consists of staurolite, chloritoid (Cld_1), biotite (Bt_1), plagioclase in samples Ra-1 to Ra-3 and staurolite + plagioclase (Pl_{ab}+ Pl_{ol}) in sample Ra-4, with ilmenite (Ilm_1)+ muscovite + quartz in all samples. The Eo-Alpine overprint caused the formation of chloritoid (Cld_2)+ ilmenite (Ilm_2)+ rutile (Rt_2), as well as biotite (Bt_2) in sample Ra-3 and paragonite in sample Ra-4. Retrograde reactions involve minor replacement of staurolite by Fe-rich chlorite and the formation of kaolinite and other clay minerals at the expense of plagioclase remnants. Permian peak phases grew randomly oriented over the Sn foliation, which consequently formed during prograde Permian metamorphism. The extent of Eo-Alpine deformation varies depending on the sample. In sample Ra-4, the formation of paragonite pseudomorphs after staurolite and the preservation of the Ilm_0 inclusion pattern indicate that the Eo-Alpine overprint was static. In samples Ra-1 and Ra-2, the deflection of Sn around Cld_1 indicates minor Eo-Alpine deformation that caused the bending and slight rotation of Cld_1 porphyroblasts. In sample Ra-3, the development of strain shadows filled with Cld_2 around staurolite porphyroblasts is interpreted as a result of pervasive Eo-Alpine shearing. Cld_1 blasts were stretched and recrystallized to a fine-grained chloritoid + quartz aggregate, where stretching is accommodated by quartz precipitating along cleavage planes of Cld_1 (Fig. 6f).

5.5 Permian and Eo-Alpine *P–T* conditions

As outlined in Sect. 5.4., the Permian mineral assemblage is not precisely reproduced by pseudosection modeling due to limitations of the solid solution models (i.e., Ti and Zn in staurolite) and potential overestimation of chlorite stability. Although the chlorite appears to affect the composition and volumes of chloritoid, we found that the position of the staurolite-chloritoid transition does not change regardless of whether chlorite is considered in the model and is predicted between 470–530 °C and 0.1–0.4 GPa in all Raasberg samples (Fig. 8e, f). We therefore assume that these inconsistencies have a minor effect on the accuracy of our *P–T* estimates. Permian peak *P–T* conditions reside close to the staurolite-chloritoid transition and below the stability field of garnet, which closely coincides with the onset of plagioclase stability. Thus, the Permian assemblage is consistent with *P–T* conditions at 500–530 °C and 0.2–0.4 GPa.

P–T conditions of the Eo-Alpine overprint are delimited by the stability field of garnet towards high pressure and plagioclase in sample Ra-4 towards low pressure. The temperature is constrained by ilmenite and rutile coexisting in equilibrium. Altogether, the Eo-Alpine phases are consistent with *P–T* conditions of 440–480 °C and 0.4–0.8 GPa (Fig. 8e, f).

6 Rossegg samples

6.1 Petrography and microstructures

The two garnet–chloritoid-bearing graphitic micaschist samples (Ro-1 and Ro-2) are characterized by the interlayering of mica-rich layers that contain garnet and chloritoid porphyroblasts and up to centimeter-thick quartz layers subparallel to the main foliation Sn (Fig. 10a, b). Both samples are Al-rich and depleted in Ca compared to Shaw's (1956) pelite and exhibit average Na contents (Table 2). Quartz layers possess pseudomorphs of a fibrous mineral that was replaced by fine-grained oxides (inset Fig. 10b). In the matrix, two different white mica populations are identified (Fig. 10g). Fine-grained muscovite (Ms1) pigmented by graphite defines the main foliation Sn; it is overgrown by a second generation of coarse-grained white mica. Compositionally, the coarse-grained mica population is characterized by both K-rich (Ms_2) and Na-rich white mica (Pg; Fig. 10c–g). Some Ms_2 crystals exhibit chemical zoning with the maximum Si content in the core (3.15 apfu; Figs. 10g, 11d). In Ms_1, the Si content is lower ($\sim$ 3.11 apfu). Garnet forms large, euhedral porphyroblasts spanning up to 4 mm in diameter. Fine-grained graphite inclusions delineate an internal foliation that continuously merges into the matrix foliation Sn (Fig. 10a). Inclusions in garnet are ilmenite, chloritoid, apatite, monazite and zircon. Some garnet crystals possess an inclusion zoning with a pigmented core and a clear rim (Fig. 10a). Chemically, garnet is characterized by an almandine-rich composition and continuous core-to-rim zoning (Fig. 11a). In the largest garnet of sample Ro-1, Xalm increases from 0.72 to 0.8, whereas Xsps exhibits a bell-shaped decrease from 0.11 in the core to 0.01 at the rim. Xprp increases slightly from 0.08 to 0.1. Xgrs gradually decreases from 0.07 in the core to 0.01 at the rim.

Chloritoid forms large (up to 3 mm long) porphyroblasts that are generally oblique to the foliation. Fine-grained graphite inclusions delineate an internal foliation that continuously merges into the external foliation (Fig. 10a, d). Chloritoid exhibits cracks filled with chlorite and small (< 5 µm) ferroan gahnite crystals (Fig. 10). Chemically, chloritoid is characterized by XMg between 0.1 and 0.15 with no clear trend from core to rim and negligible Mn content, except two analyses from chloritoid included in garnet (Fig. 11b). Cross-shaped zones with weakly foliated coarse-grained muscovite and paragonite are developed adjacent to, or intergrown with,

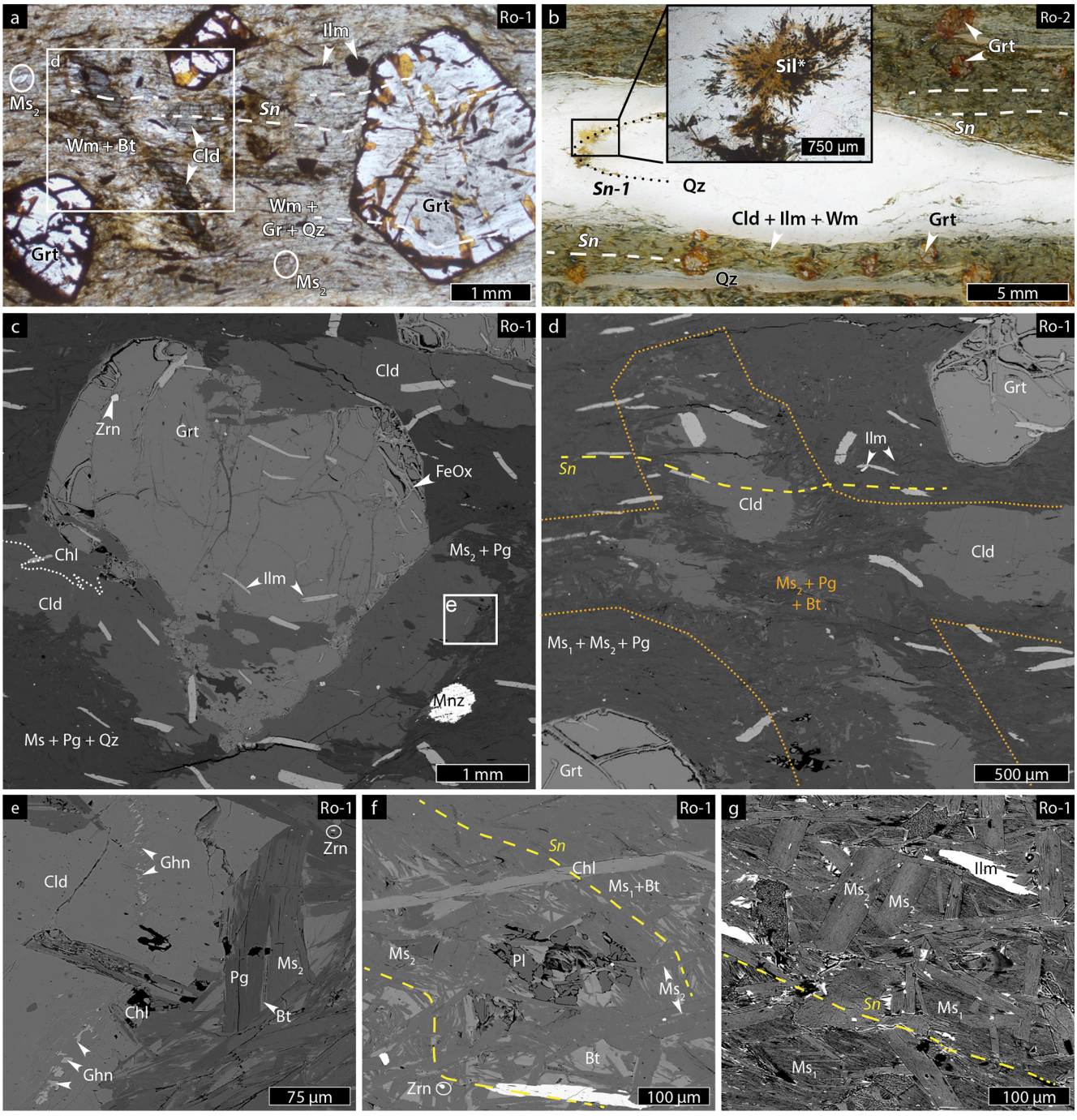

Figure 10. Transmitted light photomicrographs **(a–b)** and representative BSE–SEM images **(c–g)** illustrating microstructural features and phase assemblages of Rossegg samples (sample name given in the upper right corner). **(a)** Large garnet and chloritoid porphyroblasts overgrowing the Sn foliation defined by ilmenite and fine-grained graphite. **(b)** Interlayering of a foliated, mica-rich matrix with garnet and chloritoid porphyroblasts and quartz layers that are subparallel to the foliation. Inset shows a relic fold hinge in the quartz vein that contains a fibrous pseudomorph (labeled Sil*). **(c)** Garnet is intergrown with large chloritoid and chlorite in a matrix of muscovite and paragonite. **(d)** Cross-shaped chloritoid porphyroblasts are intergrown with coarse-grained muscovite, paragonite and subordinate biotite. The dotted orange line highlights the boundary to matrix micas. **(e)** Tiny gahnite inclusions and chlorite in a crack in chloritoid. **(f)** Relics of plagioclase associated with biotite overgrown by randomly oriented muscovite (Ms_2) and chlorite. **(g)** High-contrast BSE image of matrix-forming white mica illustrating microstructurally different white mica types: fine-grained, Sn-parallel muscovite (Ms_1) and coarse-grained, obliquely growing muscovite (Ms_2) that is sometimes chemically zoned.

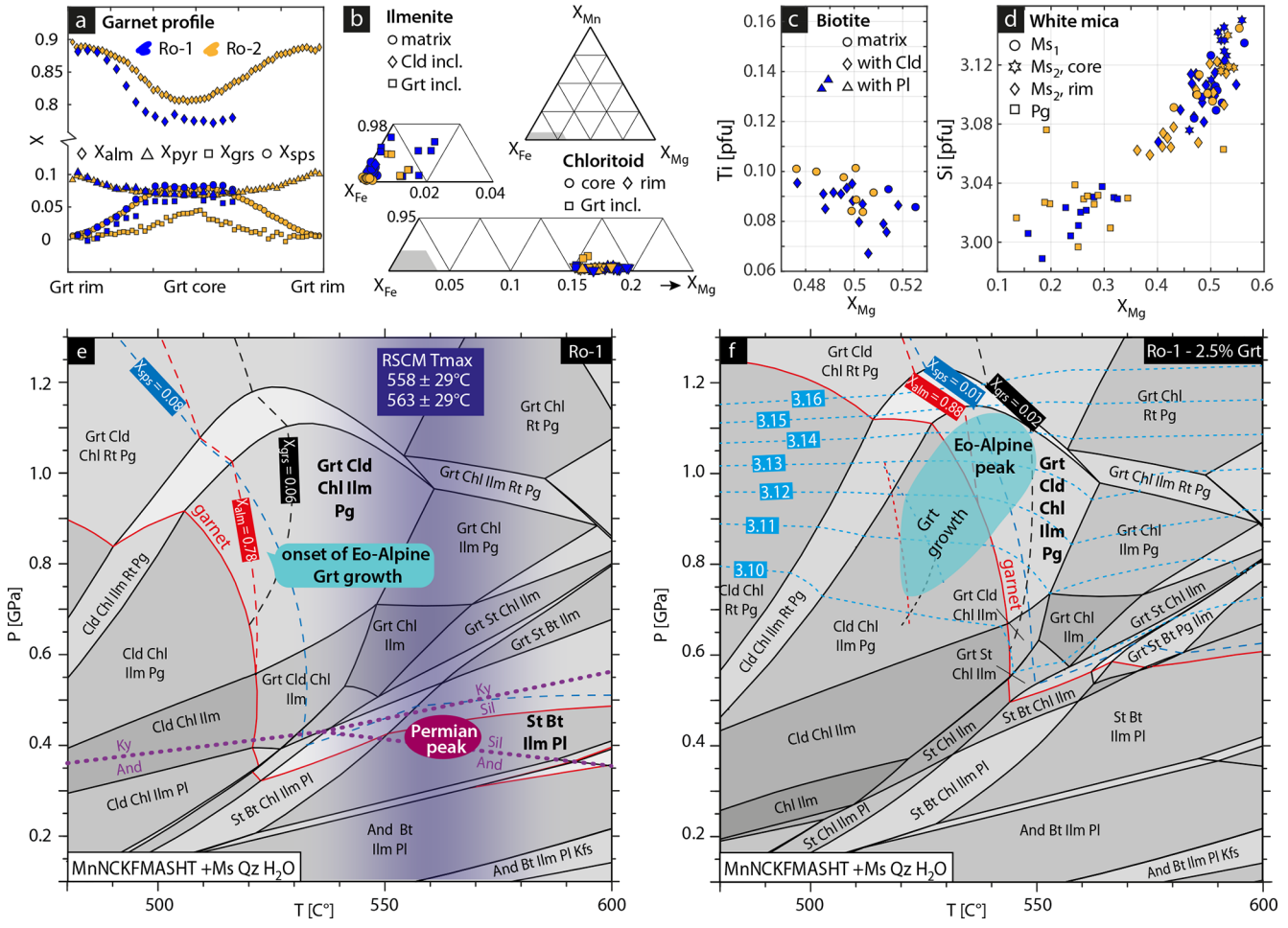

Figure 11. Mineral chemistry of **(a)** garnet, **(b)** chloritoid, ilmenite, **(c)** biotite and **(d)** white mica measured with EPMA for Rossegg samples. The same color code applies for **(a)**–**(d)**. **(a)** High-resolution garnet profile of sample Ro-2 (length 1.44 mm) representative of garnet zoning in Rossegg samples and partial profile (length 2 mm) through the largest garnet of sample Ro-1. Profile lengths are normalized for better comparison. **(e)** *P*–*T* pseudosection of sample Ro-1 (Table S13). Isopleths corresponding to the observed garnet core composition are shown as dashed lines. Dotted purple lines indicate stability fields of aluminosilicates. Maximum temperatures from RSCM are shown as the dark blue shaded area. **(f)** *P*–*T* pseudosection of sample Ro-1 considering 2.5 mol % garnet fractionation (Table S15). Isopleths corresponding to the observed garnet rim composition are shown as dashed lines. Dash-dotted blue lines are Si (pfu) isopleths in muscovite-rich white mica.

chloritoid porphyroblasts (Fig. 10a, c). Biotite that is otherwise absent in the matrix occurs here too or is associated with a few remnants of albitic plagioclase (Fig. 10d–f). Compositionally, it is fairly homogeneous in composition with XMg around 0.5 and Ti between 0.08 and 0.1 apfu (Fig. 11c). Two analyses of biotite associated with plagioclase remnants, however, show an elevated Ti content (0.13 apfu). Ilmenite that is strongly pigmented by graphite, and rarely rutile, is mostly parallel, and occasionally oblique, to the foliation. Chemically, ilmenite included in garnet exhibits higher XMg and XMn values than ilmenite in the matrix and included in chloritoid (Fig. 11b).

6.2 REE bulk rock pattern and REE mineralogy

The whole-rock REE compositions shows a flat pattern on upper-crust normalized REE plots for both samples (Fig. S12). The REE mineral assemblage is dominated by monazite that coexists with apatite, ubiquitous but tiny (< 10 µm) zircon, and rare anhedral xenotime. Apatite is strongly resorbed and highly porous and occasionally found associated with monazite (Fig. 12a). In both samples, large (up to 500 µm), elongated monazite crystals or aggregates are preferably oriented parallel to Sn (Fig. 12a–b). Monazite in sample Ro-2 was dated and is described in more detail; sample Ro-1 monazite follows similar compositional trends (Fig. S5). Typically, monazite is stained by fine-grained graphite and quartz and subordinate ilmenite and white mica inclusions. High-contrast BSE images and element maps in-

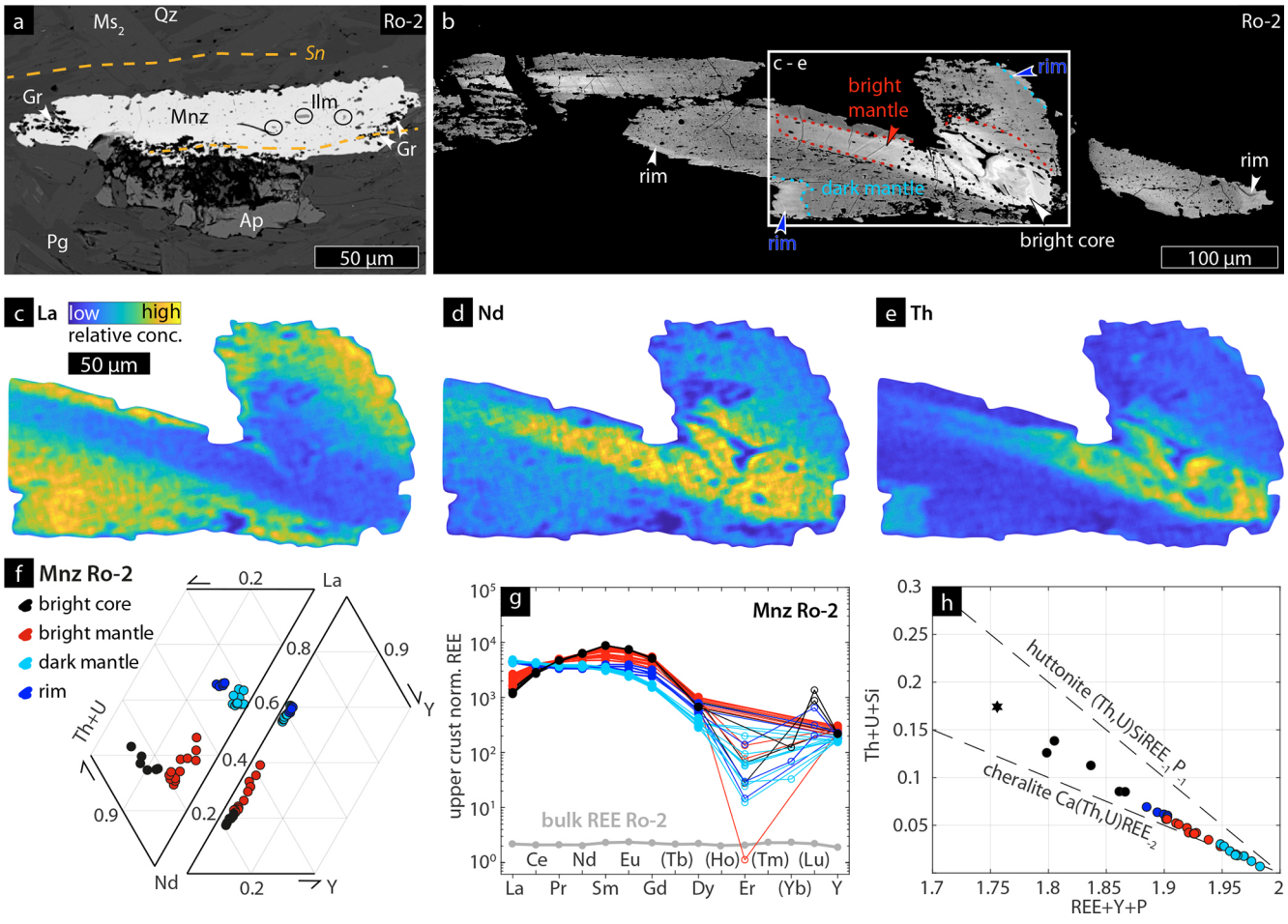

Figure 12. REE phase relationships and monazite chemistry in Rossegg samples. **(a)** Large monazite associated with strongly resorbed apatite. Tiny graphite and ilmenite delineated an internal foliation that is parallel to the matrix schistosity (Sn). **(b)** High-contrast BSE image of monazite showing internal chemical zoning. Colored labels and dotted lines indicate different types of monazite: bright core (black), bright mantle (red), dark mantle (light blue) and rim (dark blue). The white box shows the position of element maps of **(c)** La, **(d)** Nd and **(e)** Th. **(f)** La–Nd–Th+U and La–Nd–Y ternary plots of monazite. **(g)** REE distribution normalized by the average upper crust of Rudnick and Gao (2003) of monazite. Elements in brackets were not analyzed in all datasets. **(h)** REE+P vs. Th+U+Si (pfu) of monazite showing huttonite and cheralite substitutions.

dicate internal chemical zoning: a bright core, a bright mantle, a dark mantle and a discontinuous bright rim (Fig. 12b). The bright core is relatively enriched in MREEs and depleted in LREEs. Towards the mantle, the REE profile becomes progressively flatter with maximum La / Nd ratios in the dark mantle zone (Fig. 12g). This zoning is also illustrated by the inverse relationship of Nd and La on element distribution maps (Fig. 12c–d). Yttrium content is low (< 0.83 wt % Y_2O_3) and generally decreases towards the mantle (Fig. 12f). Thorium and uranium are incorporated in monazite through the cheralite and, to a lesser extent, huttonite substitutions, generally decreasing in concentration from core to mantle (Fig. 12h). In some grains, complex internal zoning within the core is attributed to variations in Th (Fig. 12e) with up to 14 wt % ThO_2 in the brightest zones. The Th / U ratios are highest in the core (~ 80) and decrease towards the dark mantle (~ 30). Most monazite grains possess a discontinuous, thin rim, which is typically only 2–3 µm wide but may reach up to 15 µm width on monazite faces normal to Sn (Fig. 12b). The La / Nd ratio and LREE concentrations at the rim are comparable to those in the dark mantle, but M+HREE (Eu–Lu+Y) is relatively enriched (Fig. 12f, g). Moreover, the rim is chemically characterized by an elevated Th+U content with ThO_2 up to 6.45 wt % and Th / U between 55 and 80 (Fig. 12h).

6.3 Geochronology

Sample Ro-2 was selected for monazite U–Pb dating since it contains monazite grains with Th-rich rims that are wider than 10 µm. On a U–Pb Tera–Wasserburg plot, monazite dates are discordant, suggesting a variable Pb_0 contribu-

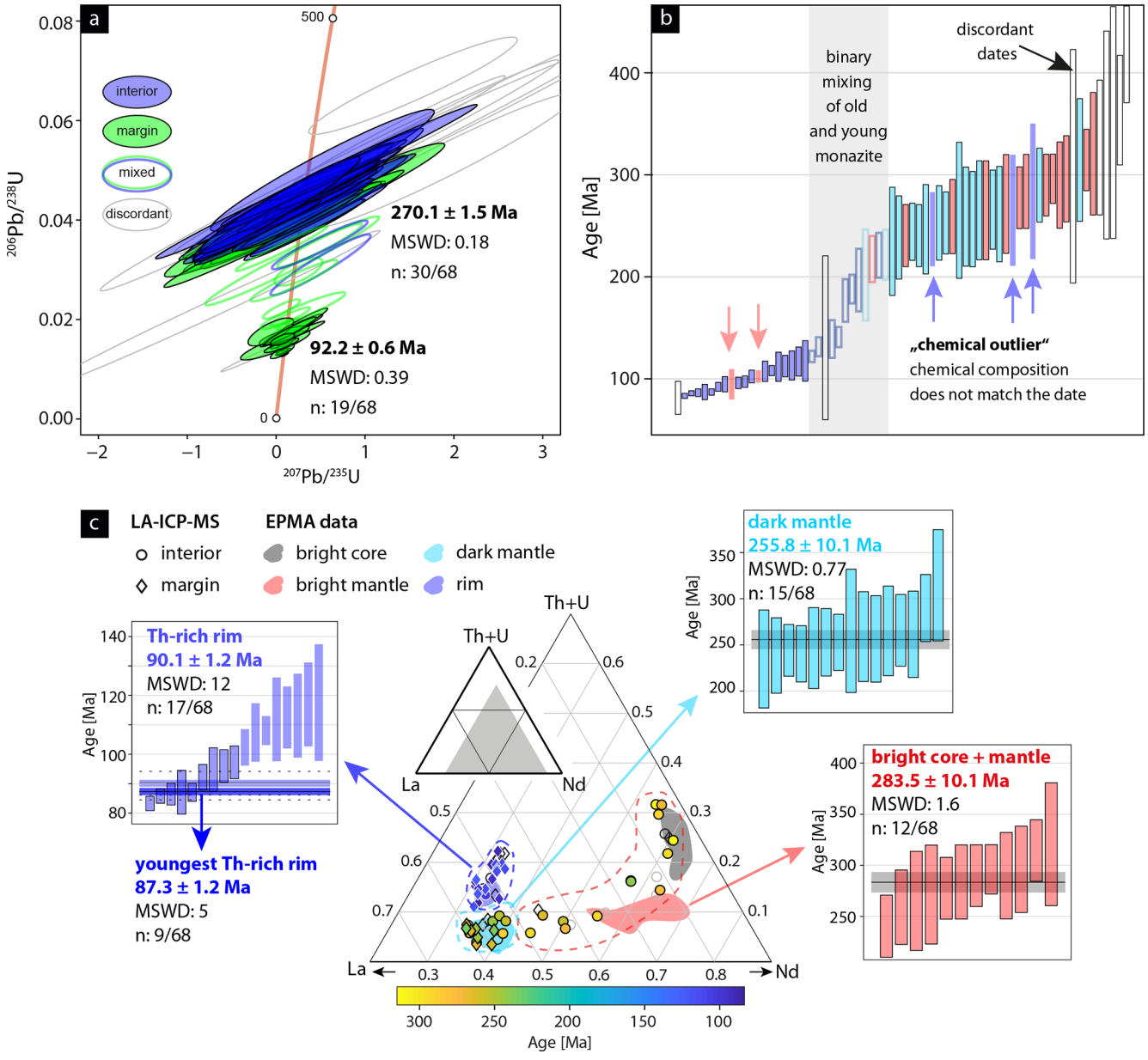

Figure 13. Geochronological data of monazite in sample Ro-2. **(a)** Wetherill concordia diagram with ^{204}Pb-corrected dates. **(b)** Weighted mean ages color-coded by chemical domain: red – bright core plus mantle; light green – dark mantle; blue – rim. Open bars represent discordant dates. **(c)** Nd–La–Th+U ternary plot illustrating the chemical composition of the monazite LA-ICP-MS data color-coded by date and weighted mean ages calculated for each chemical domain. Gray open symbols represent discordant dates; black open symbols represent "chemical outliers" that are excluded from the weighted mean age calculation.

tion (Fig. S10). The ^{204}Pb-corrected dates show two distinct clusters that yield concordia ages of 270.1 ± 1.4 Ma (n: 30, MSWD: 0.18), encompassing most analyses of the monazite interiors, and 92.2 ± 0.6 Ma (n: 19, MSWD: 0.39), involving mostly analyses from the monazite margins (Fig. 13a). A total of 8 analyses that are discordant after correction and 11 concordant analyses that lie between the main clusters were excluded from the age calculations. On a La–Nd–U+Th ternary plot, LA-ICP-MS analyses show excellent agreement with the monazite chemistry determined using EPMA (Fig. 13c). Analyses that correspond to the older population generally define the chemical domain of the monazite core and mantle, whereas the younger population chemically matches the rim domain. However, there are a few exceptions, termed "chemical outliers": analyses of the older population that plot in the chemical domain of the rim and analyses of the younger population that plot in the chemical domain of the monazite core and mantle (Fig. 13b). Con-

sidering only U–Pb dates that plot in the expected chemical domain, analyses from the monazite core and bright mantle yield a weighted mean age of 283.5 ± 10.1 Ma (n: 12, MSWD: 1.6), the dark mantle yields a weighted mean age of 255.8 ± 10.1 Ma (n: 15, MSWD: 0.77) and the rim yields a weighted mean age of 90.1 ± 1.2 Ma (n: 17, MSWD: 12). Including only the youngest dates of the rim, a weighted mean age of 87.3 ± 1.2 Ma (n: 9, MSWD: 5) is calculated.

Monazite forms euhedral porphyroblasts and contains the same phases as inclusions that are also found in the matrix, corroborating a metamorphic origin. Monazite core and mantle domains dominantly yield older U–Pb dates (243–315 Ma), suggesting that the main portion of monazite formed during Permian metamorphism. Apparent U–Pb dates that lie between the main clusters (139–222 Ma) represent binary mixing of the outermost potions of the dark mantle and the rim and have no geological relevance. The younger dates of the Th-rich rim and a few younger dates in the monazite interior indicate limited recrystallization during the Eo-Alpine metamorphism. Mechanisms of monazite formation are discussed in Sect. 7.1 and 7.2.

6.4 Interpretation of Permian and Eo-Alpine parageneses and fabrics

Based on microstructural constraints, we can identify distinct mineral parageneses and establish the timing of their growth relative to the main foliation Sn. Although these parageneses could theoretically represent stages of a single metamorphic cycle, our new monazite ages reveal unambiguously their polymetamorphic origin during the Permian and Eo-Alpine events. Clarifying which phases define the equilibrium assemblage during each event is complicated by the ambiguous relationship between monazite and porphyroblasts like garnet and chloritoid. Moreover, the microstructural perspective alone does not disclose whether certain phases (e.g., biotite) represent remnants of an earlier assemblage or reflect local bulk rock heterogeneity. Additional constraints are provided by the fact that the two events are characterized by markedly different P–T gradients: low pressure and high temperature during the Permian (Knoll et al., 2023, and references therein) and medium to high pressure during the Eo-Alpine events (Schuster et al., 2004, and references therein). Thermodynamic forward modeling is therefore employed not only to determine P–T conditions, but also to predict which phases are expected to equilibrate at high- and low-pressure conditions.

In garnet-bearing metapelites of the UAU, garnet that displays discontinuous chemical zoning is often cited as a diagnostic feature for polymetamorphism (e.g., Gaidies et al., 2006; Habler et al., 2009; Schantl et al., 2015; Schuster et al., 2001). In our samples, the gradual core–rim chemical zoning of garnet indicates a single growth stage, raising the question of why only one event – and which one – produced the garnet. A pseudosection calculated for sample Ro-1 predicts garnet in a stability field above 0.3–0.4 GPa (Fig. 11e). The garnet core composition, particularly the Ca content, is also indicative of pressures above 0.6 GPa (Fig. 11e). Therefore, we suggest that garnet formed during Eo-Alpine metamorphism. Conversely, the low-pressure Permian assemblage is garnet-free. This interpretation is consistent with its euhedral shape and general lack of overprint, aside from minor alterations by Fe oxides, which are attributed to weathering at surface conditions. Chloritoid, chlorite, paragonite and Si-rich muscovite (Ms_2) grew oblique to the Sn foliation. Particularly the presence of paragonite and the Si-rich Ms_2 composition are indicative of relatively higher pressures (Fig. 11d). We suggest that these phases together with garnet define the Eo-Alpine peak assemblage, which implies that minerals oriented parallel to the Sn foliation predate Eo-Alpine peak metamorphism. Ilmenite is, similar to Permian monazite, mostly aligned parallel to Sn and strongly included by graphite. We therefore assume it formed already during the Permian event but remained stable during the Eo-Alpine overprint, since no replacement by rutile is observed.

Although monazite grew primarily during Permian metamorphism, our findings suggest that the main mineral assemblage largely re-equilibrated during the Eo-Alpine metamorphic imprint. However, a few observations allow inferences about the Permian mineral assemblage. Few remnants of albite associated with Ti-rich biotite probably comprise relics of the Permian assemblage. Thermodynamic modeling also supports this, since both phases are predicted in the low-pressure, garnet-free area of the pseudosection (Fig. 11d). Staurolite and andalusite, which would also be expected according to the model, were not observed. However, certain characteristics of chloritoid infer that it indeed replaced pre-Alpine staurolite, and similar features have been described in other parts of the UAU (e.g., Habler et al., 2009; Piber et al., 2008). The tiny gahnite (Zn-spinel) inclusions frequently observed in chloritoid may infer staurolite, which can incorporate a significant amount of Zn in its crystal structure, as a precursor. Feenstra et al. (2003) also described gahnite and chloritoid forming due to staurolite breakdown for very Al-rich metabauxite rocks in a high-pressure setting. The commonly observed intergrowth of chloritoid with Ms_2 and paragonite ($\pm$ biotite) can be interpreted as a result of staurolite replacement given the case that K^+ and Na^+ are available in excess (e.g., Habler et al., 2009; Yardley and Baltatzis, 1985; sample Ra-4 of this study). In fact, the shape of these intergrowths is reminiscent of cross-shaped, twinned staurolite in some cases (Fig. 10d). Biotite, which is also present in these intergrowths, could be a relic of the Permian assemblage. Alternatively, it formed locally during the Eo-Alpine to balance changes in XMg between staurolite and chloritoid. This would explain its relatively low Ti content, consistent with lower temperatures (Henry et al., 2005; Wu and Chen, 2015). In summary, we argue that these observations provide indirect, yet convincing, evidence for the existence of Permian staurolite, which was replaced following the un-

balanced reaction:

$$\mathrm{St} + \mathrm{K^+} + \mathrm{Na^+} + \rightarrow \mathrm{Cld} + \mathrm{Ms_2} + \mathrm{Pg} \pm \mathrm{Ghn} \pm \mathrm{Bt}. \quad \text{(R3)}$$

Finally, the conspicuous pseudomorphs observed in quartz veins might represent pseudomorphs of fibrous sillimanite, which is described in Permian mineral assemblages of the UAU and equivalent tectonic units in the Carpathians (e.g., Habler and Thöni, 2001; Jeřábek et al., 2008; Schuster et al., 2001).

6.5 Permian and Eo-Alpine *P–T* conditions

Maximum temperatures are constrained by RSCM thermometry of two samples at 558 ± 29 °C and 563 ± 29 °C (Fig. 11e, Table 3). The stability field of the presumed Permian assemblage defined by St + Bt + Ilm + Pl + Ms + Qz intersects with the peak temperatures at 0.25–0.4 GPa. Sillimanite is only predicted at > 590 °C and does not coexist with staurolite. It is, however, reasonable to assume that quartz veins were not in equilibrium with the matrix; thus sillimanite could appear at 540 °C (Fig. 11e). Therefore, we interpret Permian peak *P–T* conditions at 560 °C and 0.4 GPa.

The Eo-Alpine peak assemblage defined by Grt+Cld+Chl+Ilm+Pg+Ms+Qz is stable at 510–560 °C and 0.5–1.1 GPa (Fig. 11e). Garnet core isopleths intersect at ∼ 520 °C and 0.7–1.0 GPa, which are interpreted as the onset of Eo-Alpine garnet growth. Garnet isopleths corresponding to the rim composition are not reproduced in the pseudosection. The bell-shaped profile of the Mn content in garnet (Fig. 11a), however, indicates that fractionation of the garnet core from the matrix must be considered (e.g., Evans, 2004). Thermodynamic modeling predicts ∼ 2.5 mol % of garnet within the stability field of the observed assemblage, which is consistent with the estimated garnet mode from the thin section (4.9 vol % garnet calculated at 550 °C and 1 GPa vs. 4.5 % modal amount of garnet in the thin section of Ro-1). To calculate the effective bulk rock composition during growth of the garnet rim, 2.5 mol % of the average garnet core composition (Xalm = 0.81; Xprp = 0.08; Xsps = 0.06; Xgrs = 0.05) corresponding to 4.9 vol % was subtracted from the bulk rock composition of sample Ro-1 (Table S15). In the resulting pseudosection, isopleths corresponding to the garnet rim composition are reproduced at 540–550 °C and 1.0–1.1 GPa (Fig. 11f). Additional constraints on the peak pressure are derived from the composition of chemically zoned, coarse-grained white mica (Ms_2). The maximum Si content observed in the core (3.15 apfu) suggests that Ms_2 formed at the Eo-Alpine pressure peak. Combining garnet isopleths and Si in potassic white mica, we interpret Eo-Alpine peak metamorphic conditions at 550 °C and 1.0–1.1 GPa.

7 Discussion

Our sample set contains allanite, REE epidote, monazite and xenotime that formed during two metamorphic events under conditions ranging from greenschist to amphibolite facies. Phase relationships and microstructures of the dated REE minerals are highly complex, justifying an in-depth discussion of factors controlling REE mineral crystallization (*P–T* conditions, bulk rock composition and deformation). Sketches illustrating the REE mineral evolution for each locality are presented in Fig. 14 and provide the basis for discussing the *P–T–t–D* evolution of both tectonic units during the Permian and Eo-Alpine events. We conclude the discussion by outlining the broader implications of our results for Cretaceous tectonics in the Austroalpine Unit.

7.1 Primary prograde REE mineral formation during Permian metamorphism

7.1.1 Allanite and REE epidote

Allanite and REE-rich epidote in samples Hi-1 and Ra-3 yield Permian U–Th–Pb dates. Euhedral allanite porphyroblasts (Aln_1) characterized by an LREE-rich composition and an internal foliation delineated by numerous fine-grained inclusions are common in both Hirschkogel and Raasberg samples. Only the latter contain a zoned REE-rich epidote (Ep_1) overgrowth on Aln_1, which is characterized by fewer, coarser-grained inclusions. Compositionally, lower total REE contents and relative enrichment of M+HREEs are typical. In sample Ra-4 (Raasberg type II), relics of the HREE-rich epidote rim (Fig. 9e) are interpreted as Ep_1 remnants, which were too small to be dated. A similar Aln_1/Ep_1 compositional pattern has been interpreted as prograde growth zoning at upper greenschist to lower amphibolite facies grade (e.g., Boston et al., 2017; Janots et al., 2008; Wing et al., 2003). We therefore interpret Aln_1 formation during prograde Permian metamorphism at greenschist facies conditions to be coeval with chloritoid formation. Only in the Raasberg samples were Permian peak temperatures sufficiently high (∼ 520 °C) to allow the formation of the Ep_1 overgrowth. Geochronological data of sample Ra-3 showed no age difference between Aln_1 (bright LREE-rich core) and Ep_1 (zoned overgrowth), confirming it formed during the same event. The grain size increase of inclusions in Aln_1 and Ep_1 is explained by the coarsening of the pre-existing matrix with increasing temperatures, also strengthening our interpretation.

Janots et al. (2008) explained the growth zoning of Aln_1 and Ep_1 by the successive breakdown of monazite and xenotime with increasing metamorphic grade. Their interpretation is applicable to our samples, supported by the presence of tiny xenotime grains in Hirschkogel samples where no Ep_1 rim is developed and the absence of xenotime in the matrix of Raasberg type I samples (Ra-1, Ra-2, Ra-3) that contain

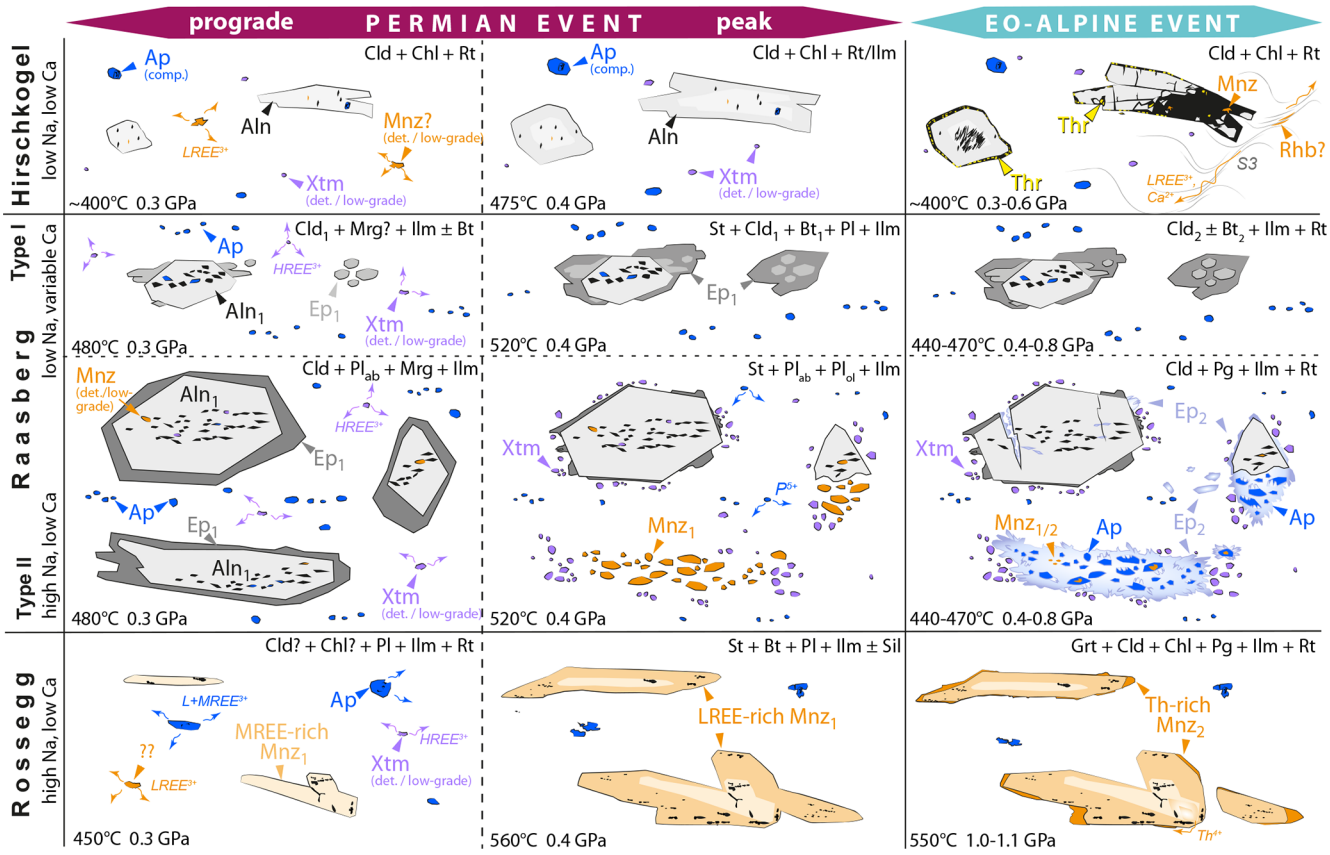

Figure 14. Sketches representing the REE mineral evolution during Permian and Eo-Alpine metamorphism at each locality as outlined in Sect. 7.1 and 7.2. The main mineral assemblage is given in the upper right corner (plus muscovite and quartz, which are present during all stages); metamorphic conditions are given in the lower left corner of each panel. Small arrows indicate relative scale of REE (± Th, P, Ca) transport in the fluid.

Aln_1 with Ep_1 rims. Except for a few, small monazite inclusions in Aln_1 in sample Ra-4, only limited evidence regarding the LREE-rich precursor exists. The chemical zoning of Aln_1 provides additional insight into the nature of the LREE-rich precursor. In all samples that contain Aln_1, we observe a gradual systematic increase in Nd and decrease in La from core to rim. This is at odds with Janots et al. (2008), who report distinct growth zones with Nd-rich cores and La-rich rims. They explain this zoning by compositional inheritance of a heterogeneous monazite population of partly detrital, party low-grade metamorphic origin. Applying the same logic to our samples, a compositionally relatively homogeneous, presumably low-grade metamorphic monazite population may have provided LREEs for Aln_1. According to Janots et al. (2008), phosphorous released from the breakdown of monazite and xenotime is incorporated in apatite that crystallized coevally with Aln_1/Ep_1. Euhedral, unzoned apatite grains are abundant in both Raasberg and Hirschkogel samples. In the latter, metamorphic overgrowths on detrital apatite grains are also common. The growth of metamorphic apatite is therefore plausible for all samples that contain Aln_1 and Ep_1. According to Janots et al. (2008), the following reaction can be written to describe the formation of Aln_1 and Ep_1, where Ca is most likely supplied by detrital or low-grade metamorphic silicate minerals (e.g., margarite – Livi et al., 2002; detrital feldspar – Janots et al., 2008).

$$\mathrm{Mnz + Xtm + Chl + Ca^{2+} \rightarrow Aln_1 + Ep_1 + Ap + Cld} \quad \text{(R4)}$$

7.1.2 Monazite and xenotime

In the Raasberg type II sample Ra-4, clusters of small xenotime blasts typically surround both partially resorbed Aln_1 porphyroblasts and patchy REE epidote aggregates. These xenotime blasts are in turn overgrown by Permian peak phases (e.g., Ilm_1, Pl_{ab}). Therefore, we suggest that in this sample, Aln_1 and Ep_1 were destabilized at Permian peak conditions and partially replaced by clusters of small monazite and xenotime blasts. This replacement is described by a reaction modified from Janots et al. (2008), where Ca^{2+} is likely incorporated into plagioclase:

$$\mathrm{Aln_1 + Ep_1 + Ap \rightarrow Mnz_1 + Xtm_1 + Ca^{2+}}. \quad \text{(R5)}$$

Permian monazite (Mnz_1), however, was largely replaced during the Eo-Alpine overprint (Sect. 7.2.1) and only exists

as relic grains included in, or adjacent to, patchy REE epidote aggregates. This interpretation is supported by Permian peak P–T conditions determined for Raasberg samples, which coincide with the upper stability limit of allanite and REE epidote (Boston et al., 2017; Janots et al., 2008; Spear, 2010; Wing et al., 2003). Moreover, the in situ replacement of large porphyroblasts by numerous small "satellite grains" is a typical replacement microstructure for this prograde reaction (e.g., Boston et al., 2017; Janots et al., 2008).

In Rossegg samples, the U–Pb dating of monazite core and mantle domains dominantly yields older U–Pb dates (243–315 Ma), suggesting that the main portion of monazite formed during Permian metamorphism (Mnz_1). In contrast to sample Ra-4, its microstructural features are inconsistent with Mnz_1 formation from the prograde breakdown of allanite. In such a case, a patchy, irregular monazite zoning pattern would be expected (Skrzypek et al., 2018) instead of the large, isolated blasts with pronounced core–rim chemical zoning. Thus, we confidently exclude the prograde breakdown of metamorphic allanite as a monazite formation reaction in this sample. Lacking direct evidence for the monazite LREE-rich precursor, the REE zoning pattern in Mnz_1 may provide additional constraints. The Mnz_1 core of sample Ro-2 exhibits a pronounced enrichment of MREEs, which is comparable to the zoning of greenschist facies monazite from other studies (e.g., Rasmussen and Muhling, 2007, 2009). This sample also contains abundant, strongly corroded apatite that can incorporate significant amounts of MREEs (Henrichs et al., 2019; Hermann, 2002). Following Janots et al. (2006), we suggest that the breakdown of detrital apatite released MREEs and phosphorous which then were incorporated in Mnz_1. Additionally, slightly increased HREE concentrations in the core and mantle domains infer a contribution of xenotime during incipient stages of monazite growth. Thus, Mnz_1 formation is summarized by the following equation:

$$\text{LREE-rich phase} + \text{REE-rich Ap} + \text{Xtm} \rightarrow Mnz_1. \quad \text{(R6)}$$

The complex growth zoning of Mnz_1 infers growth over a prolonged period, consistent with the spread observed in the Mnz_1 U–Pb dates. Protracted monazite growth is also consistent with thermodynamic modeling of Spear and Pyle (2010), who demonstrated that monazite records a range of ages rather than single points during the metamorphic episode if allanite is absent.

7.2 Secondary REE mineral formation during the Eo-Alpine overprint

7.2.1 Overprint in the allanite stability field

We first consider samples that contain pristine Permian Aln_1 ($\pm$ Ep_1) porphyroblasts (Hi-1, Raasberg type I samples). Despite substantial overprint of the main mineral assemblage, Permian allanite is not resorbed, suggesting that the Eo-Alpine event also occurred within the allanite stability field. Since no reactive precursor REE phase was present during the second event, no Eo-Alpine allanite generation formed. Therefore, the geochronological data only record Permian metamorphism in these samples (Fig. 5a–b).

In contrast, the Raasberg type II sample Ra-4 contains Permian monazite (Mnz_1). The breakdown of Mnz_1 during the Eo-Alpine overprint in the allanite stability field provided LREEs for the growth of a new REE epidote generation (Ep_2), according to Reaction (4). Microstructural and compositional properties of Ep_2, however, strongly depend on the inherited variations in the Permian REE mineral assemblage. Relic monazite grains surrounded by coronae of apatite and zoned REE-rich epidote are direct petrographic evidence for Mnz_1 replacement. Similar coronae are described as typical reaction microstructures forming during retrograde overprint of high-grade (igneous or metamorphic), large monazite crystals (e.g., Broska et al., 2005; Finger et al., 1998; Gasser et al., 2012; Hentschel et al., 2020). We propose that the same replacement mechanism produced the patchy REE epidote–apatite aggregates. Instead of a large monazite crystal, clusters of small Mnz_1 blasts that replaced prograde Permian Aln_1 were present. If phosphorous is conserved over the reaction front as suggested for the corona formation (Hentschel et al., 2020), the apatite inclusions reflect pre-existing small Mnz_1 grains. Thus, the apparent pseudomorphic replacement of Aln_1 by Ep_2–Ap (Fig. 9g) involved in fact two stages of in situ replacement (Fig. 14): (1) replacement of Aln_1 by clusters of small Mnz_1 blasts at the Permian peak (comparable to Fig. 5i of Janots et al., 2008) and (2) replacement of Mnz_1 clusters by the Ep_2–Ap aggregate. Few relics of Aln_1 ($\pm$ Ep_1) remained stable during the Eo-Alpine overprint. Here, Ep_2 is present as a thin, strongly zoned REE epidote overgrowth that chemically resembles Ep_1 in type I samples but forms preferably in cracks of the Permian porphyroblasts (Fig. 9e). For Ep_2 formation, the reaction proposed by Hentschel et al. (2020) for the allanite–apatite corona formation is modified:

$$Mnz_1 + Ca^{2+} + Si^{4+} + Al^{3+} + Fe^{2+/3+} + M + \text{HREE}^{3+} \rightarrow Ep_2 + \text{Ap} \pm \text{Thr} \pm Mnz_2. \quad \text{(R7)}$$

Here, the breakdown of Permian plagioclase provided Ca for Ep_2 and apatite. Tiny monazite inclusions within the Ep_2–Ap aggregate, particularly those mantled by apatite, may represent remnants of Permian monazite (Mnz_1). Alternatively, the formation of secondary monazite (Mnz_2) by dissolution–reprecipitation of Mnz_1 is possible (Hentschel et al., 2020). Finger et al. (2016) suggested Mnz_2 formation from the reversal of the Ep_2–Ap-forming reaction, a process that seems plausible particularly within bright, REE-rich parts of the Ep_2–Ap aggregates with relatively straight grain boundaries (Fig. 8e). Local variations in the Ca and Na concentration in the fluid greatly affect whether monazite is preserved, altered by dissolution–reprecipitation or replaced by REE epidote

(Budzyn et al., 2011). Thus, we acknowledge that a combination of monazite-forming (or preserving) mechanisms is appropriate and must be taken into account when interpreting the geochronological data of sample Ra-4.

7.2.2 Overprint in the monazite stability field

In most Hirschkogel samples, small, euhedral monazite crystals that occur in cracks of, or adjacent to, Permian allanite blasts are typically associated with tiny thorite crystals. Additionally, isolated monazite grains exist in the matrix. Regardless of its microstructural position, monazite exhibits similar REE patterns and low Th and Y contents. We therefore assume that all monazite in the Hirschkogel samples formed due to allanite resorption at low temperature, comparable to reports by Bollinger and Janots (2006) and Krenn and Finger (2007). Low Th contents are typical of monazite that forms at low-grade conditions associated with thorite (Rasmussen and Muhling, 2009); thus we can write the following reaction:

$$\mathrm{Aln} + \mathrm{Ap} \rightarrow \mathrm{Mnz} + \mathrm{Thr} + \mathrm{Ca}^{2+}. \quad \text{(R8)}$$

Monazite thermometry yields temperatures broadly consistent with monazite formation at low temperature (343–482 °C; Gratz and Heinrich, 1997), although the large dispersion may indicate incomplete equilibration between matrix xenotime and monazite that are not in direct contact. In sample Hi-1, minor allanite resorption and monazite formation likely occurred after Eo-Alpine peak metamorphism. In other Hirschkogel samples allanite resorption is more advanced, especially close to the S3 crenulation cleavage (Fig. 3c), indicating that Eo-Alpine P–T conditions lie outside the allanite stability field. Strongly resorbed allanite is microstructurally replaced by quartz, chlorite and a corona of tiny thorite crystals, but only subordinate monazite (or a different LREE-rich phase) is present in direct contact with allanite. Here, an LREE-rich phase (monazite or rhabdophane) found in cracks of chloritoid is most likely a result of allanite breakdown.

In Rossegg samples, Eo-Alpine monazite (Mnz_2) formation is evinced by U–Pb dates ranging between 81 and 121 Ma. These dates correspond to the Th-rich rim on Permian monazite blasts. Partially reset U–Pb dates in the Permian Mnz_1 ("chemical outliers"; Fig. 11b) suggest that it served as source material for the rim, consistent with studies demonstrating metamorphic monazite growth at the expense of inherited monazite (Rasmussen and Muhling, 2007). The sharp compositional discontinuity between the Mnz_2 rim and the dark mantle and its preferable formation in sites normal to the schistosity (Fig. 12b) argues for a dissolution–reprecipitation formation mechanism of Mnz_2. Additionally, Mnz_2 overgrowth formation may have occurred, which is difficult to discern as the shape of the Mnz_1 grain prior to Eo-Alpine metamorphism is not known. Experiments demonstrated that Th-rich rims most likely form in the presence of alkali-bearing fluids (Harlov et al., 2011; Hetherington et al., 2010). Such fluid compositions are expected in our samples due to the dissolution of Permian plagioclase and formation of Eo-Alpine paragonite. Constraining the timing of Mnz_2 formation relative to the main mineral assemblage is not straightforward as direct phase contacts of monazite and garnet or chloritoid porphyroblasts (i.e., the Eo-Alpine peak assemblage) are lacking. In contrast to low-temperature monazite in Hirschkogel samples, the rim is enriched in Th, which is indicative of monazite crystallization at elevated temperatures (Rasmussen and Muhling, 2007; Seydoux-Guillaume et al., 2012). Thus, we interpret the formation of the Mnz_2 rim at, or close to, Eo-Alpine peak conditions.

In summary, significant secondary REE mineral formation is observed if the overprint occurred outside the stability field of the primary REE mineral assemblage. In cases where the overprint falls in the stability field of the primary REE mineral, primary allanite is preserved and secondary allanite does not form. Monazite on the other hand is more prone to recrystallization, facilitating the formation of secondary monazite.

7.3 Relative role of P–T and bulk rock composition for REE mineral stability

The reconstructed REE mineral evolution confirms that allanite and monazite generally do not coexist in equilibrium. Consistent with other studies, we find that allanite is stable at greenschist to lower amphibolite facies conditions and monazite forms both at lower- and higher-grade conditions (e.g., Bollinger and Janots, 2006; Janots et al., 2006, 2008, 2011; Krenn and Finger, 2007; Rasmussen et al., 2001; Wing et al., 2003). Xenotime remains stable at higher temperatures compared to monazite and may coexist with allanite (e.g., Hi-1 and Ra-4); its breakdown at higher temperatures explains the systematic prograde zoning with LREE-rich allanite cores and HREE-rich epidote rims (Janots et al., 2008). Furthermore, contrasting evolutions derived for different samples from the same locality that experienced identical P–T conditions (Fig. 14) underline the strong bulk rock chemistry control on stability limits. Our sample set confirms the influence of bulk rock CaO and $\mathrm{Al_2O_3}$ content on allanite and monazite stability, which is well established by other studies (e.g., Foster and Parrish, 2003; Hoschek, 2016; Krenn and Finger, 2007; Rasmussen and Muhling, 2009; Spear, 2010; Wing et al., 2003). For instance, the Eo-Alpine overprint in Hirschkogel samples at $\sim$ 400 °C corresponds to the low-temperature stability limit of allanite (Janots et al., 2008; Wing et al., 2003). In most samples, the overprint occurred outside the stability field of allanite, except for sample Hi-1. The high $\mathrm{Al_2O_3}$ content of sample Hi-1 (30.5 wt %) presumably increased allanite stability towards lower temperatures (Fig. 15a), thus preserving Permian allanite in this sample.

In other cases, bulk Ca and Al contents alone do not sufficiently determine allanite and monazite stability, which

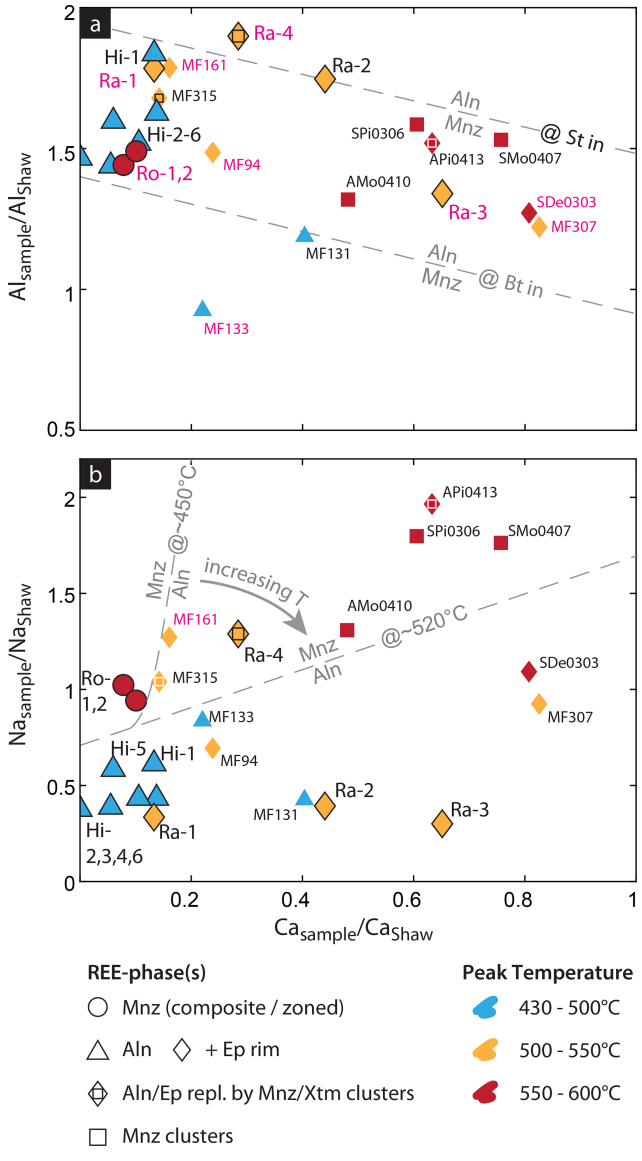

Figure 15. Bulk rock Ca, Al and Na contents normalized by Shaw's (1956) average low-grade pelite and compositional limits for allanite and monazite. Larger symbols are samples of this study; smaller symbols are from Janots et al. (2008). Symbols represent the REE mineral(s), color represents peak temperature and labels are sample names. Magenta labels are used if the REE mineral is inconsistent with the proposed compositional limits. **(a)** Normalized Ca vs. Al content and compositional limits of allanite and monazite at the biotite and staurolite isograd proposed by Wing et al. (2003). **(b)** Normalized Ca vs. Na contents and tentative compositional limits based on our sample set and data by Janots et al. (2008).

aligns with Boston et al. (2017) and Janots et al. (2008). For instance, compositional limits for Ca and Al proposed by Wing et al. (2003) predict metamorphic allanite as a precursor for Permian monazite in Rossegg samples (Fig. 15a), which is highly unlikely as discussed above (Sect. 7.1.2). Rossegg and Hirschkogel samples overlap in terms of bulk Ca and Al content (Fig. 15a), but metamorphic allanite formed only in the latter. Similarly, the model of Wing et al. (2003) incorrectly predicts allanite preservation for sample Ra-4 and allanite replacement by monazite for Raasberg type I samples (Fig. 15a). Janots et al. (2008) proposed the molar CaO / Na_2O ratio as the critical factor for the temperature of the prograde allanite breakdown. We suggest that the bulk rock Na content best explains both the absence and presence of metamorphic allanite in very Ca-poor Hirschkogel and Rossegg samples as well as contrasting Permian peak assemblages in the Raasberg samples (Fig. 15b). Elevated bulk rock Na contents increase the stability field of plagioclase towards higher pressures (Fig. 11f, g). This affects the stability limits of allanite, as both phases compete for Ca. In Na-rich Rossegg samples, albitic plagioclase formed during prograde Permian metamorphism (Fig. 10f). Because of the low bulk rock Ca content, it seems plausible that a sufficient amount of plagioclase, albeit of albitic composition, prevents the growth of allanite. In contrast, no plagioclase formed in Na-poor Hirschkogel samples; thus allanite grew as the main calcic phase.

Similarly, the upper stability limit of allanite is related to the bulk Na content and plagioclase formation. The Na-rich type II sample Ra-4 contains significantly larger amounts of plagioclase compared to Raasberg type I samples. Consequently, Aln_1/Ep_1 breakdown occurred at lower temperatures compared to Na-poor Raasberg type I samples where Aln_1/Ep_1 remained stable at the Permian peak. Hence, if bulk rock Na is relatively high ($Na/Na_{Shaw} > 1$), the prograde breakdown of allanite to monazite occurs at ~ 520 °C. Based on our sample set and published data (Janots et al., 2008), we propose tentative compositional limits for allanite and monazite in Ca vs. Na space (Fig. 15b). At ~ 450 °C, allanite can form in Ca-poor metapelites ($Ca/Ca_{Shaw} < 0.2$) if Na/Na_{Shaw} is below 0.6 (Hirschkogel samples). The Ca-poor and Na-rich Rossegg samples constrain a field in which no allanite will develop that is separated by a steep curve originating at $Na/Na_{Shaw} \sim 0.7$. With increasing temperatures, the curve becomes progressively shallower; at ~ 520 °C, the slope is constrained by samples with replacement microstructures of allanite by monazite at relatively higher Na / Ca ratios (e.g., Ra-4) and samples that preserve allanite with epidote rims at lower Na / Ca ratios (Ra-1, Ra-2, Ra-3).

The amount of REEs in the bulk rock appears to have no influence on whether allanite or monazite represents the stable LREE-rich phase, consistent with studies that assess allanite and monazite stability using thermodynamic modeling (Janots et al., 2007; Spear, 2010). The bulk rock REE composition may, however, affect the composition of whichever LREE-rich phase is present. For instance, anomalies in the bulk rock REE pattern are reflected in the REE pattern of the dominant REE-bearing mineral (e.g., positive Eu anomaly in Raasberg samples). Furthermore, the bulk rock Y (+HREE) content strongly influences xenotime stability at greenschist facies conditions which in turn determines the HREE con-

centration of the coexisting LREE-rich phase (e.g., Pyle et al., 2001). This may explain compositional variations comparing allanite and REE epidote in different Raasberg samples.

7.4 *P–T–t–D* evolution

7.4.1 Permian event

The obtained *P–T–t* data allow us to reconstruct Permian metamorphic conditions in both investigated tectonic units (Fig. 16). In the Schöckel Nappe (DG-NS), peak temperatures of 475 °C in higher structural levels (Hirschkogel samples) that increase to 520 °C at the base (Raasberg samples) at relatively low pressures of ∼ 0.3–0.4 GPa are consistent with the Permian LP-HT gradient (Fig. 16) and with regional RSCM data (Rantitsch et al., 2005). Previous studies attributed these temperatures to Eo-Alpine tectonics (Krenn et al., 2008; Rantitsch et al., 2005; Schantl et al., 2015), owing to ambiguous hitherto existing geochronological data (Gasser et al., 2010, and references therein). Our allanite and REE epidote ages in Hirschkogel and Raasberg samples unequivocally prove that these peak temperatures and thus the main metamorphic signature correspond to the Permian event. In sample Hi-1, the allanite Pb/U–Th isochron date of 261.3 ± 8.4 Ma corresponds to the crystallization of the dark mantle domain inferred from compositional data (Fig. 5b). The coarsening of matrix minerals postdating allanite growth likely occurred at the metamorphic peak; therefore the allanite age is attributed to the late prograde evolution. In sample Ra-3, we found no systematic difference in Pb_0-corrected dates for Aln_1 and Ep_1, indicating that the different growth stages of Aln_1 and Ep_1 cannot be resolved based on the U–Th–Pb data. Ilmenite inclusions imply the growth of Aln_1 in the ilmenite stability field. Therefore, the age of 275.2±6.2 Ma corresponds to prograde Permian metamorphism at 450–520 °C and 0.3–0.4 GPa.

The monazite date of the Rossegg sample confirmed that pre-Alpine metamorphism in the Waxenegg Nappe (KW-NS) corresponds to the Permian event, as already speculated by Schantl et al. (2015) based on the presence of polyphase garnet. In our case, for the garnet-free Permian assemblage we interpret peak *P–T* conditions of 560 °C and 0.4 GPa that are consistent with the Permian LP-HT gradient in the Austroalpine Unit (Fig. 16). The U–Pb monazite age data show that the main portion of monazite formed during Permian metamorphism, albeit partially overprinted during the Eo-Alpine event. Particularly in the Th-rich Mnz_1 core, we noted complex, irregular chemical zoning patterns that are linked to small-scale variation in Th (Fig. 12e). Such microstructures are typical for the dissolution and reprecipitation of monazite which can already occur at relatively low temperatures, as documented in experiments (< 400 °C; Grand'Homme et al., 2016, 2018; Seydoux-Guillaume et al., 2012). Young U–Pb dates that compositionally correspond to Mnz_1 ("chemical outliers"; Fig. 13b) also indicate (partial) resetting of the U–Pb system in Permian Mnz_1. If these analyses compromised by alteration are excluded, we find that U–Pb dates in the MREE-rich interior zone are generally older (ca. 283 Ma) and younger in the LREE-rich mantle (ca. 256 Ma; Fig. 13c). Based on tiny ilmenite inclusions in monazite, minimum temperatures of ∼ 450 °C for the onset of monazite growth are estimated. This is consistent with the elevated Th content in the bright core, since at lower-grade conditions, Th-poor monazite is expected to form together with thorite (Rasmussen and Muhling, 2007).

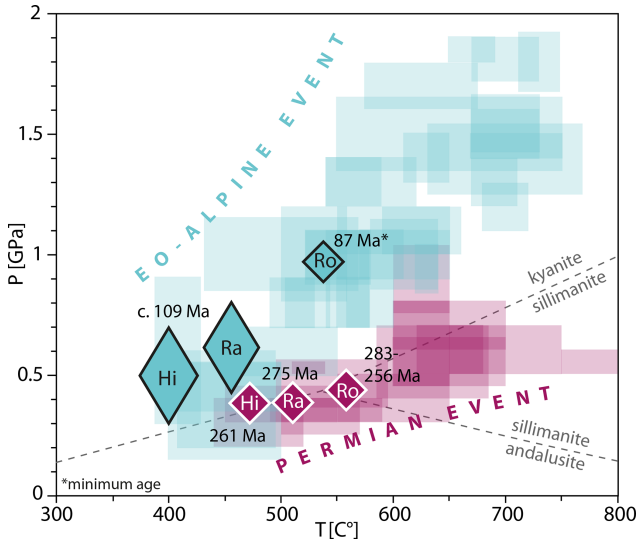

Figure 16. *P–T–t* data for the Permian and Eo-Alpine event in each location. Transparent rectangles represent published *P–T* data compiled by Knoll et al. (2023) for the Permian and Schuster et al. (2004) for the Eo-Alpine events.

Overall, our Permian *P–T–t* data are consistent with the literature data recording LP-HT metamorphism over a time span from 290 to 240 Ma (Fig. 16; see Knoll et al., 2023, for a compilation of Permian *P–T–t* data; Stumpf et al., 2024). Younger ages towards higher structural levels are consistent with a progressively increasing heat flow in response to lithospheric thinning (Knoll et al., 2023, and references therein). Prolonged metamorphism over a time span of ca. 27 Myr corroborated by our monazite age data is consistent with slow heating rates that were inferred for the Permian event (Bestel et al., 2009; Gaidies et al., 2008b; Knoll et al., 2023). Geochronological data of the Raasberg samples do not directly disclose the duration of metamorphism. However, the unusually coarse grain size observed in some Raasberg samples provides at least indirect evidence for the long-lasting nature of Permian metamorphism.

The discovery of Permian metamorphism in the Schöckel Nappe implies that the timing of metamorphism in the neighboring DG nappes (Gasen and Gschnaidt nappes) has to be reconsidered. Pre-Alpine garnet reported by Schantl et

al. (2015) at the base of the Gschnaidt Nappe formed most likely during Permian metamorphism. Moreover, the presumed Eo-Alpine inverted metamorphic gradient across the three nappes proposed by Schantl et al. (2015) may also be inherited from the Permian event. Permian metamorphism in this part of the DG-NS provides an explanation for a long-known peculiarity compared to nappes composed of low-grade metamorphic Paleozoic metasediments elsewhere in the Austroalpine Unit. For instance, the low-grade metamorphic nappes of the Gurktal Alps and the Tirolic–Noric Nappe System experienced a Variscan tectonometamorphic imprint and often contain slices of transgressive Permo-Mesozoic metasediments (e.g., Neubauer et al., 2022, and references therein), which are missing in the DG nappes north of Graz (e.g., Flügel and Hubmann, 2000). The metamorphic conditions determined for the Schöckel Nappe (450–520 °C and 0.3–0.4 GPa) imply that the unit was buried several kilometers in the Permian. Therefore, no sediments could be deposited on top of this unit during the post-Variscan sedimentation cycle, which commenced in the Permian.

7.4.2 Eo-Alpine event

In the Schöckel Nappe, we constrain Eo-Alpine P–T conditions of $\sim$ 470 °C and 0.4–0.7 GPa at the base of the nappe that decrease to $\sim$ 400 °C and 0.3–0.6 GPa at higher structural levels. These P–T estimates are subject to greater uncertainty compared to Permian peak conditions; nonetheless we emphasize that similar P–T conditions were calculated in other units of similar Eo-Alpine grade (e.g., Hollinetz et al., 2022) and are generally consistent with the Eo-Alpine geothermal gradient (Fig. 16; Schuster et al., 2004). Timing for the Eo-Alpine overprint is determined using the U–Th–Pb data of Ep_2 in sample Ra-4. The significance of the date is complicated by the compositional heterogeneity of the Ep_2 domains and presence of numerous apatite and monazite inclusions. Low Ca concentrations in two analyses that fall on the main trend likely represent monazite inclusions, supporting the presence of secondary Mnz_2. Since Ep_2, apatite and Mnz_2 formed from the same Reaction (7), we see no reason to exclude these "polluted" analyses from the age calculation. We interpret the Pb/U–Th date of 108.8 ± 6.6 Ma as the crystallization age of Ep_2 (+ Ap + Mnz_2) during the Eo-Alpine metamorphic overprint but acknowledge that chemical heterogeneity and existence of phase boundaries within the analytical volume may compromise the precision of our date to some degree. It is therefore not surprising that our age is somewhat younger than biotite Rb–Sr data, suggesting cooling below 300 °C at 113 ± 1 Ma (Schantl et al., 2015). Despite these small discrepancies we argue that within error, both our results, data by Schantl et al. (2015) and other white mica ages from the area (Gasser et al., 2010, and references therein) are broadly consistent with metamorphism and exhumation of the Schöckel Nappe in the Early Cretaceous (> 110 Ma). This relatively older evolution prior to peak metamorphism in the higher-grade KW-NS is comparable to other units of similar grade (Hollinetz et al., 2022).

In the Waxenegg Nappe, Eo-Alpine P–T conditions (550 °C, 1.0–1.1 GPa) are somewhat lower in temperature but higher in pressure compared to published thermobarometric data (580–590 °C, 0.77–0.87 GPa; Krenn et al., 2008). This discrepancy may result from using mineral pairs that formed during different metamorphic events for previous P–T calculations. We constrain the timing of Eo-Alpine metamorphism from the geochronology of the Mnz_2 rim at ca. 90 Ma. Individual U–Pb dates of the overgrowth zone display a significant dispersion, evident from the relatively large MSWD value of this population (Fig. 13c). Comparable to the Permian evolution, this may indicate protracted monazite growth, which would support the extended time span for prograde metamorphism in other KW nappes suggested by Stumpf et al. (2024). Alternatively, older dates in the overgrowth zone may be compromised by minor amounts of Permian monazite. Avoiding this potential source of error, a mean weighted age of 87.3 ± 1.2 Ma that is calculated from the youngest population (n: 9, MSWD: 5.2) is considered as the minimum age of Eo-Alpine monazite formation. Eo-Alpine peak metamorphism at ca. 90 Ma is consistent with the timing of the pressure peak in the eclogite facies units of the KW-NS (Miladinova et al., 2022; Thöni et al., 2008). Cooling below 300 °C at 80 Ma (Schantl et al., 2015) suggests fast cooling and exhumation during the Late Cretaceous, which is also typical for the KW-NS (Thöni, 2006, and references therein).

A major finding of our study is that the main fabric in all investigated samples is inherited from the Permian event. Deformation during the Eo-Alpine overprint is evident only locally in all sample groups. In the Hirschkogel samples, the S3 crenulation, which reoriented Permian porphyroblasts, is attributed to Eo-Alpine deformation. In the Raasberg samples, the intensity of Eo-Alpine deformation varies strongly, indicating that even in proximity to the nappe boundary, Eo-Alpine deformation in the Schöckel Nappe was strongly localized. The geochronological data do not correlate with the degree of deformation: sample Ra-4 records only the Eo-Alpine event, albeit statically recrystallized during the overprint, whereas in the strongly deformed sample Ra-3, Permian allanite is preserved. Allanite and REE epidote recrystallization is therefore primarily driven by chemical disequilibrium (Sect. 7.2.1), but the minerals remain unaffected by deformation, highlighting the potential of allanite to preserve a pre-Alpine or prograde metamorphic age, even after significant overprint by deformation postdating peak metamorphism. This finding is comparable to the preservation of Permian allanite in an eclogite facies Alpine shear zone reported from the western Alps (Cenki-Tok et al., 2011). Even in the highest-grade Rossegg samples, we found that, at least on a microstructural level, the Eo-Alpine overprint is a static event, evinced from the preservation of staurolite pseudomorphs. This circumstance may be explained by the fact that

our samples were collected distally from the nappe boundary. Our finding highlights that inheritance of Permian fabrics should be considered in future studies investigating the structural evolution of nappes of the KW-NS.

7.5 Implications for Cretaceous tectonics

Our conclusion that the main mineral assemblage and fabrics in the Schöckel Nappe formed during Permian metamorphism suggests that previous quantitative P–T estimates, especially their timing (e.g., Krenn et al., 2008; Schantl et al., 2015), must be considered with care. Based on our data, we can draw the following implications on the nature of the contact separating the Waxenegg and Schöckel nappes. At the time of Eo-Alpine peak metamorphism in the Waxenegg Nappe, the Schöckel Nappe was already exhumed to upper-crustal levels ($< 300\,°C$). This implies a P–T difference of $\sim 250\,°C$ and at least 0.5 GPa, potentially up to 0.7–0.8 GPa, between the two nappes. Such a discordance is consistent with the exhumation of the Waxenegg Nappe below a major low-angle normal fault in the ductile regime between 90 and 80 Ma. This structure separates rocks with a predominantly Permian and low-grade Eo-Alpine overprint in the hanging wall from rocks with a Permian and medium-grade, P-dominated Eo-Alpine metamorphic overprint in the footwall. Assuming lithostatic pressure, a standard upper-crustal density of $2700\,kg\,m^{-3}$ and a fault plane dip of 25°, the pressure difference would correspond to a minimum displacement of 45 km (0.5 GPa) or 71 km (0.8 GPa) along the fault. Krenn et al. (2008) also proposed a large-scale, top-to-northeast shear zone along the contact, which was subsequently overprinted by top-to-southwest normal faulting. However, the Permian evolution was not recognized at the time. Therefore, we strongly advise revisiting the tectonic evolution and kinematics of the proposed fault in future studies, taking the Permian metamorphism and structural evolution into account. Schantl et al. (2015) noted the presence of a phyllonite zone separating the Waxenegg Nappe from the overlying DG nappes. This zone may correspond to a gradient with increasing finite strain and retrogression in the footwall which would be expected towards a detachment contact.

Such a large-scale, low-angle normal fault is comparable to structures at the base of the DG-NS in the central and western parts of the Austroalpine Unit (e.g., Griesmeier et al., 2019; Koroknai et al., 1999; Neubauer et al., 1995; Putiš et al., 2002; Rantitsch et al., 2020; Ratschbacher et al., 1989; Schorn and Stüwe, 2016; Sölva et al., 2005). For instance, a multimethod investigation of the DG nappes in the Gurktal Alps revealed that these units are detached along major normal faults with east-directed kinematics in the Gurktal Alps (Koroknai et al., 1999; Neubauer et al., 1995; Rantitsch et al., 2020). Both the magnitude of the temperature difference between hanging wall and footwall (100–250 °C; Rantitsch et al., 2020) and the timing of peak metamorphism in the footwall (ca. 99–83 Ma; Iglseder, 2019; Neubauer et al., 2003; Wölfler et al., 2023) are comparable to our study area. West of the Tauern window, similar (Eo-Alpine) crustal-scale structures with southeast-directed kinematics are reported from the base of the DG-NS (Froitzheim et al., 1997; Fügenschuh et al., 2000; see also cross sections in Reiser et al., 2010). Based on thermochronometric and geochronological data together with RSCM analyses, significant differences of about 200 °C between the footwall and hanging wall together with rapid footwall exhumation between 100–70 Ma are documented (Fügenschuh et al., 2000; Hölzer et al., 2024; Lünsdorf et al., 2012; Rockenschaub, 2003).

These low-angle normal faults and shear zones with east- or southeast-directed kinematics juxtapose low-grade rocks of the DG-NS against higher-grade ($> 500\,°C$) portions of the Austroalpine nappe stack and presumably facilitated the exhumation of Eo-Alpine eclogites in the KW-NS during the Late Cretaceous extensional regime. Furthermore, the activity of these normal-sense structures seems more or less coeval with west-northwest-directed thrusting in structurally lower parts of the nappe stack (e.g., in the Vinschgau shear zone at the base of the Ötztal Nappe; Montemagni et al., 2023). Upper Cretaceous synorogenic sediments of the Gosau Group that unconformably overlie these low-angle detachments provide additional constraints on the timing (Wagreich and Decker, 2001). To conclude, synorogenic Late Cretaceous low-angle detachments are documented from all over the Austroalpine Unit. We therefore interpret the low-angle normal fault between the Schöckel and Waxenegg nappes as a segment of a larger crustal-scale structure, which we tentatively term the "Austroalpine Detachment System".

8 Conclusions

We investigated the metamorphic evolution of metapelites in two nappes of the Austroalpine Unit separated by a major tectonic contact. In situ U–Th–Pb dating of allanite and REE epidote and monazite coupled with thermodynamic forward modeling revealed Permian (290–250 Ma) and Eo-Alpine (109–87 Ma) metamorphism in both the hanging wall (Schöckel Nappe, DG-NS) and the footwall (Waxenegg Nappe, KW-NS). For both events, an upright metamorphism gradient is identified, with P–T conditions increasing from 475 °C and 0.3–0.4 GPa to 560 °C and 0.4 GPa during the Permian and $\sim 400\,°C$ and 0.3–0.6 GPa to 550 °C and 1.0–1.1 GPa during the Eo-Alpine events.

Contrasting REE mineral evolution histories in samples with identical P–T histories revealed that the bulk rock composition of major elements, most importantly Ca, Al and Na, exerts a first-order control on P–T conditions at which REE mineral reactions occur. For Ca-poor and Al-rich metapelites, the bulk rock Na content determines whether allanite or monazite forms. In Na-rich samples where metamorphic plagioclase formed, we observe restricted or no allanite formation. Significant secondary REE mineral forma-

tion is observed if the overprint occurred outside the stability field of the primary REE mineral assemblage. In cases where the overprint falls in the stability field of the primary REE mineral, we noted contrasting behavior of allanite and monazite. Primary allanite is preserved and unaffected by deformation, thus geochronology only records the first event. Primary monazite on the other hand is more prone to fluid-assisted dissolution and reprecipitation forming secondary monazite. Single monazite can therefore record complex polyphase histories.

We stress that recognizing a pre-Alpine imprint in low-grade mineral assemblages is not as straightforward compared to higher-grade rocks where polymetamorphism is more easily identified, for example from garnet zoning patterns. Moreover, the Permian and Eo-Alpine P–T gradients converge at greenschist facies conditions (Fig. 16), making it more difficult to link P–T data to either the high- or low-pressure gradient when geochronological data are not available. As a consequence, Permian metamorphism might be underestimated in greenschist facies units of the UAU that lack Permian igneous rocks, emphasizing the necessity of precise geochronological data in low-grade metamorphic units. We here demonstrate that a dataset relying on multiple samples is invaluable for understanding the effects of P–T conditions, bulk rock composition and deformation on a complex, polyphase REE mineral evolution, which provides the basis to determine both the pre-Alpine and Eo-Alpine metamorphic evolution of poorly constrained Austroalpine basement nappes.

The main metamorphic signature and structural imprint in the Schöckel Nappe corresponds to the Permian event, and the Eo-Alpine overprint is lower grade than previously assumed. Our results imply a marked increase of $\sim 250\,^{\circ}\mathrm{C}$ and at least 0.5 GPa between the two nappes at the timing of peak metamorphism in the Waxenegg Nappe. For a simple, low-angle normal fault geometry, this would correspond to a minimum displacement of 45 km. We therefore propose the existence of a major low-angle normal fault between the KW and DG nappe systems, which is potentially part of a crustal-scale structure, tentatively termed the Austroalpine Detachment System.

Data availability. The EMPA and LA-ICP-MS datasets and bulk composition data used for pseudosection calculations are openly available at the Tethys research data repository of GeoSphere Austria (https://doi.org/10.24341/tethys.231, Hollinetz et al., 2024).

Supplement. The supplement related to this article is available online at: https://doi.org/10.5194/ejm-36-943-2024-supplement.

Author contributions. MSH: conceptualization, data curation, formal analysis, funding acquisition, investigation, visualization, project administration, writing (original draft). BH: conceptualization, investigation, resources, supervision, writing (review and editing). DAS: funding acquisition, supervision, writing (review and editing). CRMM: formal analysis, investigation, methodology, resources. RS: resources, writing (review and editing). GR: investigation, writing (review and editing). PS: investigation, resources. CI: resources, writing (review and editing). MR: resources, writing (review and editing). BG: supervision, writing (review and editing).

Competing interests. The contact author has declared that none of the authors has any competing interests.

Disclaimer. Publisher's note: Copernicus Publications remains neutral with regard to jurisdictional claims made in the text, published maps, institutional affiliations, or any other geographical representation in this paper. While Copernicus Publications makes every effort to include appropriate place names, the final responsibility lies with the authors.

Acknowledgements. Financial support for this research was provided by the Uni:docs fellowship program of the University of Vienna, the Marietta Blau scholarship of the Austrian Academy of Sciences, and the Natural Sciences and Engineering Research Council of Canada (NSERC Discovery). Open-access funding was provided by the University of Vienna. We thank Brandon Boucher (UNB) for his support with the LA-ICP-MS analyses and Franz Kiralyi (University of Vienna) for his assistance with the EPMA. We greatly acknowledge the editorial handling by Chiara Groppo and thorough reviews by Paola Manzotti and an anonymous reviewer which significantly improved the quality of the manuscript.

Financial support. This research has been supported by the Natural Sciences and Engineering Research Council of Canada (grant no. NSERC Discovery).

Review statement. This paper was edited by Chiara Groppo and reviewed by Paola Manzotti and one anonymous referee.

References

Armbruster, T., Bonazzi, P., Akasaka, M., Bermanec, V., Chopin, C., Gieré, R., Armbruster, T., Bonazzi, P., Akasaka, M., Bermanec, V., Chopin, C., Gieré, R., Heuss-Assbichler, S., Liebscher, A., Menchetti, S., Pan, Y. and Pasero, M.: Recommended nomenclature of epidote-group minerals, Eur. J. Mineral., 18, 551–567, https://doi.org/10.1127/0935-1221/2006/0018-0551, 2006.

Bestel, M., Gawronski, T., Abart, R., and Rhede, D.: Compositional zoning of garnet porphyroblasts from the polymetamorphic Wölz Complex, Eastern Alps, Miner. Petrol., 97, 173–188, https://doi.org/10.1007/s00710-009-0084-z, 2009.

Bollinger, L. and Janots, E.: Evidence for Mio-Pliocene retrograde monazite in the Lesser Himalaya, far western Nepal,

Eur. J. Mineral., 18, 289–297, https://doi.org/10.1127/0935-1221/2006/0018-0289, 2006.

Bojar, H. P., Bojar, A. V., Mogessie, A., Fritz, H., and Thalhammer, O. A. R.: Evolution of veins and sub-economic ore at Strassegg, Paleozoic of Graz, Eastern Alps, Austria: evidence for local fluid transport during metamorphism, Chem. Geol., 175, 757–777, https://doi.org/10.1016/S0009-2541(00)00342-9, 2001.

Boston, K. R., Rubatto, D., Hermann, J., Engi, M., and Amelin, Y.: Geochronology of accessory allanite and monazite in the Barrovian metamorphic sequence of the Central Alps, Switzerland, Lithos, 286, 502–518, https://doi.org/10.1016/j.lithos.2017.06.025, 2017.

Broska, I., Williams, C. T., Janák, M., and Nagy, G.: Alteration and breakdown of xenotime-(Y) and monazite-(Ce) in granitic rocks of the Western Carpathians, Slovakia, Lithos, 82, 71–83, https://doi.org/10.1016/j.lithos.2004.12.007, 2005.

Budzyn, B., Harlov, D. E., Williams, M. L., and Jercinovic, M. J.: Experimental determination of stability relations between monazite, fluorapatite, allanite, and REE-epidote as a function of pressure, temperature, and fluid composition, Am. Mineral., 96, 1547–1567, https://doi.org/10.2138/am.2011.3741, 2011.

Catlos, E. J., Gilley, L. D., and Harrison, T. M.: Interpretation of monazite ages obtained via in situ analysis, Chem. Geol., 188, 193–215, https://doi.org/10.1016/S0009-2541(02)00099-2, 2002.

Cenki-Tok, B., Oliot, E., Rubatto, D., Berger, A., Engi, M., Janots, E., Thomsen, T. B., Manzotti, P., Regis, D., Spandler, C., and Robyr, M.: Preservation of Permian allanite within an Alpine eclogite facies shear zone at Mt Mucrone, Italy: Mechanical and chemical behavior of allanite during mylonitization, Lithos, 125, 40–50, https://doi.org/10.1016/j.lithos.2011.01.005, 2011.

Coggon, R., and Holland, T. J. B.: Mixing properties of phengitic micas and revised garnet-phengite thermobarometers, J. Metamorph. Geol., 20, 683–696, https://doi.org/10.1046/j.1525-1314.2002.00395.x, 2002.

Dallmeyer, R. D., Handler, R., Neubauer, F., and Fritz, H.: Sequence of thrusting within a thick-skinned tectonic wedge: Evidence from 40Ar/39Ar and Rb-Sr ages from the Austroalpine nappe complex of the Eastern Alps, J. Geol., 106, 71–86, https://doi.org/10.1086/516008, 1998.

De Capitani, C. and Petrakakis, K.: The computation of equilibrium assemblage diagrams with Theriak/Domino software, Am. Mineral., 95, 1006–1016, https://doi.org/10.2138/am.2010.3354, 2010.

Evans, T. P.: A method for calculating effective bulk composition modification due to crystal fractionation in garnet-bearing schist: Implications for isopleth thermobarometry, J. Metamorph. Geol., 22, 547–557, https://doi.org/10.1111/j.1525-1314.2004.00532.x, 2004.

Feenstra, A., Ockenga, E., Rhede, D., and Wiedenbeck, M.: Li-rich zincostaurolite and its decompression-related breakdown products in a diaspore-bearing metabauxite from East Samos (Greece): An EMP and SIMS study, Am. Mineral., 88, 789–805, https://doi.org/10.2138/am-2003-5-608, 2003.

Finger, F., Broska, I., Roberts, M. P., and Schermaier, A.: Replacement of primary monazite by apatite-allanite-epidote coronas in an amphibolite facies granite gneiss from the eastern Alps, Am. Mineral., 83, 248–258, https://doi.org/10.2138/am-1998-3-408, 1998.

Finger, F., Krenn, E., Schulz, B., Harlov, D., and Schiller, D.: "Satellite monazites" in polymetamorphic basement rocks of the Alps: Their origin and petrological significance, Am. Mineral., 101, 1094–1103, https://doi.org/10.2138/am-2016-5477, 2016.

Flügel, H. W. and Hubmann, B.: Das Paläozoikum von Graz: Stratigraphie und Bibliographie. Schriftreihe der Erdwissenschaftlichen Kommission (Vol. 13), Österreichische Akademie der Wissenschaften, Wien, 118 pp., ISBN 3-7001-2859-2, 2000.

Foster, G. and Parrish, R. R.: Metamorphic monazite and the generation of PTt paths, Geol. Soc. Spec. Publ., 220, 25–47, https://doi.org/10.1144/GSL.SP.2003.220.01.02, 2003.

Fritz, H.: Kinematics and geochronology of Early Cretaceous thrusting in the northwestern Paleozoic of Graz (Eastern Alps), Geodin. Acta, 2, 53–62, https://doi.org/10.1080/09853111.1988.11105156, 1988.

Fritz, H.: Stratigraphie, Fazies und Tektonik im nordwestlichen Grazer Paläozoikum (Ostalpen), Jb. Geol. B.-A., 134, 227–255, 1991.

Froitzheim, N., Conti, P. T., and Van Daalen, M.: Late Cretaceous, synorogenic, low-angle normal faulting along the Schlinig fault (Switzerland, Italy, Austria) and its significance for the tectonics of the Eastern Alps, Tectonophysics, 280, 267–293, https://doi.org/10.1016/S0040-1951(97)00037-1, 1997.

Froitzheim, N., Plašienka, D., and Schuster, R.: Alpine tectonics of the Alps and Western Carpathians, The Geology of Central Europe Volume 2: Mesozoic and Cenozoic, edited by: McCann, T., Geological Society of London, 1141–1232, https://doi.org/10.1144/CEV2P.6, 2008.

Fügenschuh, B., Mancktelow, N. S., and Seward, D.: Cretaceous to Neogene cooling and exhumation history of the Oetztal-Stubai basement complex, eastern Alps: A structural and fission track study, Tectonics, 19, 905–918, https://doi.org/10.1029/2000TC900014, 2000.

Fuhrman, M. L. and Lindsley, D. H.: Ternary-feldspar modeling and thermometry, Am. Mineral., 73, 201–215, 1988.

Gaidies, F., Abart, R., De Capitani, C., Schuster, R., Connolly, J. A. D., and Reusser, E.: Characterization of polymetamorphism in the Austroalpine basement east of the Tauern Window using garnet isopleth thermobarometry, J. Metamorph. Geol., 24, 451–475, https://doi.org/10.1111/j.1525-1314.2006.00648.x, 2006.

Gaidies, F., Krenn, E., De Capitani, C., and Abart, R.: Coupling forward modelling of garnet growth with monazite geochronology: an application to the Rappold Complex (Austroalpine crystalline basement), J. Metamorph. Geol., 26, 775–793, https://doi.org/10.1111/j.1525-1314.2008.00787.x, 2008a.

Gaidies, F., De Capitani, C., Abart, R., and Schuster, R.: Prograde garnet growth along complex P–T–t paths: results from numerical experiments on polyphase garnet from the Wölz Complex (Austroalpine basement), Contrib. Mineral. Petr., 155, 673–688, https://doi.org/10.1007/s00410-007-0264-y, 2008b.

Gasser, D., Stüwe, K., and Fritz, H.: Internal structural geometry of the Paleozoic of Graz, Int. J. Earth. Sci., 99, 1067–1081, https://doi.org/10.1007/s00531-009-0446-0, 2010.

Gasser, D., Bruand, E., Rubatto, D., and Stüwe, K.: The behaviour of monazite from greenschist facies phyllites to anatectic gneisses: an example from the Chugach Metamorphic Complex, southern Alaska, Lithos, 134, 108–122, https://doi.org/10.1016/j.lithos.2011.12.003, 2012.

Grand'Homme, A., Janots, E., Seydoux-Guillaume, A. M., Guillaume, D., Bosse, V., and Magnin, V.: Partial resetting of the U-Th-Pb systems in experimentally altered monazite: Nanoscale evidence of incomplete replacement, Geology, 44, 431–434, https://doi.org/10.1130/G37770.1, 2016.

Grand'Homme, A., Janots, E., Seydoux-Guillaume, A.-M., Guillaume, D., Magnin, V., Hövelmann, J., Höschen, C., and Boiron, M. C.: Mass transport and fractionation during monazite alteration by anisotropic replacement, Chem. Geol., 484, 51–68, https://doi.org/10.1016/j.chemgeo.2017.10.008, 2018.

Gratz, R. and Heinrich, W.: Monazite-xenotime thermobarometry: Experimental calibration of the miscibility gap in the binary system CePO4-YPO4, Am. Mineral., 82, 772–780, https://doi.org/10.2138/am-1997-7-816, 1997.

Griesmeier, G. E., Schuster, R., and Grasemann, B.: Major fault zones in the Austroalpine units of the Kreuzeck Mountains south of the Tauern Window (Eastern Alps, Austria), Swiss, J. Geosci., 112, 39–53, https://doi.org/10.1007/s00015-018-0328-1, 2019.

Habler, G. and Thöni, M.: Preservation of Permo–Triassic low-pressure assemblages in the Cretaceous high-pressure metamorphic Saualpe crystalline basement (Eastern Alps, Austria), J. Metamorph. Geol., 19, 679–697, https://doi.org/10.1046/j.0263-4929.2001.00338.x, 2001.

Habler, G., Thöni, M., and Sölva, H.: Tracing the high pressure stage in the polymetamorphic Texel Complex (Austroalpine basement unit, Eastern Alps): P–T–t–d constraints, Miner. Petrol., 88, 269–296, https://doi.org/10.1007/s00710-006-0143-7, 2006.

Habler, G., Thöni, M., and Grasemann, B.: Cretaceous metamorphism in the Austroalpine Matsch Unit (Eastern Alps): the interrelation between deformation and chemical equilibration processes, Miner. Petrol., 97, 149–171, https://doi.org/10.1007/s00710-009-0094-x, 2009.

Harlov, D. E., Wirth, R., and Hetherington, C. J.: Fluid-mediated partial alteration in monazite: the role of coupled dissolution–reprecipitation in element redistribution and mass transfer, Contrib. Mineral. Petr., 162, 329–348, https://doi.org/10.1007/s00410-010-0599-7, 2011.

Henrichs, I. A., Chew, D. M., O'Sullivan, G. J., Mark, C., McKenna, C., and Guyett, P.: Trace element (Mn-Sr-Y-Th-REE) and U-Pb isotope systematics of metapelitic apatite during progressive greenschist-to amphibolite-facies Barrovian metamorphism, Geochem. Geophy. Geosy., 20, 4103–4129, https://doi.org/10.1029/2019GC008359, 2019.

Henry, D. J., Guidotti, C. V., and Thomson, J. A.: The Ti-saturation surface for low-to-medium pressure metapelitic biotites: Implications for geothermometry and Ti-substitution mechanisms, Am. Mineral., 90, 316–328, https://doi.org/10.2138/am.2005.1498, 2005.

Hentschel, F., Janots, E., Trepmann, C. A., Magnin, V., and Lanari, P.: Corona formation around monazite and xenotime during greenschist-facies metamorphism and deformation, Eur. J. Mineral., 32, 521–544, https://doi.org/10.5194/ejm-32-521-2020, 2020.

Hermann, J.: Allanite: thorium and light rare earth element carrier in subducted crust, Chem. Geol., 192, 289–306, https://doi.org/10.1016/S0009-2541(02)00222-X, 2002.

Hetherington, C. J., Harlov, D. E., and Budzyń, B.: Experimental metasomatism of monazite and xenotime: mineral stability, REE mobility and fluid composition, Miner. Petrol., 99, 165–184, https://doi.org/10.1007/s00710-010-0110-1, 2010.

Holland, T. J. B. and Powell, R.: An improved and extended internally consistent thermodynamic dataset for phases of petrological interest, involving a new equation of state for solids, J. Metamorph. Geol., 29, 333–383, https://doi.org/10.1111/j.1525-1314.2010.00923.x, 2011.

Holland, T. J. B., Green, E. C. R., and Powell, R.: A thermodynamic model for feldspars in $KAlSi_3O_8$–$NaAlSi_3O_8$–$CaAl_2Si_2O_8$ for mineral equilibrium calculations, J. Metamorph. Geol., 40, 587–600, https://doi.org/10.1111/jmg.12639, 2022.

Hollinetz, M. S., Schneider, D. A., McFarlane, C. R. M., Huet, B., Rantitsch, G., and Grasemann, B.: Bulk inclusion micro-zircon U–Pb geochronology: A new tool to date low-grade metamorphism, J. Metamorph. Geol., 40, 207–227, https://doi.org/10.1111/jmg.12624, 2022.

Hollinetz, M. S., McFarlane, C. R. M., Huet, B., and Schantl, P.: EPMA, LA-ICP-MS U-Pb and bulk rock composition datasets of metapelites from the Austroalpine Unit north of Graz, Tethys Research Data Repository, https://doi.org/10.24341/tethys.231, 2024.

Hölzer, K., Wolff, R., Hetzel, R., and Dunkl, I.: The Long-Lasting Exhumation History of the Ötztal-Stubai Complex (Eastern European Alps): New Constraints from Zircon (U–Th)/He Age-Elevation Profiles and Thermokinematic Modeling, Lithosphere, 174, 20 pp., https://doi.org/10.2113/2024/lithosphere_2023_174, 2024.

Hoschek, G.: Phase relations of the REE minerals florencite, allanite and monazite in quartzitic garnet–kyanite schist of the Eclogite Zone, Tauern Window, Austria, Eur. J. Mineral., 28, 735–750, https://doi.org/10.1127/ejm/2016/0028-2549, 2016.

Iglseder, C.: Lithostratigrafische und lithodemische Einheiten auf GK25 Blatt Radenthein-Ost, in: Arbeitstagung 2019 der Geologischen Bundesanstalt. Geologie des Kartenblattes GK25 Radenthein-Ost, edited by: Griesmeier, G. E. U. and Iglseder, C., 19–44, ISBN 978-973-610-873-0, 2019.

Janots, E., Negro, F., Brunet, F., Goffé, B., Engi, M., and Bouybaouène, M. L.: Evolution of the REE mineralogy in HP–LT metapelites of the Sebtide complex, Rif, Morocco: monazite stability and geochronology, Lithos, 87, 214–234, https://doi.org/10.1016/j.lithos.2005.06.008, 2006.

Janots, E., Brunet, F., Goffé, B., Poinssot, C., Burchard, M., and Cemič, L.: Thermochemistry of monazite-(La) and dissakisite-(La): implications for monazite and allanite stability in metapelites, Contrib. Mineral. Petr., 154, 1–14, https://doi.org/10.1007/s00410-006-0176-2, 2007.

Janots, E., Engi, M., Berger, A., Allaz, J., Schwarz, J. O., and Spandler, C.: Prograde metamorphic sequence of REE minerals in pelitic rocks of the Central Alps: implications for allanite–monazite–xenotime phase relations from 250 to 610 C, J. Metamorph. Geol., 26, 509–526, https://doi.org/10.1111/j.1525-1314.2008.00774.x, 2008.

Janots, E., Engi, M., Rubatto, D., Berger, A., Gregory, C., and Rahn, M.: Metamorphic rates in collisional orogeny from in situ allanite and monazite dating, Geology, 37, 11–14, https://doi.org/10.1130/G25192A.1, 2009.

Janots, E., Berger, A., and Engi, M.: Physico-chemical control on the REE minerals in chloritoid-grade metasediments from a

single outcrop (Central Alps, Switzerland), Lithos, 121, 1–11, https://doi.org/10.1016/j.lithos.2010.08.023, 2011.

Jeřábek, P., Janák, M., Faryad, S. W., Finger, F., and Konečný, P.: Polymetamorphic evolution of pelitic schists and evidence for Permian low-pressure metamorphism in the Vepor Unit, West Carpathians, J. Metamorph. Geol., 26, 465–485, https://doi.org/10.1111/j.1525-1314.2008.00771.x, 2008.

Knoll, T., Huet, B., Schuster, R., Mali, H., Ntaflos, T., and Hauzenberger, C.: Lithium pegmatite of anatectic origin-A case study from the Austroalpine Unit Pegmatite Province (Eastern European Alps): geological data and geochemical model, Ore. Geol. Rev., 154, 105298, https://doi.org/10.1016/j.oregeorev.2023.105298, 2023.

Koroknai, B., Neubauer, F., Genser, J., and Topa, D.: Metamorphic and tectonic evolution of Austroalpine units at the western margin of the Gurktal nappe complex, Eastern Alps, Schweiz. Miner. Petrog., 79, 277–295, 1999.

Krenn, E. and Finger, F.: Formation of monazite and rhabdophane at the expense of allanite during Alpine low temperature retrogression of metapelitic basement rocks from Crete, Greece: Microprobe data and geochronological implications, Lithos, 95, 130–147, https://doi.org/10.1016/j.lithos.2006.07.007, 2007.

Krenn, K., Fritz, H., Mogessie, A., and Scharflechner, J.: Late Cretaceous exhumation history of an extensional extruding wedge (Graz Paleozoic Nappe Complex, Austria), Int. J. Earth. Sci., 97, 1331–1352, https://doi.org/10.1007/s00531-007-0221-z, 2008.

Livi, K. J., Ferry, J. M., Veblen, D. R., Frey, M., and Connolly, J. A.: Reactions and physical conditions during metamorphism of Liassic aluminous black shales and marls in central Switzerland, Eur. J. Mineral., 14, 647–672, 2002.

Lo Pò, D. and Braga, R.: Influence of ferric iron on phase equilibria in greenschist facies assemblages: The hematite-rich metasedimentary rocks from the Monti Pisani (Northern Apennines), J. Metamorph. Geol., 32, 371–387, https://doi.org/10.1111/jmg.12076, 2014.

Lünsdorf, N. K., Dunkl, I., Schmidt, B. C., Rantitsch, G., and von Eynatten, H.: The thermal history of the Steinach Nappe (eastern Alps) during extension along the Brenner Normal Fault system indicated by organic maturation and zircon (U-Th)/He thermochronology, Austrian, J. Earth. Sci., 105, 17–25, 2012.

Lünsdorf, N. K., Dunkl, I., Schmidt, B. C., Rantitsch, G., and von Eynatten, H.: Towards a higher comparability of geothermometric data obtained by Raman spectroscopy of carbonaceous material. Part 2: A revised geothermometer, Geostand. Geoanal. Res., 41, 593–612, https://doi.org/10.1111/ggr.12178, 2017.

Matura, A. and Schuster, R.: Geologische Karte der Republik Österreich 1:50 000, Blatt 135 Birkfeld, Verlag der Geologischen Bundesanstalt, Wien, https://doi.org/10.24341/tethys.58, 2014.

Maruyama, S., Liou, J. G., and Suzuki, K.: The peristerite gap in low-grade metamorphic rocks, Contrib. Mineral. Petr., 81, 268–276, https://doi.org/10.1007/BF00371681, 1982.

Miladinova, I., Froitzheim, N., Nagel, T. J., Janak, M., Fonseca, R. O., Sprung, P., and Münker, C.: Constraining the process of intracontinental subduction in the Austroalpine Nappes: Implications from petrology and Lu-Hf geochronology of eclogites, J. Metamorph. Geol., 40, 423–456, https://doi.org/10.1111/jmg.12634, 2022.

Montemagni, C., Zanchetta, S., Rocca, M., Villa, I. M., Morelli, C., Mair, V., and Zanchi, A.: Kinematics and time-resolved evolution of the main thrust-sense shear zone in the Eo-Alpine orogenic wedge (the Vinschgau Shear Zone, eastern Alps), Solid Earth, 14, 551–570, https://doi.org/10.5194/se-14-551-2023, 2023.

Nagy, G., Draganits, E., Demény, A., Pantó, G., and Arkai, P.: Genesis and transformations of monazite, florencite and rhabdophane during medium grade metamorphism: examples from the Sopron Hills, Eastern Alps, Chem. Geol., 191, 25–46, https://doi.org/10.1016/S0009-2541(02)00147-X, 2002.

Neubauer, F., Dallmeyer, R. D., Dunkl, I., and Schirnik, D.: Late Cretaceous exhumation of the metamorphic Gleinalm dome, Eastern Alps: kinematics, cooling history and sedimentary response in a sinistral wrench corridor, Tectonophysics, 242, 79–98, https://doi.org/10.1016/0040-1951(94)00154-2, 1995.

Neubauer, F., Genser, J., and Handler, R.: Tectonic Evolution of the western margin of the Gurktal nappe complex, Eastern Alps: Constraints from structural studies and 40Ar/39Ar white mica ages, Mitteilungen der Österreichischen Mineralogischen Gesellschaft, 148, 240–241, 2003.

Neubauer, F., Fried, G., Genser, J., Handler, R., Mader, D., and Schneider, D.: Origin and tectonic evolution of the Eastern Alps deduced from dating of detrital white mica: a review, Austrian, J. Earth. Sci., 100, 8–23, 2007.

Neubauer, F., Liu, Y., Dong, Y., Chang, R., Genser, J., and Yuan, S.: Pre-Alpine tectonic evolution of the Eastern Alps: from prototethys to paleotethys, Earth-Sci. Rev., 226, 103923, https://doi.org/10.1016/j.earscirev.2022.103923, 2022.

Nosenzo, F., Manzotti, P., Poujol, M., Ballèvre, M., and Langlade, J.: A window into an older orogenic cycle: P–T conditions and timing of the pre-Alpine history of the Dora-Maira Massif (Western Alps), J. Metamorph. Geol., 40, 789–821, https://doi.org/10.1111/jmg.12646, 2022.

Piber, A., Tropper, P., and Mirwald, P. W.: The metamorphic evolution of the Patscherkofel Crystalline Complex (Tyrol, Eastern Alps, Austria), Austrian. J. Earth. Sci., 101, 27–35, 2008.

Plunder, A., Agard, P., Dubacq, B., Chopin, C., and Bellanger, M.: How continuous and precise is the record of P–T paths? Insights from combined thermobarometry and thermodynamic modelling into subduction dynamics (Schistes Lustrés, W. Alps), J. Metamorph. Geol., 30, 323–346, https://doi.org/10.1111/j.1525-1314.2011.00969.x, 2012.

Powell, R. and Holland, T. J. B.: On thermobarometry, J. Metamorph. Geol., 26, 155–179, https://doi.org/10.1111/j.1525-1314.2007.00756.x, 2008.

Putiš, M., Korikovsky, S. P., Wallbrecher, E., Unzog, W., Olesen, N. Ø., and Fritz, H.: Evolution of an eclogitized continental fragment in the Eastern Alps (Sieggraben, Austria), J. Struct. Geol., 24, 339–357, https://doi.org/10.1016/S0191-8141(01)00071-2, 2002.

Pyle, J. M., Spear, F. S., Rudnick, R. L., and McDonough, W. F.: Monazite–xenotime–garnet equilibrium in metapelites and a new monazite–garnet thermometer, J. Petrol., 42, 2083–2107, https://doi.org/10.1093/petrology/42.11.2083, 2001.

Rantitsch, G., Iglseder, C., Schuster, R., Hollinetz, M. S., Huet, B., and Werdenich, M.: Organic metamorphism as a key for reconstructing tectonic processes: a case study from the Austroalpine unit (Eastern Alps), Int. J. Earth. Sci., 109, 2235–2253, https://doi.org/10.1007/s00531-020-01897-7, 2020.

Rantitsch, G., Sachsenhofer, R. F., Hasenhüttl, C., Russegger, B., and Rainer, T.: Thermal evolution of an extensional detachment

as constrained by organic metamorphic data and thermal modeling: Graz Paleozoic Nappe Complex (Eastern Alps), Tectonophysics, 411, 57–72, https://doi.org/10.1016/j.tecto.2005.08.022, 2005.

Rasmussen, B. and Muhling, J. R.: Monazite begets monazite: evidence for dissolution of detrital monazite and reprecipitation of syntectonic monazite during low-grade regional metamorphism, Contrib. Mineral. Petr., 154, 675–689, https://doi.org/10.1007/s00410-007-0216-6, 2007.

Rasmussen, B. and Muhling, J. R.: Reactions destroying detrital monazite in greenschist-facies sandstones from the Witwatersrand basin, South Africa, Chem. Geol., 264, 311–327, https://doi.org/10.1016/j.chemgeo.2009.03.017, 2009.

Rasmussen, B., Fletcher, I. R., and McNaughton, N. J.: Dating low-grade metamorphic events by SHRIMP U-Pb analysis of monazite in shales, Geology, 29, 963–966, https://doi.org/10.1130/0091-7613(2001)029<0963:DLGMEB>2.0.CO;2, 2001.

Ratschbacher, L., Frisch, W., Neubauer, F., Schmid, S. M., and Neugebauer, J.: Extension in compressional orogenic belts: the eastern Alps, Geology, 17, 404–407, https://doi.org/10.1130/0091-7613(1989)017<0404:EICOBT>2.3.CO;2, 1989.

Reiser, M. K., Scheiber, T., Fügenschuh, B., and Burger, U.: Hydrological characterisation of lake Obernberg, Brenner Pass area, Tyrol, Austrian. J. Earth. Sci., 103, 43–57, 2010.

Ricchi, E., Bergemann, C. A., Gnos, E., Berger, A., Rubatto, D., and Whitehouse, M. J.: Constraining deformation phases in the Aar Massif and the Gotthard Nappe (Switzerland) using Th-Pb crystallization ages of fissure monazite-(Ce), Lithos, 342, 223–238, https://doi.org/10.1016/j.lithos.2019.04.014, 2019.

Rockenschaub, M., Kolenbrat, B., and Frank, W.: Geochronologische Daten aus dem Brennergebiet: Steinacher Decke, Brennermesozoikum, Ötz-Stubai-Kristallin, Innsbrucker Quarzphyllitkomplex, Tarntaler Mesozoikum, in: "Brenner": Arbeitstagung 2003, Trins im Gschnitztal, 1.–5. September 2003: Geologische Kartenblätter 1:50.000 148 Brenner, edited by: Rockenschaub, M., 117–124, ISBN 3-85316-018-2, 2003.

Rudnick, R. L. and Gao, S.: Composition of the continental crust, in: Treatise on Geochemistry (Vol. 3), edited by: Holland, H. D. and Turekian, K. K., Elsevier–Pergamon, Oxford, 1–64, https://doi.org/10.1016/B0-08-043751-6/03016-4, 2003.

Schantl, P., Schuster, R., Krenn, K., and Hoinkes, G.: Polyphase metamorphism at the southeastern margin of the Graz Paleozoic and the underlying Austroalpine basement units, Austrian. J. Earth. Sci., 108, https://doi.org/10.17738/ajes.2015.0023, 2015.

Schmid, S. M., Fügenschuh, B., Kissling, E., and Schuster, R.: Tectonic map and overall architecture of the Alpine orogeny, Eclogae. Geol. Helv., 97, 93–117, https://doi.org/10.1007/s00015-004-1113-x, 2004.

Schulz, B. and Krause, J.: Electron probe petrochronology of polymetamorphic garnet micaschists in the lower nappe units of the Austroalpine Saualpe basement (Carinthia, Austria), Z. Dtsch. Ges. Geowiss., 172, 19 pp., https://doi.org/10.1127/zdgg/2021/0247, 2021.

Schuster, R. and Stüwe, K.: Permian metamorphic event in the Alps, Geology, 36, 603–606, https://doi.org/10.1130/G24703A.1, 2008.

Schuster, R. and Stüwe, K.: Geological and Tectonic Setting of Austria, in: Landscapes and Landforms of Austria, World Geomorphological Landscapes, edited by: Embleton-Hamann, C., Springer, Cham, https://doi.org/10.1007/978-3-030-92815-5_1, 2022.

Schuster, R., Scharbert, S., Abart, R., and Frank, W.: Permo-Triassic extension and related HT/LP metamorphism in the Austroalpine-Southalpine realm, Mitt. Ges. Geol. Bergbaustud. Österr, 45, 111–141, 2001.

Schuster, R., Koller, F., Höck, V., Hoinkes, G., and Bousquet, R.: Explanatory notes to the map: Metamorphic structure the Alps: Metamorphic evolution of the Eastern Alps, Mitt. Österr. Miner. Ges., 149, 175–199, 2004.

Schorn, S. and Stüwe, K.: The Plankogel detachment of the Eastern Alps: petrological evidence for an orogen-scale extraction fault, J. Metamorph. Geol., 34, 147–166, https://doi.org/10.1111/jmg.12176, 2016.

Seydoux-Guillaume, A. M., Montel, J. M., Bingen, B., Bosse, V., de Parseval, P., Paquette, J. L., Janots, E., and Wirth, R.: Low-temperature alteration of monazite: Fluid mediated coupled dissolution–precipitation, irradiation damage, and disturbance of the U–Pb and Th–Pb chronometers, Chem. Geol., 330, 140–158, https://doi.org/10.1016/j.chemgeo.2012.07.031, 2012.

Shaw, D. M.: Geochemistry of pelitic rocks. Part III: Major elements and general geochemistry, Geol. Soc. Am. Bull., 67, 919–934, https://doi.org/10.1130/0016-7606(1956)67[919:GOPRPI]2.0.CO;2, 1956.

Skrzypek, E., Bosse, V., Kawakami, T., Martelat, J. E., and Štípská, P.: Transient allanite replacement and prograde to retrograde monazite (re) crystallization in medium-grade metasedimentary rocks from the Orlica-Śnieżnik Dome (Czech Republic/Poland): textural and geochronological arguments, Chem. Geol., 449, 41–57, https://doi.org/10.1016/j.chemgeo.2016.11.033, 2017.

Skrzypek, E., Kato, T., Kawakami, T., Sakata, S., Hattori, K., Hirata, T., and Ikeda, T.: Monazite behaviour and time-scale of metamorphic processes along a low-pressure/high-temperature field gradient (Ryoke Belt, SW Japan), J. Petrol., 59, 1109–1144, https://doi.org/10.1093/petrology/egy056, 2018.

Sölva, H., Grasemann, B., Thöni, M., Thiede, R., and Habler, G.: The Schneeberg normal fault zone: normal faulting associated with Cretaceous SE-directed extrusion in the Eastern Alps (Italy/Austria), Tectonophysics, 401, 143–166, https://doi.org/10.1016/j.tecto.2005.02.005, 2005.

Spear, F. S.: Monazite–allanite phase relations in metapelites, Chem. Geol., 279, 55–62, https://doi.org/10.1016/j.chemgeo.2010.10.004, 2010.

Spear, F. S. and Pyle, J. M.: Theoretical modeling of monazite growth in a low-Ca metapelite, Chem. Geol., 273, 111–119, https://doi.org/10.1016/j.chemgeo.2010.02.016, 2010.

Stumpf, S., Skrzypek, E., and Stüwe, K.: Dating prograde metamorphism: U–Pb geochronology of allanite and REE-rich epidote in the Eastern Alps, Contrib. Mineral. Petr., 179, 63, https://doi.org/10.1007/s00410-024-02130-3, 2024.

Stüwe, K. and Schuster, R.: Initiation of subduction in the Alps: Continent or ocean?, Geology, 38, 175–178, https://doi.org/10.1130/G30528.1, 2010.

Thöni, M.: Dating eclogite-facies metamorphism in the Eastern Alps–approaches, results, interpretations: a review, Miner.

Petrol., 88, 123–148, https://doi.org/10.1007/s00710-006-0153-5, 2006.

Thöni, M., Miller, C., Blichert-Toft, J., Whitehouse, M. J., Konzett, J., and Zanetti, A.: Timing of high-pressure metamorphism and exhumation of the eclogite type-locality (Kupplerbrunn–Prickler Halt, Saualpe, south-eastern Austria): constraints from correlations of the Sm–Nd, Lu–Hf, U–Pb and Rb–Sr isotopic systems, J. Metamorph. Geol., 26, 561–581, https://doi.org/10.1111/j.1525-1314.2008.00778.x, 2008.

Tropper, P. and Recheis, A.: Garnet zoning as a window into the metamorphic evolution of a crystalline complex: the northern and central Austroalpine Ötztal-Complex as a polymorphic example, Mitteilungen der Österreichischen Geologischen Gesellschaft, 94, 27–53, 2003.

Vermeesch, P.: IsoplotR: A free and open toolbox for geochronology, Geosci. Front., 9, 1479–1493, https://doi.org/10.1016/j.gsf.2018.04.001, 2018.

Vermeesch, P.: Unifying the U–Pb and Th–Pb methods: joint isochron regression and common Pb correction, Geochronology, 2, 119–131, https://doi.org/10.5194/gchron-2-119-2020, 2020.

von Raumer, J. F. and Neubauer, F.: Late Precambrian and Palaeozoic evolution of the Alpine basement–an overview, in: Pre-Mesozoic geology in the Alps, edited by: von Raumer, J. F. and Neubauer, F., Springer, Berlin, Heidelberg, 625–639, https://doi.org/10.1007/978-3-642-84640-3_37, 1993.

Wagreich, M. and Decker, K.: Sedimentary tectonics and subsidence modelling of the type Upper Cretaceous Gosau basin (Northern Calcareous Alps, Austria), Int. J. Earth. Sci., 90, 714–726, https://doi.org/10.1007/s005310000181, 2001.

Wawrzenitz, N., Krohe, A., Rhede, D., and Romer, R. L.: Dating rock deformation with monazite: The impact of dissolution precipitation creep, Lithos, 134, 52–74, https://doi.org/10.1016/j.lithos.2011.11.025, 2012.

White, R. W., Powell, R., and Johnson, T. E.: The effect of Mn on mineral stability in metapelites revisited: New a–x relations for manganese-bearing minerals, J. Metamorph. Geol., 32, 809–828, https://doi.org/10.1111/jmg.12095, 2014.

Whitney, D. L. and Evans, B. W.: Abbreviations for names of rock-forming minerals, Am. Mineral., 95, 185–187, 2010.

Williams, M. L., Jercinovic, M. J., Harlov, D. E., Budzyń, B., and Hetherington, C. J.: Resetting monazite ages during fluid-related alteration, Chem. Geol., 283, 218–225, https://doi.org/10.1016/j.chemgeo.2011.01.019, 2011.

Wing, B. A., Ferry, J. M., and Harrison, T. M.: Prograde destruction and formation of monazite and allanite during contact and regional metamorphism of pelites: petrology and geochronology, Contrib. Mineral. Petr., 145, 228–250, https://doi.org/10.1007/s00410-003-0446-1, 2003.

Wölfler, A., Wolff, R., Hampel, A., Hetzel, R., and Dunkl, I.: Phases of enhanced exhumation during the cretaceous and cenozoic orogenies in the Eastern European Alps: new insights from thermochronological data and thermokinematic modeling, Tectonics, 42, e2022TC007698, https://doi.org/10.1029/2022TC007698, 2023.

Wu, C. M. and Chen, H. X.: Revised Ti-in-biotite geothermometer for ilmenite-or rutile-bearing crustal metapelites, Sci. Bull., 60, 116–121, https://doi.org/10.1007/s11434-014-0674-y, 2015.

Yardley, B. W. D. and Baltatzis, E.: Retrogression of staurolite schists and the sources of infiltrating fluids during metamorphism, Contrib. Mineral. Petr., 89, 59–68, https://doi.org/10.1007/BF01177591, 1985.